UNIVERSITY OF CALIFORNIA

Santa Barbara

Engineered Platforms to Investigate Effects of Cell-Cell and 3D Adhesions on Structural and Functional Maturity of Human Induced Pluripotent Stem Cell-Derived Cardiomyocytes (hiPSC-CMs)

A dissertation submitted in partial satisfaction of the

requirements for the degree Doctor of Philosophy

in Mechanical Engineering

by

Kerry Veronica Lane

Committee in charge:

Professor Beth L. Pruitt, Chair

Professor Megan Valentine

Professor Sam Daly

Professor Anthony DeTomaso

December 2023

The dissertation of Kerry Veronica Lane is approved.

_____

Megan Valentine

_____

Sam Daly

_____

Anthony DeTomaso

_____

Beth L. Pruitt, Committee Chair

September 2023

Engineered Platforms to Investigate Effects of Cell-Cell and 3D Adhesions on Structural and Functional Maturity of Human Induced Pluripotent Stem Cell-Derived Cardiomyocytes (hiPSC-CMs)

ACKNOWLEDGEMENTS

First, I want to thank my family who have supported me throughout my entire life. My parents have always nurtured my love of math and science and I started in Mechanical Engineering to follow in my dad's footsteps. My sister has been one of my biggest supporters, and on more than one occasion during this PhD she has helped me with her statistical expertise. Finally, my little Milly has been a beacon of light whenever I have struggled. Her excitement to see me every time I'm away from her for over a minute, as well as the joy she has brought my lab mates and friends has been crucial to me making it through the tough spots during my PhD.

I want to gratefully acknowledge staff members at UCSB that have helped me along the way to my PhD. Dr. Dave Bothman in the CNSI Microfluidics Laboratory was incredibly helpful in troubleshooting device fabrication. Dr. Ben Lopez in the NRI-MCDB Microscopy Facility was always available to help with imaging optimization, especially with confocal imaging.

I am also incredibly grateful for the current members and alumni of the Pruitt Lab who have provided friendship and support during my PhD. I joined the lab alongside Orlando Chirikian, Liam Dow, and Sam Feinstein and have had the pleasure of working with them for the entirety of my degree. Dr. Anna Kim and Dr. Erica Castillo were both wonderful mentors, collaborators, and office mates who I am thankful to have gotten to work with. I also have had the pleasure of sharing an office with Gabby Villalpando Torres, who has been an amazing friend, co-worker, and honorary dog mom to my Milly.

Outside of research, I have had much support from the office of Instructional Development that has allowed me to find and grow my love of teaching and develop new skills along the way. Dr. Lisa Berry and Dr. Olga Faccani, especially, have been incredibly supportive of my growth as an educator and my interest in improving my teaching practice.

I want to thank my committee members – Dr. Sam Daly, Dr. Tony De Tomaso, and Dr. Megan Valentine – who are excellent academics and have provided guidance and advice during my PhD. I want to give special thanks to Dr. Sam Daly, who in addition to serving as a committee member, was the first professor I TAed for and has provided mentorship and opportunities for further teaching throughout my PhD.

I'd like to thank my advisor, Dr. Beth Pruitt, for taking me on during my second year and giving me the space to explore research that interests me. As a woman in Mechanical Engineering, having a strong and successful female advisor has been very impactful. Beth has helped me cultivate confidence in my abilities both within and outside of research. Beth has also encouraged me to pursue my interests outside of research, including helping to create opportunities for me teach, which made me realize my passion for teaching. I am incredibly grateful for all that you have done for me Beth.

Finally, I want to acknowledge the funding that has supported my PhD, including the UCSB Chancellor's Fellowship, the NSF GRFP (award No. 1650114), and the NIH (3RM1GM131981-02S1).

VITA OF KERRY VERONICA LANE

July 2023

Education

University of California, Santa Barbara (UCSB) — Expected Graduation: *August 2023*

Ph.D. in Mechanical Engineering with Bioengineering Emphasis and Certificate in College and University Teaching (CCUT)
Cumulative GPA: 3.93/4.00

M.S. in Mechanical Engineering
Cumulative GPA: 3.93/4.00 — *May 2020*

Seattle University (SU)

B.S. in Mechanical Engineering with a Minor in Mathematics — *June 2017*
Cumulative GPA: 3.92/4.00, *Summa Cum Laude*

Teaching and Mentorship Experience

Lead TA of Mechanical Engineering Department, UCSB — *August 2021 - Present*

- Worked with Mechanical Engineering Chair and Vice-Chair to expand department TA training and increase the resources of Lead TA
- Redesigned the TA orientation session, created activities and examples to practice implementing grading best practices and an introduction to active learning techniques
- Created a workshop series for TAs including sessions focused on fostering belonging in engineering courses, assessing students, and backwards learning course/lecture design
- Developed and collected resources for TAs, including handouts with tips for grading, running office hours, and navigating the instructor-TA relationship and a roster of former TAs for each course

Associate in Mechanical Engineering, UCSB
Course: Statics — *Summer 2021*

- Redesigned the course to implement a flipped classroom; recorded 15 lectures for students to watch before the accompanying synchronous problem solving sessions
- Developed 6 tests and 6 quizzes, one quiz and test per week, to ensure regular checks of students' comprehension

Graduate Teaching Assistant, UCSB

Course: Statics — *Fall 2017 & 2019*

- Prepared and taught a 1.5 hour lecture on centroids and center of mass (2019)
- Prepared and led weekly 1 hour long recitation sections, held weekly offices hours, wrote exam questions, and graded and provided feedback on homework and exams
- Head TA (2019) – organized schedules for splitting grading and proctoring with other TAs for the course

Course: Vibrations — *Winter 2018*

- Designed and wrote homework assignments, held weekly offices hours, graded exams

Course: Cellular Bioengineering (graduate level course) — *Winter 2019*

- Prepared and led lab sessions teaching students cell culture, immunohistochemistry, and brightfield and fluorescence microscopy
- Held weekly offices hours, graded and provided feedback on homework and presentations

Course: Methods in Mechanobiology (graduate level course) — *Winter 2020, 2021, & 2022*

- Prepared and led lab sessions teaching students PDMS molding, microcontact printing, polyacrylamide gel casting, brightfield and fluorescence microscopy, and traction force microscopy (TFM)
- Prepared and taught 1.5 hour lectures on traction force microscopy (2020, 2021), microcontact printing (2020), and atomic force microscopy (AFM, 2022)
- Designed and wrote homework assignments, graded and provided feedback on homework and projects

Research Mentor, UCSB *September 2020 - present*

- Abhishek Sharma, Graduate Rotation Student (Fall 2020)
- Shaylee Larson, Graduate Rotation Student (Summer 2022)
- Janae Gayle, Undergraduate Student, UC LEADS Scholar (June 2022 – June 2023)

Student Grader, SU *September 2015 – July 2017*

Courses: Statics, Dynamics
Responsibilities: Graded and provided feedback on students homework

Research Experience

Graduate Student Researcher, UCSB
Department of Mechanical Engineering

Dissertation Lab
Advisor: Beth Pruitt *January 2019 - Present*

Dissertation Title: *Engineered Platforms to Investigate Effects of Cell-Cell and 3D Adhesions on Human Induced Pluripotent Stem Cell-Derived Cardiomyocyte (hiPSC-CM) Maturity*

- Adapted a platform for single-cell 3D encapsulation of hiPSC-CMs
- Developed a high throughput hydrogel platform to enable *in vitro* studies of cardiovascular diseases using hiPSC-CMs
- Trained others on a number of techniques, including photolithography, polyacrylamide gel fabrication, atomic force microscopy, and brightfield and fluorescence microscopy

Pennathur Lab
Advisors: Sumita Pennathur & Deborah Fygenson *September 2017 – December 2018*

- Adapted a protocol for creating DNA-stabilized silver nanoclusters (AgNCs) to allow for a universal ratiometric beacon that does not require exposing the target DNA to silver reduction

Undergraduate Research Assistant, SU
Advisor: Frank Shih *June 2015 – June 2017*

- Collaboratively developed a thermal actuator using carbon nanotubes
- Investigated various materials for impact energy dissipation, including sandwich composites and ceramic fibers

Undergraduate Research Intern, Northwestern University
Advisor: Chad Mirkin *Summer 2016*

- Developed a novel technique for characterizing spherical nucleic acids (SNAs) made with diverse oligonucleotides
- Gained proficiency with high pressure liquid chromatography (HPLC) to purify solutions of synthesized oligonucleotides

Engineering Intern, AGM Container Controls –
Tucson, AZ *Summer 2015*
Supervisor: Eric Zuercher, Vice President

- Produced and edited macros in Visual Basic for Excel, SolidWorks, and BricsCAD

Lab Assistant, University of Arizona *December 2012 – July 2013*
Supervisor: Peter Decelles

- Processed rock and sediment samples for analysis via crushing and gravitational and magnetic separation of minerals

Honors and Awards

2023 Biophysical Society Annual Meeting Travel Award *December 2022*

UCSB Mechanical Engineering Department Best TA Award *October 2020*

National Science Foundation Graduate Research Fellowship (NSF GRFP) *March 2017*

- Awarded an NSF GRFP, an extremely competitive fellowship that recognizes and supports outstanding graduate students who have demonstrated the potential to be high achieving scientists and engineers and provides three years of financial support

UC Santa Barbara Chancellor's Fellowship *March 2017*

- Earned one of the highest honors awarded to an incoming graduate student at the University on the basis of demonstrated academic excellence, leadership, and exceptional promise
- Nominated by the Mechanical Engineering department and one of a very small number of applicants to be awarded this fellowship which provides three years of financial support

Reverend Edmund B. McNulty, S.J., Award *June 2017*

- Awarded the highest honor conferred on one graduating engineering or computer science student in the College of Science and Engineering; judged on scholarship, leadership, dedication, and inspiration.

CoSIDA First Team Academic All-District *November 2015*

- Selected as a member of an honorary sports team composed of the most outstanding student athletes of a specific season and district in various sports. Team selection served as a nomination for Academic All-American honors.

Outreach and Activities

"DEI Discussions: We are all learners" Reading Group *January 2023 – March 2023*

- Bi-weekly group reading & discussing "Inclusive Teaching" by Kelly A. Hogan and Viji Sathy

MultifacetedU Mixer Series *January 2023 – June 2023*

- Co-created a series of mixers for graduate students focused on diversity, equity, and inclusion in teaching and TAing
- Includes sessions focusing on principles of DEI as well as practical application and use in the classroom, in research, and outside of academia

Diversity, Equity, and Inclusion Discussion for Incoming Graduate Students *September 2020*

- Initiated, organized, and led a discussion with the incoming graduate students during the official Mechanical Engineering department orientation
- Selected relevant articles for students to read before the discussion and facilitated conversation about implicit bias, the time tax on underrepresented groups in academia, microaggressions, and being an active bystander

Picture a Scientist Screening *August 2020*

- Organized a screening of the film Picture a Scientist before it was readily available to the public

Partners in Education Outreach *August 2020*

- Designed and led an activity to engage students in STEM fields that was accessible for students to do from home over Zoom

Bailey Gatzert Elementary School Outreach *March 2016 – June 2016*

- Led STEM-focused afterschool program, designed activities to engage students in STEM fields

Membership and Societies

- **American Association of University Women**, **American Society for Engineering Education**, **Biophysical Society** – member
- **Biomedical Engineering Society** – founding member of the UCSB chapter
- **Tau Beta Pi Engineering Society** – secretary of the Washington Gamma chapter, induction November 2015
- **NCAA Division 1 Seattle University Volleyball Team** – four-year starting setter and team captain

Trainings

- **Introduction to Equity-Minded Mentoring Workshop**, Equity in Graduate Education Resource Center, September 2022, *via Zoom*.
- **What does it Mean to be Anti-Racist? Workshop**, UCSB Office of Diversity, Equity, and Inclusion, May 2021, *via Zoom*.
- **Navigating Difficult Dialogues Workshop**, UCSB Office of Diversity, Equity, and Inclusion, June 2021, *via Zoom*.
- **From Awareness to Action: Identifying, Intervening, and Reducing Microagressions Workshop**, UCSB Office of Diversity, Equity, and Inclusion, January 2022, *via Zoom*.

Publications and Patents

1. **Lane, K.V.,** Dow, L.P., et. al. Dual-Protein Patterning to Investigate Effects of Cell-Cell Adhesions on hiPSC-CM Maturity (*in preparation*)
2. Dow, L.P., Gaietta, G., Kaufman, Y., Swift, M.F., Lemos, M., **Lane, K.V.,** et al. "Morphological control enables nanometer-scale dissection of cell-cell signaling complexes" Nature Communications, 2022, doi: 10.1038/s41467-022-35409-9
3. Chirikian, O., Feinstein, S.D., Faynus, M.A., Kim, A.A., **Lane, K.V.**, et al. "The Effects of Xeno-Free Cryopreservation on the Contractile Properties of Human iPSC derived Cardiomyocytes". *Journal of Molecular and Cellular Cardiology*, **2022**.
4. Kim, A.A.*, Castillo, E.A.*, **Lane, K.V.***, et al. "Wafer-Scale Protein Patterning for Hydrogel Devices". *Micromachines*, 1386, **2021**.
5. Castillo, E.A., **Lane, K.V.**, Pruitt, B.L. "Micromechanobiology: Focusing on the Cardiac Cell–Substrate Interface". *Annual Review of Biomedical Engineering*, **2020**.
6. Yasuda, N.K., Schulman, D.S., Traina, D.J., Mather, E.R., **Lane, K.V.**, Lo, M.E., Weaver, K.D., Shih, F.J. "Investigation of Energy Absorption Characteristic of Ceramic Fiber Reinforced Elastomer Composites". ASME International Mechanical Engineering Congress and Exposition, **2017**.
7. **Lane, K.V.**, Yasuda, N.K., Lo, M.E., Mather, E.R., Shih, F.J. "Experimental Characterization of Low Velocity Impact Energy Dissipation in Sandwich Composites With Porous Cores With Tailored Structure and Morphology". *ASME International Mechanical Engineering Congress and Exposition*, **2016**.

8. Bever, A.M., Brown, P.J., **Lane, K.V.**, Levy-Wendt, B.L., Yasuda, N.K., Han, Y.L., Shih, F.J. "Characterization of a Fast Responding Composite Thermal Bimorph Film Actuator Based on Carbon Nanotube Sheets". *ASME International Mechanical Engineering Congress and Exposition*, **2015**.
9. Anna A. Kim, Erica A. Castillo, **Kerry V. Lane**, Gabriela V. Torres, and Beth L. Pruitt. **2021**. Wafer-Scale Protein Patterning of Hydrogel Devices. U.S. Patent 63,274,309, filed November 1, 2021. *Patent pending*.

*These authors contributed equally to this work

Conferences and Presentations

Oral Presentations

1. **Lane, K.V.**, Dow, L.P., et al. "Dual-Protein Patterning to Investigate Effects of Cell-Cell Adhesions on hiPSC-CM Maturity" Biophysical Society Annual Meeting 2023.

Poster Presentations

1. **Lane, K.V.**, Kim, A.A., Castillo, E.A., Torres, G.V., Chirikian, O., Pruitt, B.L. "Scaling up lift-off protein patterning on hydrogels" BMES Cellular and Molecular Bioengineering Conference 2022.
2. **Lane, K.V.**, Castillo, E.A., Wilson, R.E., Chirikian, O., Denisin A.K., Pruitt, B.L. "Tunable Hydrogel Platforms to Investigate Effects of 3D Adhesions on hiPSC-CM Maturity" Biomedical Engineering Society Conference 2020.
3. **Lane, K.V.**, Castillo, E.A., et al. "Tunable Hydrogel Platforms to Investigate Effects of 3D Adhesions on hiPSC-CM Maturity" International Society for Stem Cell Research Annual Conference 2020.
4. **Lane, K.V.**, Pennathur, S., Fygenson, F. "DNA-stabilized silver nanoclusters (AgNCs) for sensing DNA in biological media" IEEE EMBS Micro and Nanotechnology in Medicine Conference 2018.

ABSTRACT

Engineered Platforms to Investigate Effects of Cell-Cell and Adhesions on hiPSC-CM Maturity

by

Kerry Veronica Lane

Heart disease is the leading cause of death in the US, and human cell models are needed to study how structure and function are related in heart health and disease. Human induced pluripotent stem cell-derived cardiomyocytes (hiPSC-CMs) are one promising cell model, but their immaturity (e.g., lower sarcomere alignment and contractility) relative to adult human cardiomyocytes (CMs) limits their physiological relevance. Controlling cellular shape via 2D protein micropatterning has been commonly used to enhance the maturity of single-cell hiPSC-CMs, but is often done via microcontact printing, which has low accuracy and reproducibility, or lift-off patterning, which is less commonly used because of the low-throughput and technical process for creating the pattern templates. In addition to limitations on protein patterning accuracy, these studies have failed to investigate the impact of two important features of native heart tissue: cell-cell contacts between neighboring CMs and the 3D microenvironment. In this work, we sought to scale up the lift-off protein patterning method and improve the single-cell hiPSC-CM model by developing platforms for: 1) dual protein patterning to imitate both CM-ECM and

CM-CM interactions for single-cell hiPSC-CMs and 2) 3D microwells to create a 3D microenvironment for single-cell hiPSC-CMs.

To scale up lift-off patterning, we created protein templates on a 4” wafer and then diced the wafer into individual templates. We showed that we could make at least 16 templates per wafer, and that the protein patterns made with this method were reproducible, had a shelf life of at least 6 months, and were compatible with pattern transfer to polyacrylamide (PA) hydrogels and subsequent culture of hiPSC-CMs. These results allow for the expanded use of lift-off patterning, which is a more accurate and precise method for patterning hiPSC-CMs.

To achieve dual protein patterning, we used a two-step photomolecular adsorption process to create spatially-accurate protein patterns with laminin bodies (to replicate CM-ECM contacts) and N-cadherin end caps (to replicate CM-CM contacts). We cultured hiPSC-CMs on these dual protein patterns and studied their cell shape, subcellular structure, contractility, and force production. We found that dual protein patterning with N-cadherin end caps leads to greater cell area and increased contractility in the direction of sarcomere organization, but no differences in force production or sarcomere organization.

To replicate the 3D microenvironment for single hiPSC-CMs, we utilized a PDMS double molding process to create a thin PDMS mold. The thin mold was incubated with Matrigel (an ECM protein cocktail) and then used when casting a polyacrylamide (PA) hydrogel, creating microwells in the PA hydrogel. We cultured hiPSC-CMs in the microwells and studied their size and subcellular structure. We found that the 3D-patterned hiPSC-CMs had greater cell height than 2D-patterned

hiPSC-CMs, but interestingly no difference in cell volume. We also found that 3D-patterned hiPSC-CMs had greater myofibrillar content than 2D-patterned hiPSC-CMs, suggesting that they had more sarcomeres (subcellular force-producing units).

Using these platforms, we have shown that we can improve hiPSC-CM structure and function through mimicking aspects of the microenvironment of mature human CMs. These platforms can be used to improve the hiPSC-CM model for future studies of heart function and disease.

TABLE OF CONTENTS

LIST OF FIGURES

1. Introduction

1.1. Background

Heart disease is one of the leading causes of death in the world [1]. Research is needed to improve our understanding of the structural and functional changes to heart muscle cells, heart disease, and reveal targets for potential treatments. Human heart research has been historically limited to animal models, most often murine, because of the limited availability of human heart tissue or primary human cardiomyocytes (CMs), the muscle cells of the heart. CMs have a low regenerative capacity, turning over ~1% of cells per year at 25 years old and decreasing to ~0.45% by the age of 75 [2], meaning we cannot take a sample from the heart of a living human, limiting studies on human tissue to donated organs. Additionally, primary human CMs are difficult to culture *in vitro*, typically surviving no more than four weeks [3]. Together, these factors restrict the study of primary human hearts.

With limited access to primary human hearts for studying, murine models have been vital for heart research. However, while these murine models are instructive, they are imperfect – there are many essential differences between murine and human heart physiology [4, 5]. Rats have heart rates five times higher than humans and an inverse force to heart rate relationship [5]. In mature human CMs, about 95% of the sarcomeric myosin heavy chain (*MYH7*) is the beta isoform (*βMHC*) [6]. In murine models, the alpha isoform of *MYH7* (*αMHC*) is the predominant adult isoform [6, 7]. To emphasize the relevance of such a difference, the most common genetic heart disease, hypertrophic cardiomyopathy (HCM), is

frequently caused by mutations in *βMHC* – the lack of *βMHC* expression in murine models limits the study of HCM in these animals [8-10].

1.2. Stem cell derived cardiomyocytes as a reductionist human heart model

One proposed model to bridge the gap between animal models and human heart function and disease are human induced pluripotent stem cell-derived CMs (hiPSC-CMs). hiPSC-CMs are CMs that have been differentiated from human induced pluripotent stem cells (hiPSCs), which are cells that have been reprogrammed back to stemness from differentiated cells [11, 12]. This approach allows researchers to take skin or blood cells from a patient and reprogram them back to stem cells, making hiPSCs a robust supply of stem cells [13, 14]. We can make hiPSC-CMs from hiPSCs with improved protocols that have made hiPSC-CM differentiation more consistent and high-throughput [13], greatly expanding the use of hiPSC-CMs (Figure 1-1).

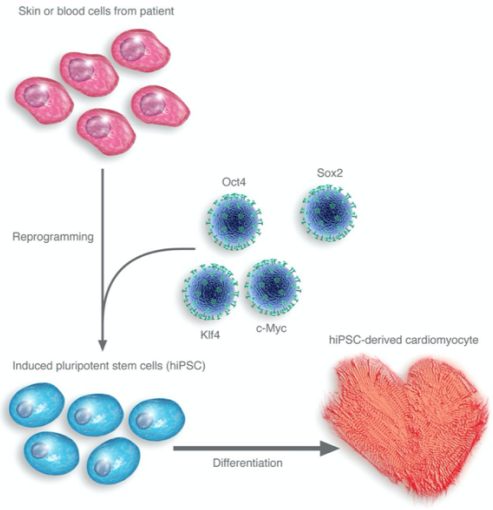

Figure 1-1. Schematic of process flow from patient cell to hiPSC to hiPSC-CM. Reproduced with permission from Eschenhagen, et al. [12].

In addition to being a model with an almost limitless supply, hiPSC-CMs provide the opportunity to observe complex subcellular structures within CMs [6, 15, 16]. CMs are comprised of force producing units called sarcomeres, which join end-to-end with neighboring CMs at intercalated discs (Figure 1-2). Sarcomeres contain myosin motor proteins and actin filaments, which are required for contractile movement, and join together at the z-disc, where the actin thin filaments are bound [17]. Aligned columns of sarcomeres form myofibrils, which are connected to neighboring myofibrils mechanically via adherens junctions and desmosomes, allowing for cooperative contractility of CMs [17-19]. Sarcomeres and other subcellular structures are difficult to visualize in whole hearts or heart tissues, making hiPSC-CMs an ideal model for studying sarcomeric structure and function in CMs. As sarcomeres are the key contractile element of CMs, the ability to visualize and study them is a powerful asset in heart research. Additionally, hiPSC-CMs can be genetically edited to include endogenous fluorescent tags on subcellular structures, making studies of subcellular structures easier and allowing for live-cell imaging of these structures [16, 20]. In this work, we use an hiPSC-CM line tagged on the alpha-actinin-2 protein, developed at the Allen Institute for Cell Science (cell line 75; allencell.org/cell-catalog) [16]. Alpha-actinin-2 is on the z-disc, allowing for visualization of the ends of the hiPSC-CMs sarcomeres (Figure 1-2). Alpha-actinin-2 is not expressed in hiPSCs, so it also serves as a verification of successful hiPSC-CM differentiation [20].

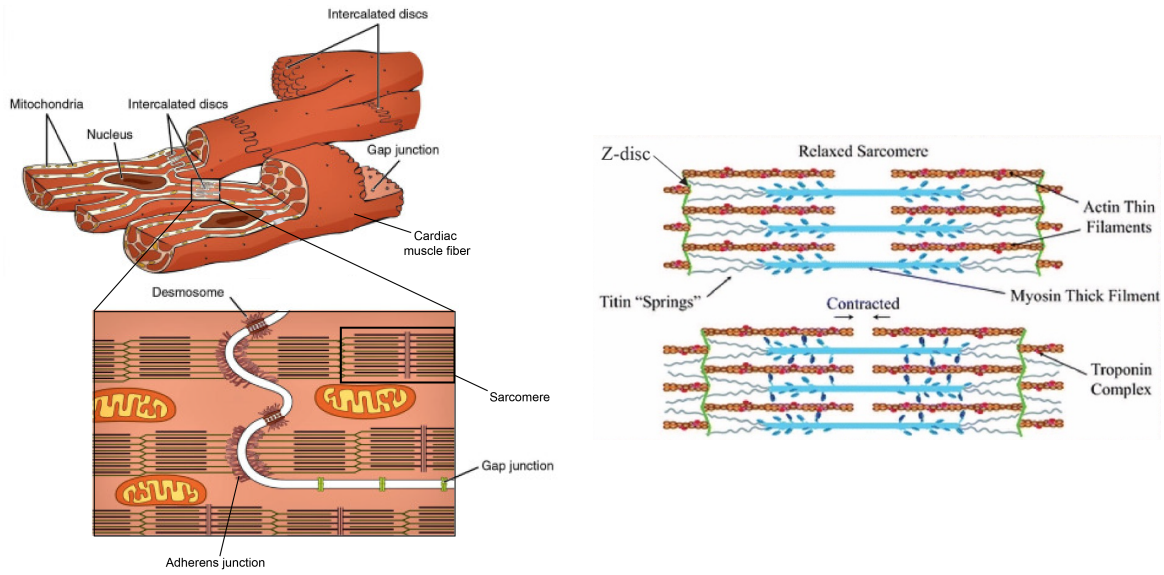

Figure 1-2. Schematics of **(a)** intercalated discs and **(b)** sarcomeres. Figures adapted with permission from (a) [21] and (b) [17].

1.3. Patterning to improve hiPSC-CM maturity

While hiPSC-CMs have become a more widely used model, there remain limitations hindering their use – primarily, the structural and functional differences between hiPSC-CMs and mature human CMs, including CM morphology, sarcomere organization, and contractile force [22, 23]. Mature human CMs have an elongated shape with average length-to-width ratio of approximately 7 or greater and highly aligned sarcomeres; hiPSC-CMs are smaller and have an irregular shape and unaligned sarcomeres, similar to fetal human CMs (Figure 1-3) [6, 15, 24]. Structure is related to function, and sarcomere organization and CM morphology are correlated with contractile force – with more organized and elongated CMs producing higher contractile forces than unorganized, irregularly-shaped CMs [15, 22].

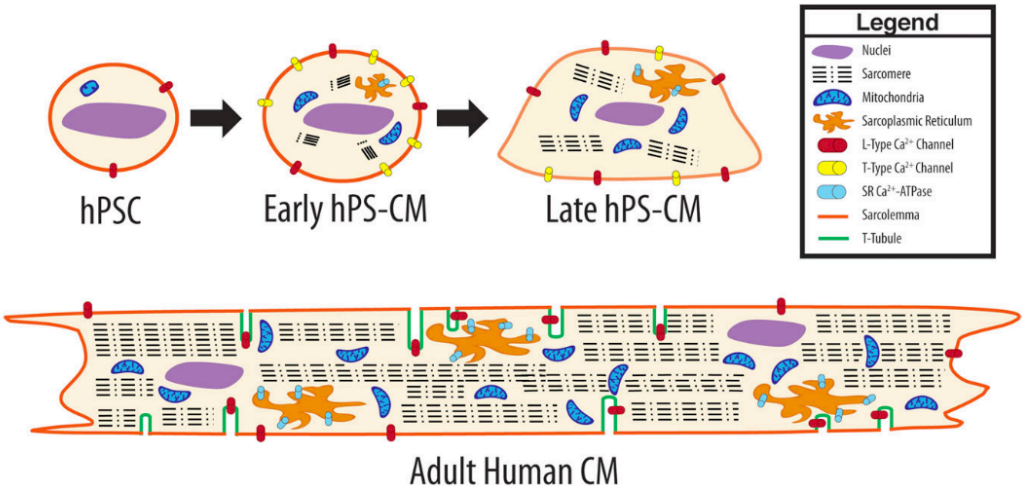

Figure 1-3. Schematic of hiPSC-CM and adult human CMs. Figure reproduced with permission from [24].

There are many approaches that have been used to improve the structural and functional maturity of hiPSC-CMs, including modulating the stiffness of the culture substrate, culturing hiPSC-CMs over long periods, and controlling hiPSC-CM morphology through protein patterning [22, 24]. Protein patterning, which we will focus on here, has been done via a variety of methods, including light-induced molecular adsorption of proteins [25], microcontact printing [26-28], and lift-off [29]. For CMs, studies have typically used rectangular patterns of extracellular matrix (ECM) proteins with aspect ratios of ~7:1, similar to that of mature human CMs [15, 22, 30, 31]. These studies have found that patterned CMs present more highly aligned myofibrils which produce greater contractile forces and other markers of maturity, such as calcium transient anisotropy [15]. Additionally, protein patterning has been shown to work with various device substrates, including polyacrylamide

(PA) hydrogels, allowing for tunable stiffnesses to match physiological microenvironments and for functional measurements such as TFM [15, 27-33].

1.4. Polyacrylamide (PA) hydrogels for tunability and physiological stiffness

PA hydrogels are commonly used due to their range of possible stiffnesses and their tunability. They are made up of crosslinked acrylamide monomers and their stiffness and porosity can be modified by adjusting the amount of monomer and crosslinker [34-36]. The possible stiffnesses of a PA hydrogel can range from approximately 1 kPa to 100 kPa, spanning a large range of physiological tissue stiffness [34-36].

Within that range, we commonly use PA hydrogels with a stiffness of 10kPa, the approximate stiffness of native human heart tissue [37, 38]. At this stiffness, the PA hydrogel can deform due to hiPSC-CM contraction [15, 34, 36]. The deformation of PA provides an environment more similar to the native environment of cardiomyocytes and allows for measurement of the response of hiPSC-CMs acting against a load (the substrate) [15, 34-36]. On glass substrates, hiPSC-CMs do not change length when contracting because glass is not deformable. Instead, hiPSC-CM contraction on glass is described as twitching [15, 31, 39]. For this reason, in this work we will primarily use PA hydrogels.

1.5. Patterning to further improve the hiPSC-CM model

While patterning of CMs has been done with various methods and on varying substrates, most of this patterning has been done with ECM proteins on two-

dimensional surfaces. In their native microenvironment, CMs interact with both the ECM and other CMs in a three-dimensional tissue (Figure 1-2). Therefore, developing methods for patterning hiPSC-CMs with multiple proteins, to mimic CM-ECM and CM-CM interactions, and patterning hiPSC-CMs in 3D could develop a more accurate hiPSC-CM model for a range of applications, including drug screenings and disease studies.

1.6. My Contributions

The cardiomyocyte mechanobiology field has done ample work investigating the interactions between CMs and ECM. These studies have been transformative in hiPSC-CM work but there are still many aspects of the native CM microenvironment that have been understudied with relation to improving the hiPSC-CM model. I sought to improve the hiPSC-CM model by investigating the effects of two aspects of the heart microenvironment: (1) the interactions between CMs and both their neighboring CMs and their surrounding ECM and (2) the 3D nature of the microenvironment. To address these aspects, I developed and utilized a dual-protein patterning platform and a 3D microwell platform, both made in PA hydrogels to replicate a physiologically relevant stiffness and to allow the platform to deform due to hiPSC-CM contraction [15, 34-36]. These platforms fill a gap in current technology in methods for single-cell studies of cell-cell and cell-ECM interactions and in single-cell 3D studies (Figure 1-4). Additionally, I demonstrated that hiPSC-CMs behave distinctly when on dual-protein patterns or in 3D microwells, indicating that further exploration of cell-cell interactions and the 3D microenvironment could

improve single-cell hiPSC-CM maturity. These techniques, and the results I collected with them, can help inform the development of better human models for studies of heart function, disease, and therapeutics.

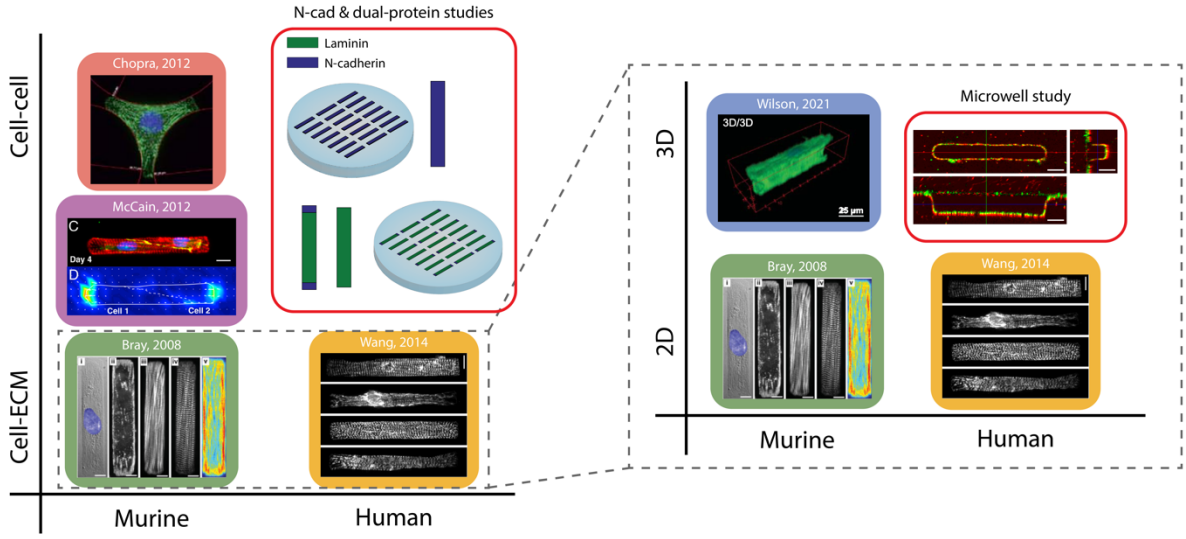

Figure 1-4. Gap in current platforms for *in vitro* studies of hiPSC-CMs**.** Previous work with hiPSC-CMs has focused on cell-ECM interactions [15, 31, 40] and studies investigating CM-CM interactions have been limited to mostly murine models [18, 19, 41, 42]. A gap exists in single-cell studies of cell-cell interactions in a human model. Our dual-protein platform fills this gap by providing interactions mimicking cell-ECM and cell-cell attachments. Within cell-ECM studies, 3D studies have focused on the tissue-level, both in animal models [43, 44] and in human models [45-47]. For single-cell studies, Wilson, et al. patterned individual mouse myocytes in 3D patterns [48], but there has been a gap in human studies. Our microwell platform fills this gap by providing a 3D microenvironment for hiPSC-CMs with high system control. Images have been reproduced with permission from: (left to right, top to bottom) [49] (CC0 1.0: https://creativecommons.org/publicdomain/zero/1.0/), [41], [30], [31], and [48].

1.7. Thesis Overview

Chapter 2 - Micromechanobiology: Focusing on the Cardiac Cell–Substrate Interface

The cell-substrate interface is a key aspect of patterning hiPSC-CMs to improve their structure and function. To continue developing our hiPSC-CM platforms, we review the integrin expression and ECM composition present in the native CM microenvironment. We also consider common strategies used to adhere ECM proteins to the substrate in mechanobiology and various biomaterial approaches to modify parameters in the *in vitro* microenvironment.

Chapter 2 is reprinted and reformatted with permission from the following: Castillo, E. A., Lane, K. V., & Pruitt, B. L. (2020). Micromechanobiology: Focusing on the Cardiac Cell-Substrate Interface. *Annual Review of Biomedical Engineering, 22,* 257-284. [50].

Chapter 3 - Wafer-Scale Patterning of Protein Templates for Hydrogel Fabrication

Fabricating platforms for patterning hiPSC-CMs is often complicated and time-consuming, requiring cleanroom facilities and photolithography experience. To increase the efficiency and throughput of hiPSC-CM platform production, we developed a method for generating shelf-stable protein pattern templates on glass, increasing the yield from each batch ~16-fold. We show that these templates are compatible with polyacrylamide hydrogel co-polymerization and subsequent hiPSC-CM attachment.

Chapter 3 is reprinted and reformatted with permission from the following: Kim, A. A., Castillo, E. A., Lane, K. V., Torres, G. V., Chirikian, O., Wilson, R. E., Lance,

S. A., Pardon, G., & Pruitt, B. L. (2021). Wafer-Scale Patterning of Protein Templates for Hydrogel Fabrication. *Micromachines*, 12(11). [51].

Chapter 4 - Dual-Protein Patterning to Mimic N-Cadherin-Mediated Cell-Cell Contact in Human Induced Pluripotent Stem Cell-Derived Cardiomyocytes (hiPSC-CMs)

To improve existing single-cell hiPSC-CM platforms, we investigated the effect of N-cadherin, as a proxy for cell-cell contact, on hiPSC-CM structure and function. We show that hiPSC-CMs do not attach well to patterns of only N-cadherin. We developed a method for patterning two proteins in a spatially accurate manner to mimic both cell-cell and cell-ECM interactions that exist in the native CM microenvironment. We demonstrate that we can pattern N-cadherin and Laminin in precise designs aligned with one another and that we can transfer these patterns to polyacrylamide hydrogels. We show that hiPSC-CMs on dual-protein patterns have larger cell areas than those on single-protein patterns and greater contractility in the direction of sarcomere organization, but show no differences in aspect ratio, sarcomere organization, or force production.

Chapter 5 - Tunable Hydrogel Platforms to Investigate Effects of 3D Patterning on hiPSC-CM Maturity

To investigate the impact of replicating a 3D microenvironment on hiPSC-CM maturity, we produced single-cell 3D microwells and culture hiPSC-CMs inside of them. We show that we can successfully seed hiPSC-CMs in 3D microwells, but at

a low rate with few single cells. We demonstrate that hiPSC-CMs patterned in 3D microwells have a greater cell height, though we found no differences in cell area. We also demonstrate that hiPSC-CMs in 3D microwells have greater myofibrillar content and qualitatively observed that the sarcomeres in 3D-patterned hiPSC-CMs are organized along the z-direction, versus solely planar sarcomere organization in 2D-patterned hiPSC-CMs.

Chapter 6 - Conclusions and Future Directions

We conclude with a summary of our findings and suggestions for future work with these platforms, including biological questions that can be probed with the use of these platforms.

Appendices

The appendices include detailed protocols and supplementary information.

2. Micromechanobiology: Focusing on the Cardiac Cell-Substrate Interface

This chapter is reprinted and reformatted with permission from the following: Castillo, E. A., Lane, K. V., and Pruitt, B. L., “Micromechanobiology: Focusing on the Cardiac Cell-Substrate Interface”. Annual Review of Biomedical Engineering, 22:257–284, 6 2020. [50]. This chapter includes the entire manuscript, including figures and tables. The chapter covers a review of the native microenvironment of cardiomyocytes in the human heart. It also examines *in vitro* techniques to replicate the heart microenvironment and the interactions between protein and substrate in *in vitro* devices. Finally, this chapter discusses the biomaterial approaches commonly used to adjust aspects of the microenvironment in *in vitro* studies. I was second author and I aided in the development of the review scope and contents with the first author Erica Castillo and my advisor Beth Pruitt. I led the conceptualization and writing for the protein-substrate interface section while Erica led the writing of the whole manuscript and Beth contributed to the design and editing.

2.1. Abstract

Engineered, *in vitro* cardiac cell and tissue systems provide testbeds to study cardiac development, cellular disease processes, and drug responses in a dish. Much effort has focused on improving the structure and function of engineered cardiomyocytes and heart tissues. However, these parameters depend critically on signaling through the cellular microenvironment in terms of ligand composition, matrix stiffness and substrate mechanical properties, i.e., matrix

micromechanobiology. To facilitate improvements to *in vitro* microenvironment design, we review how cardiomyocytes and their microenvironment change during development and disease in terms of integrin expression and ECM matrix composition. We also discuss strategies used to bind proteins to common mechanobiology platforms and discuss important differences in binding strength to the substrate. Finally, we review example biomaterial approaches designed to support and probe cell-ECM interactions of cardiomyocytes *in vitro* as well as open questions and challenges.

2.2. Introduction

Tissue integrity and cardiac function are achieved by cardiomyocytes (CMs) maintaining cell-extracellular matrix (ECM) and cell-cell interactions [52]. Human heart tissue is composed of three layers: endocardium, myocardium, and epicardium (Figure 2-1). The myocardium contracts and relaxes to pump blood throughout the body. Within the myocardium reside CMs, cardiac fibroblasts, cardiac vascular cells, and leukocytes in a network of ECM (Figure 2-1) [17, 53]. CMs generate contractile forces and occupy the largest volume fraction of the myocardium [54]. Cell subtypes, matrix, and composition differ in the atria, ventricles, and conduction bundles, resulting in varied structural, functional, molecular, and electrophysiological properties [55].

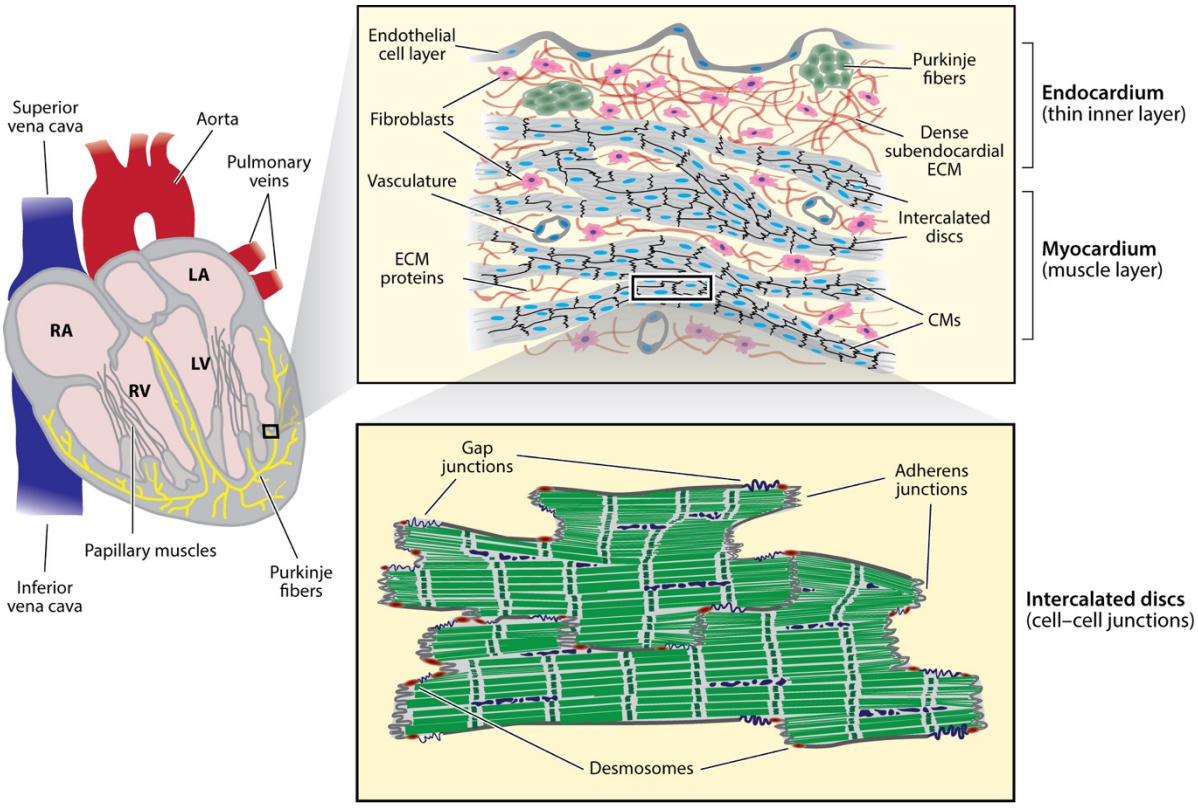

Castillo EA, et al. 2020.
Annu. Rev. Biomed. Eng. 22:257–84

Figure 2-1. Schematic of the heart and the spatial location of myocardium. The myocardium has a highly ordered, hierarchical structure composed mostly of CMs by volume and mostly fibroblasts by cell number, as well as vascular and other cell types. The cell–ECM and cell–cell junctions provide biophysical and biochemical signals to the CMs. The intercalated discs provide neighboring cells with physical and electrical connections. Abbreviations: CM, cardiomyocytes; ECM, extracellular matrix; LA, left atrium; LV, left ventricle; RA, right atrium; RV, right ventricle. Figure adapted from [17] with permission from The Royal Society of Chemistry.

Adherent cell types use various adhesion molecules to physically anchor within this microenvironment (Figure 2-2a) [56]. Integrins are the principal receptors that link ECM proteins to the cell cytoskeleton [57, 58]. CM integrins serve a wide variety of functions, including adhesion, signaling, viral uptake, ion channel regulation, stem

cell differentiation and engraftment, modification of hypertrophic growth responses, and transmission of mechanical signal (mechanotransduction); they may also provide protection from ischemic stress [59]. Other nonintegrin ECM receptors (known to interact directly with the ECM) at the cell surface of CMs include the dystroglycan complex and syndecan proteoglycans [60-62]. In CMs the structure composed of the dystrophin-glycoprotein complex and the integrin-vinculin-talin complex is known as the costamere [63, 64]. In addition to mediating cell-ECM interactions, integrins mediate cell-cell interactions [65]. Intercalated discs connect CMs to one another and are composed of adherens junctions, desmosomes, and gap junctions that provide adhesive and electrical coupling between CMs (Figure 2-1) [66]. Integrins are bidirectional signal transducers, and ligand binding leads to intracellular signaling events (Figure 2-3b) [67, 68]. We use the term outside-in signaling to refer to the cascade of events following integrin-ligand binding. In contrast, inside-out signaling can alter integrin conformation and binding characteristics from within the cell [67]. By simultaneously binding thousands of integrin receptors to ECM binding sites, a cell compiles a spatiotemporal map of the biochemical and biophysical properties of the microenvironment [69].

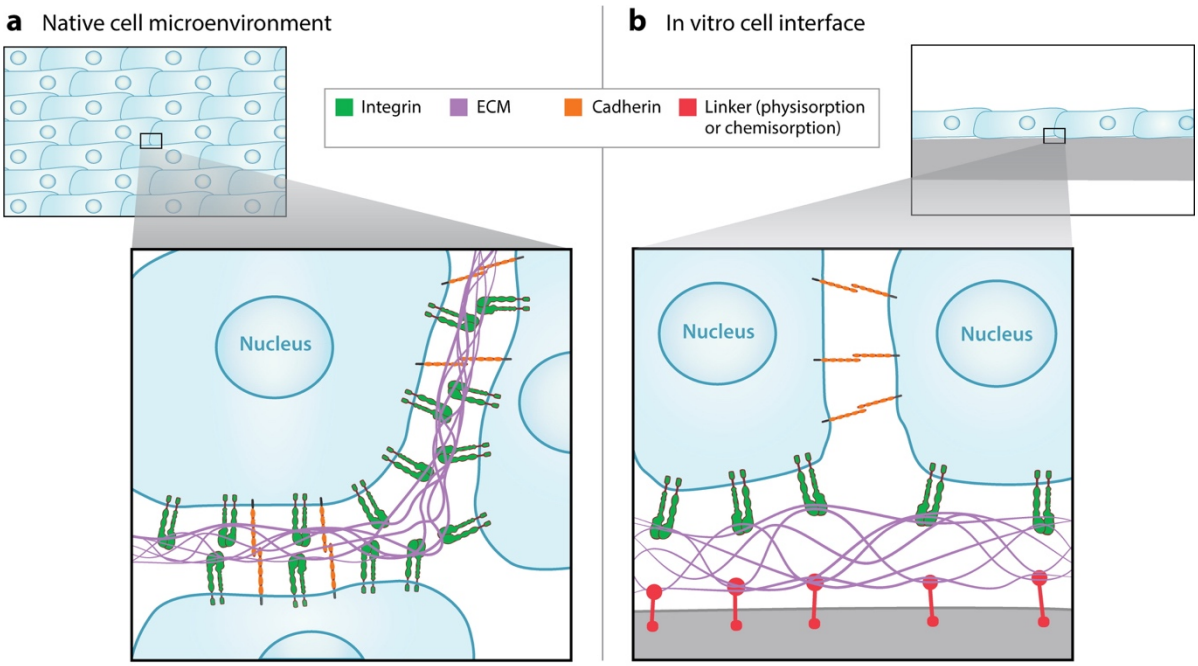

Castillo EA, et al. 2020.
Annu. Rev. Biomed. Eng. 22:257–84

Figure 2-2. Simplified schematic highlighting interactions among integrins, extracellular matrix (ECM), cell–cell contacts, and linkers. **(a)** The native cell microenvironment can be mimicked by **(b)** the *in vitro* cell–substrate interface through the engagement of a cell's integrins with specific ligands found within ECM proteins. The ECM in an *in vitro* interface is physically linked to the substrate (gray) via a linker (red). How a cell interacts (or not) depends on biochemical and biophysical properties of ECM, linker, and substrate. Note that the schematics are not drawn to scale.

The heart undergoes constant cycles of contraction and relaxation. Given the dynamic nature of the heart, a robust structural linkage between CMs and extracellular components is needed to transmit forces and deformations [70]. The myocardial ECM is composed of glycoproteins (e.g., collagens, elastin, fibronectin, laminin), proteoglycans, glycosaminoglycans, and growth factors [53]. The function of each cardiac ECM protein can be structural and/or nonstructural. After being secreted from cells, ECM proteins can undergo further modification and

degradation. Matrix metalloproteinases (MMPs) can remodel the matrix and modify the cell-ECM interface [71, 72], while tissue inhibitor metalloproteinases regulate MMP matrix degradation [73]. ECM properties such as biochemical composition, mechanical properties, and structure are known to influence CM adhesion and cardiac lineage differentiation, function, and maturity.

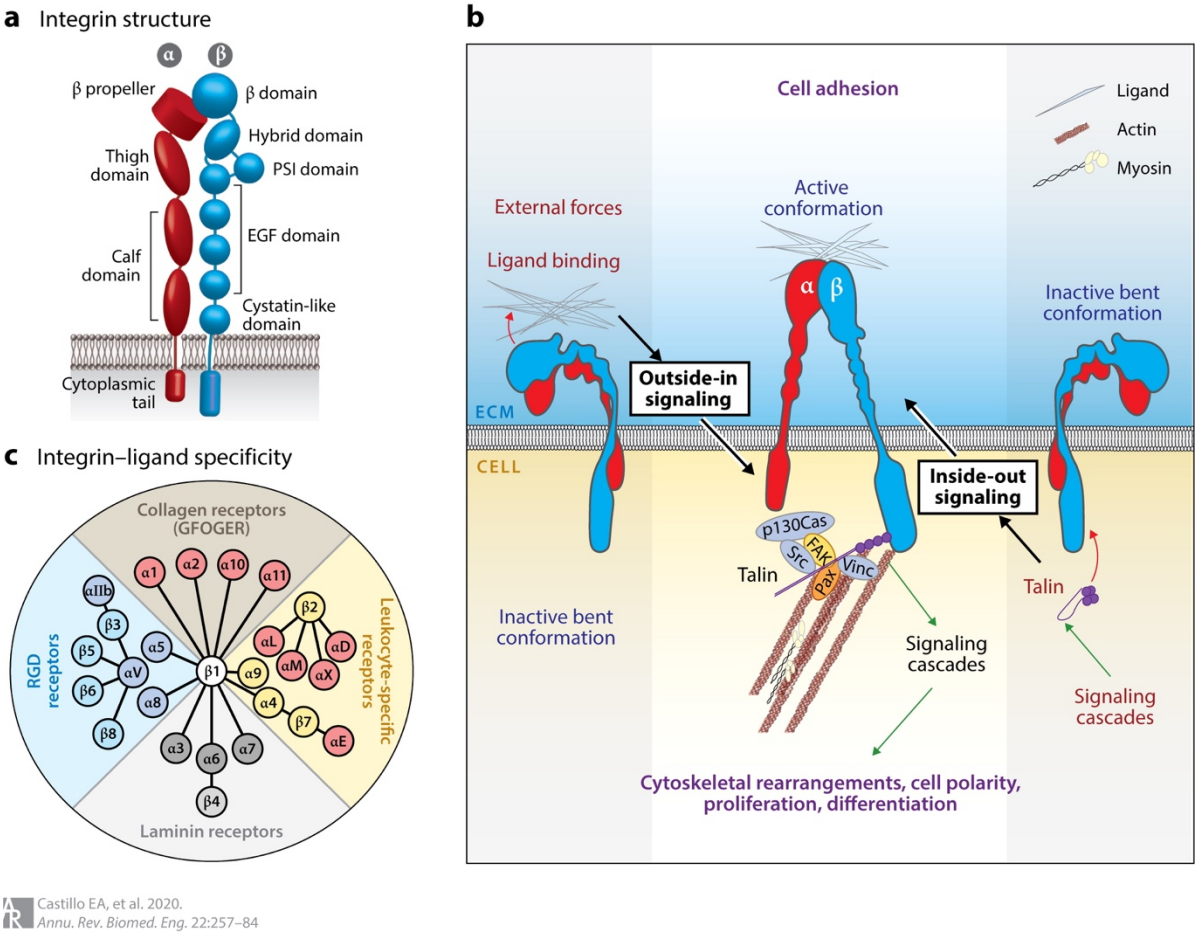

Castillo EA, et al. 2020.
Annu. Rev. Biomed. Eng. 22:257–84

Figure 2-3. Integrins are cell adhesion receptors that serve as mechanical links between the extracellular matrix (ECM) and a cell's cytoskeleton. **(a)** Integrins are transmembrane heterodimers composed of an α and a β subunit. **(b)** Integrins are known as bidirectional signaling receptors that can trigger signaling cascades after externally binding to a ligand (outside-in signaling). Additionally, integrins can be controlled from signaling cascades within the cell (inside-out signaling). **(c)** Integrin subtypes have specific ECM protein ligand-binding properties. Panels adapted with permission from References (a) [74], (b) [75], and (c) [76], respectively.

CM adhesion receptors and the cardiac microenvironment undergo temporal changes during heart development. Differences in integrin expression profiles are frequently observed in embryonic versus adult tissues. During development, CMs display changing integrin expression profiles. The term integrin expression profile refers to the different integrin types and their respective quantities at the cell surface. Distinct integrin types can trigger different intracellular signaling pathways [77]. Furthermore, during heart development the ECM exhibits changes in biochemical and biophysical properties such as biochemical composition as well as mechanical properties and structure. Changes in ECM properties ultimately lead to changes to the myocardium's mechanical properties, which affect heart function. The CM integrin expression profile and surrounding myocardial ECM composition reach a dynamic steady state in adulthood, and upon disease or injury these properties undergo changes in expression and composition.

Embryonic and induced pluripotent stem cells (iPSCs) do not appear to have significant differences, and in this review we refer to both cell types as pluripotent stem cells (PSCs) [78, 79]. PSC-derived CMs (PSC-CMs) are a model that allow the study of cardiac development, disease, and drug modeling. All *in vitro* setups require PSC-CMs to adhere to a substrate. However, cells do not directly interact with the substrate. A cell binds via integrins to specific binding sites on the ECM protein, which we refer to as the cell-ECM interface. The ECM protein is attached to the substrate via physisorption or a chemisorption linker (Figure 2-2b), which we refer to as the protein-substrate interface. We refer to the combination of the cell-

ECM and protein-substrate interface as the cell-substrate interface (also known as the biointerface). How a cell interacts and responds to an *in vitro* microenvironment depends not only on the cell's integrin type and ECM properties but also on the linker and substrate properties.

One of the goals of *in vitro* platforms is to provide stem cells with the appropriate outside-in signaling needed for adhesion, cardiac lineage differentiation, and CM maturity by recapitulating aspects of the native cardiac microenvironment. PSC-CMs display early to late fetal CM characteristics in terms of morphology and function [22, 80]. However, the lack of a suitable adult CM source and known differences between species [4] in terms of key cardiac contractile proteins [81] have motivated researchers to improve PSC-CM models and address the maturity challenge. Multiple *in vitro* approaches have been explored in an effort to increase PSC-CM maturity: electromagnetic stimulation, biochemical factors, physical stimulation (topography, stiffness, stretch), and long-term culture. The resulting models span from single cells to engineered tissues, such as engineered heart tissue, microfluidic heart-on-a-chip, cell sheets, decellularized heart, and muscular thin films [22, 46, 80, 82, 83].

One way to probe and decouple the cell-substrate interface is by using biomaterials to vary different biophysical and biochemical properties [84]. An open challenge for the field is to identify the minimally complex biomaterial model that can support and recapitulate key features of cardiac function in cell and tissue models [85]. Historically, Matrigel™ has prevailed for PSC culture and PSC-CM differentiation, though other synthetic alternatives are emerging. Matrigel's complex

composition of more than 1,000 proteins and lot-to-lot variability complicate attempts to decouple the effects of ECM composition and contributes to heterogeneity in PSC-CM development and response. However, by systematically varying biomaterial properties, researchers are gaining better knowledge of the specific properties of CM differentiation, morphology, structure, function, and maturity.

To facilitate these efforts, we first review native developmental changes in CMs integrin ex- pression and myocardial ECM composition. To support mechanobiological insights, we review strategies for linking ECM proteins to common substrates. Finally, we review a variety of biomaterials approaches that offer control over ligand composition, matrix mechanics (e.g., stiffness), dimensionality (e.g., two versus three dimensions), and matrix structure (e.g., topography) used in CM mechanobiology studies.

2.3. Native Cardiac Development

2.3.1. Temporal dynamics of Cardiomyocyte integrin expression (Development and Disease)

Integrins are heterodimers that consist of an α and a β subunit (Figure 2-3a). The size of individual subunits can range from 80 to 180 kDa. In mammals there are more than 18 α subunit and 8 β subunit types. To date, 24 unique α–β combinations (integrin types) have been identified. Spliced variant isoforms of individual subunits also exist [86]. Different integrin types lead to specific integrin-ligand interactions. However, there is redundancy in the interactions, a specific integrin type can bind to

different types of ligands, and one ligand can have multiple receptors for different integrin types [65]. Specific integrin-ECM combinations (Figure 2-3c) have been extensively documented [77, 87]. The result of ligand binding can be a broad range of signaling cascades within the cell (Figure 2-3b). Integrin function has been studied primarily via knockout animal models, and several functions remain unclear [77]. For example, for fibroblast cells the α_5 β_1 integrin determines adhesion strength, while $\alpha_V\beta_3$ integrin and talin enable mechanotransduction [88]. The integrin expression profile is also known to modulate the spatiotemporal organization of force transmission at cell-matrix adhesions [89]. To bind an extracellular ligand, integrins at the plasma membrane must undergo a conformational change from bent to unfolded (Figure 2-3b). Biochemical and biomechanical integrin regulation affects integrin cell surface availability, binding properties, activation, and clustering [90].

The various methods used to determine integrin expression levels analyze either RNA levels or protein levels. Reverse transcriptase polymerase chain reaction (RT-PCR) provides a measure of the specific amount of target RNA. RNA sequencing provides the whole RNA transcriptome at one time point. A trade-off of these methods is that RNA data do not always translate directly to protein levels. Regulatory processes following the production of messenger RNA contribute to the mismatch between transcription and translation [91]. While some studies use RNA levels to determine integrin expression, others favor the use of antibodies to directly label the protein. Western blot analysis quantifies relative protein expression levels. Immunohistochemistry (IHC) labeling of tissue sections with antibodies confirms

protein expression and preserves the protein's spatial distribution. Fluorescence-activated cell sorting of labeled cells provides the relative protein levels from cell to cell. A caveat with antibodies is that care must be taken to validate and include appropriate controls to ensure the signal comes from the protein of interest and not nonspecific binding [92]. A combination of both RNA and protein data would be the gold standard in integrin expression studies.

In this section, we review CM integrin expression throughout normal cardiac development and describe how it changes with different cardiovascular diseases. Integrins are at the cell-ECM interface and thus are essential to mechanobiological signaling during these remodeling phases [93]. The studies reviewed use various animal models, and we note that differences may exist between species, including in integrin expression. Thus, we provide the model organism in parentheses for clarity.

In early cardiac muscle development, CMs express α_5 and α_6 integrin subunits dimerized with both β_{1A} and β_{1D} (mouse) [94]. The α_5 integrin subunit is replaced by α_7 in adult CMs (mouse) [95]. CM integrin subunit expression undergoes a switch at birth, and $\alpha_{7B}\beta_{1D}$ integrin becomes dominantly expressed (mouse) [94]. Table 2-1 summarizes trends in CM integrin expression throughout development and with disease/injury. The α integrin subunits expressed in CMs also include α_1, α_6, α_9, and α_{10} [59]. In addition to the dominant β_1 integrin subunit, β_3 and β_5 are present in CMs [59].

Table 2-1. Cardiomyocyte integrin expression in cardiac development and disease[a]

Integrin subunit	Embryonic	Fetal	Neonatal	Adult	Disease/injury
α_1		■ R [96]	■ R [96]	× R [96]	↑ R [96, 97]

α_3		■ R [96]	■ R [96]	■ R [96]	→ R [96, 97]
α_5	■ M [94] α_5 is abundantly expressed	■ R [96]	■ R [96]	× M, R [65, 96]	↑ R [96, 97]
α_6	■ M [94, 95] α_6 is abundantly expressed	■ M [95]	■ M [95]		
α_7	■ M [94]	■ M [94]	■ M [94]	■ M [94] α_{7B} is abundantly expressed	↑ M [98]
β_1		■ R, M [94, 96]	■ R [96]	■ R, M, H [96, 99] β_{1D} is abundantly expressed	→ R, A [96, 100] ↑ M [101] ↓ M [102, 103]

[a]All data are from cardiomyocyte protein expression. Myocardial tissue level trends are omitted. Filled squares indicate presence; crosses indicate absence. Upward arrows indicate an increase in expression; downward arrows indicate a decrease in expression; rightward arrows indicate no change in expression. Blank cells indicate no data. Abbreviations: A, rabbit; H, human; M, mouse; R, rat.

2.3.1.1. α_1

$\alpha_1\beta_1$ integrin is associated with cell attachment to collagen and laminin [87]. The α_1 integrin subunit is present in fetal and neonatal CMs (rat) [96]. However, by the time CMs reach adulthood, the α_1 integrin subunit is no longer present (rat) [96]. Induction of cardiac hypertrophy by aortic coarctation revealed increased expression of the α_1 integrin subunit in CMs (rat) [96]. In an induced myocardial infarction (MI) model, the α_1 integrin subunit localized to CMs in the peri-infarcted area and increased from undetectable to detectable levels 1 week post MI and persisted until 6 weeks post MI (rat). Expression of α_1 integrin also increased in apoptotic CMs after MI [97].

2.3.1.2. α_3

$\alpha_3\beta_1$ integrin is known to bind to laminin [87]. Terracio, et al. [96] showed that the α_3 integrin subunit is present in fetal, neonatal, and adult CMs (rat). They induced

cardiac hypertrophy by aortic coarctation and observed no change in α_3 integrin subunit expression levels in CMs (rat) [96]. Nawata, et al. [97] induced MI and observed no change in the level of expression of the α_3 integrin subunit in CMs throughout the 6 weeks after MI (rat).

2.3.1.3. α_5

$\alpha_5\beta_1$ integrin is known to bind to fibronectin [87]. Embryonic CMs express the α_5 integrin subunit, which is found in complex with both β_{1A} and β_{1D} (mouse) [94]. Wiencierz, et al. [95] confirmed that in embryonic CMs the α_5 integrin subunit is strongly expressed (mouse). The α_5 integrin subunit is present in fetal and neonatal CMs (rat) [96]. However, by the time CMs reach adulthood, the α_5 integrin subunit is no longer present (rat, mouse) [65, 96]. Terracio, et al. [96] induced cardiac hypertrophy and observed the return of the α_5 integrin subunit in CMs (rat). Nawata, et al. [97] induced MI and observed a peak in the level of expression of the α_5 integrin subunit in CMs at 4 and 7 days post MI (rat). The level of expression then decreased to levels observed in control groups after 6 weeks post MI (rat). The disparity in temporal dynamics of α_5 and α_1 integrin subunit expression following MI suggests that different α integrin subunits could have different roles in remodeling [93, 97].

2.3.1.4. α_6

$\alpha_6\beta_1$ integrin is known to bind to laminin [87, 104]. Embryonic CMs express the α_{6A} integrin subunit, which is found in complex with both β_{1A} and β_{1D} subunits (mouse) [94]. Wiencierz, et al. [95] confirmed that in embryonic CMs, α_6 is a strongly expressed integrin subunit (mouse). At the tissue level, early in embryonic

development, the α_6 integrin subunit is located primarily in the heart and specifically within the myocardium (mouse), and it is no longer present in the myocardium by birth. Expression of the α_6 integrin subunit is spatially regulated as the heart matures; it is initially downregulated in the ventricles, followed by the atrial regions. The α_6 integrin subunit is also present in early chick myocardium [65]. Recently, atrial and ventricular CM sub-populations were isolated throughout embryonic and adult stages based on differential expression in the α_6 integrin subunit (mouse). Patch-clamp analysis and gene expression profiling confirmed the atrial and ventricular CM subtypes. Expression levels of the α_6 integrin subunit correlated with expression of myosin light chain 2a (MLC-2a) and MLC-2v [95].

2.3.1.5. α_7

$\alpha_7\beta_1$ integrin is known to bind to laminin [87]. Brancaccio, et al. [94] found that the α_{7B} integrin subunit in CMs starts to be expressed at embryonic day (E)17 (mouse). $\alpha_{7B}\beta_{1D}$ integrin is present in developing and adult CMs (mouse) [94]. The onset of α_7 integrin subunit expression in CMs during cardiac muscle development is not temporally coordinated with β_{1D} expression (mouse) [94]. Following birth and in adulthood, the α_7 and β_{1D} integrin subunits are abundantly expressed in CMs (mouse) [94]. Babbitt, et al. [98] demonstrated that the α_7 and β_{1D} integrin subunits in CMs increase in expression 1 week following aortic constriction (mouse).

2.3.1.6. β_1

The β_1 integrin subunit is ubiquitous in many cell types and is present in half of known integrin types [77]. The β_1 integrin subunit is present in fetal, neonatal, and adult CMs (rat) [96]. The initial expression time point of the β_{1D} integrin subunit

varies between studies within the same species. Brancaccio, et al. [94] showed that from E11 to E17 the β_{1A} and β_{1D} integrin subunit variants are coexpressed in CMs (mouse). In contrast, Van Der Flier, et al. [99] showed that β_{1D} integrin subunit expression in CMs begins around the time of birth (mouse). In the developing and newborn heart, β_{1D} can dimerize with several α integrin subunits, including α_5, α_7, and α_{7B} (mouse) [94]. This study showed that β_{1D} is not an exclusive partner to α_{7B}, as was previously thought. As development progresses, β_{1A} subunit expression progressively declines, while β_{1D} subunit expression increases in CMs (mouse) [94]. In newborn and adult CMs, the integrin subunit isoform β_{1D} is the only β_1 subunit expressed (mouse) [94]. Van Der Flier, et al. [99] also showed that the β_{1D} integrin subunit was present at the costameres and intercalated discs of adult CMs (mouse and human). The integrin subunit β_{1D} may provide muscle cells with a stronger mechanical link between the ECM and actin cytoskeleton fibrils [105]. Moreover, in adult CMs, the β_{1D} integrin subunit associates only with the α_{7B} integrin subunit (mouse) [94].

Terracio, et al. [96] induced cardiac hypertrophy and observed no change in β_1 integrin subunit expression levels in CMs (rat). Sun, et al. [106] demonstrated that gene expression of β_1 is temporally upregulated after MI (rat). Additionally, these authors showed that β_{1D} is downregulated by inflammatory cytokines such as tumor necrosis factor. Krishnamurthy, et al. [101] observed an increase in β_1 integrin subunit expression in CMs after MI in comparison to controls (mouse). They also noted that not all CMs exhibit increased β_1 expression. Ichikawa, et al. [100] demonstrated that after 9 weeks of treatment with daunorubicin (a cardiotoxic drug

reducing left ventricular function) the total protein expression of β_{1D} did not change in comparison to controls (rabbit). Manso, et al. [102] showed that loss of talin-2 led to a 50% reduction in levels of β_{1D} in CMs, while normal cardiac structure and function were maintained (mouse). Transgenic mice overexpressing thrombospondin 3 (Thbs3; upregulated in cardiac disease) in CMs showed reduced surface integrin and sarcolemmastability. β_{1D}, α_5, and α_7 integrins from Thbs3 hearts showed reduced membrane presence (mouse). Overexpression of $\alpha_7\beta_{1D}$ integrin reduced Thbs3-related disease and led to a rise in endogenous integrin $\alpha_5\beta_{1D}$ (mouse) [103].

2.3.1.7. Pluripotent stem cell and pluripotent stem cell–cardiomyocyte integrins

Much less is known about the integrin expression of PSC-CMs. PSCs abundantly express α_5, α_6, α_V, β_1, and β_5 integrin subunits [107]. The PSC-CM integrin expression profile has been shown to be temporally modulated. Ja, et al. [108] demonstrated that PSC-CMs express higher RNA levels of α_1, α_2, α_3, α_7, and β_1 integrin subunits than do PSC cardiac progenitors (human). Yu, et al. [109] showed that α_7 integrin subunit expression is lower in PSC-CMs than in neonatal CMs (mouse).

2.3.2. Temporal Dynamics of Myocardial Extracellular Matrix Composition (Development and Disease)

In order to evaluate the native cardiac ECM proteome, samples must be in the form of whole tissue sections or isolated/enriched ECM proteins from tissues. IHC has been used to spatially label ECM proteins within tissue sections. As discussed

above, trade-offs concerning the use of antibodies apply. A few studies have also reported ECM gene expression levels using RT-PCR. Another common technique involves decellularization of the heart and a protein precipitation step, followed by analysis via liquid chromatography in tandem with mass spectrometry (LC-MS/MS) [110]. A drawback of performing decellularization is that some soluble matrix components can be lost or altered during sample processing [111]. Missing low-abundance proteins are a known pitfall of LC-MS/MS [110]. Ongoing challenges in cardiac proteome analysis include the relative insolubility of ECM proteins and the relatively high abundance of other proteins in cardiac tissues [112].

In this section, we review the changes that occur in myocardial ECM composition throughout the normal cardiac development timeline. We also discuss ECM protein structural organization and spatial location within the myocardium (Figure 2-4a). We then describe how the myocardial ECM composition profile is affected by different cardiovascular diseases. Unless otherwise stated, the following discussion describes composition changes within the left ventricle. There exist many differences among species, and while some myocardial ECM composition changes may be the same, we list the model organism in parentheses for clarity. Table 2 summarizes trends in myocardial ECM protein composition in cardiac development and disease. For coverage of other cardiac ECM proteins and composition of other heart compartments, we refer the reader to other excellent detailed reviews [53, 113].

Table 2-2. Myocardial ECM protein composition in cardiac development and disease[a]

ECM protein	Embryonic	Fetal	Neonatal	Adult	Disease/injury
Collagen I	■ M [114]	■ R [115-117]	↓ M [114] ↑ R [115-117]	↑ R [115-117]	↑ R [118, 119] ↓ R [120]

				Collagen I is abundantly expressed	
Collagen III		■ R [116, 117]	↑ R [117]	↑ R [116, 117]	↑ R [118] → R [119] × R [120]
Collagen IV	■ M [114]	■ R [116, 117]	↑ M [114] ■ R [116] ↓ R [117]	■ R [116] ↓ R [117] Collagen IV is a major component of basement membrane	↑ R [119, 120]
Collagen V			■ R [115]	■ R [120]	↓ R [120]
Collagen VI				■ R [121]	↑ R [120]
Collagen XV				■ R [120]	× R [120]
Laminin	■ H [122]	■ R [116]	↑ R [116]	↑ R [116] ■ H [123] Laminin is a major component of basement membrane	↓ R [120] → R [119]
Fibronectin	■ M [114]	■ R [117] Fibronectin is abundantly expressed	↓ R [117] → M [114] Fibronectin is abundantly expressed	↓ R [117]	↑ H, R, M [97, 120, 124-126]
Elastin	■ M [114]		→ M [114]	■ R [119]	→ R [119, 120]

[a]All data are from myocardial left ventricular ECM protein expression. Trends in the disease column reflect the first temporal data point reported. Filled squares indicate presence; crosses indicate absence. Upward arrows indicate an increase in expression; downward arrows indicate a decrease in expression; rightward arrows indicate no change in expression. Blank cells indicate no data. Abbreviations: ECM, extracellular matrix; H, human; M, mouse; R, rat.

2.3.2.1. Collagens

Collagen fibrils are aggregates of triple helices composed of long polypeptide chains called α chains [127]. Individual collagen fibrils, with diameters ranging from 30 to 80 nm, come together to form collagen fibers [127]. The 14 different types of collagen vary in their composition and arrangement of α chains [127]. Collagens I, II, III, V, and XI form fibrils, and the rest are described as nonfibrillar [127]. Collagen is the most abundant ECM protein in the heart. The myocardial collagen matrix is

75-80% collagen I; 11–20% collagen III; and the remaining percentage composed of collagen IV, collagen V, and collagen VI [111, 127]. This ratio of collagen types has also been reported to be conserved among three species (rat, dog, and macaque) [121].

The adult myocardium has a collagen network with a hierarchical structure that evolves during development. Within the endomysium (Figure 2-4a), neighboring CMs are connected by intercellular struts composed of collagen fibrils and anchored near the Z-band level [127]. CMs are next surrounded by interwoven bundles of collagen fibrils, and the perimysium (Figure 2-4a), which contains collagen bundles that surround groups of CMs [127].

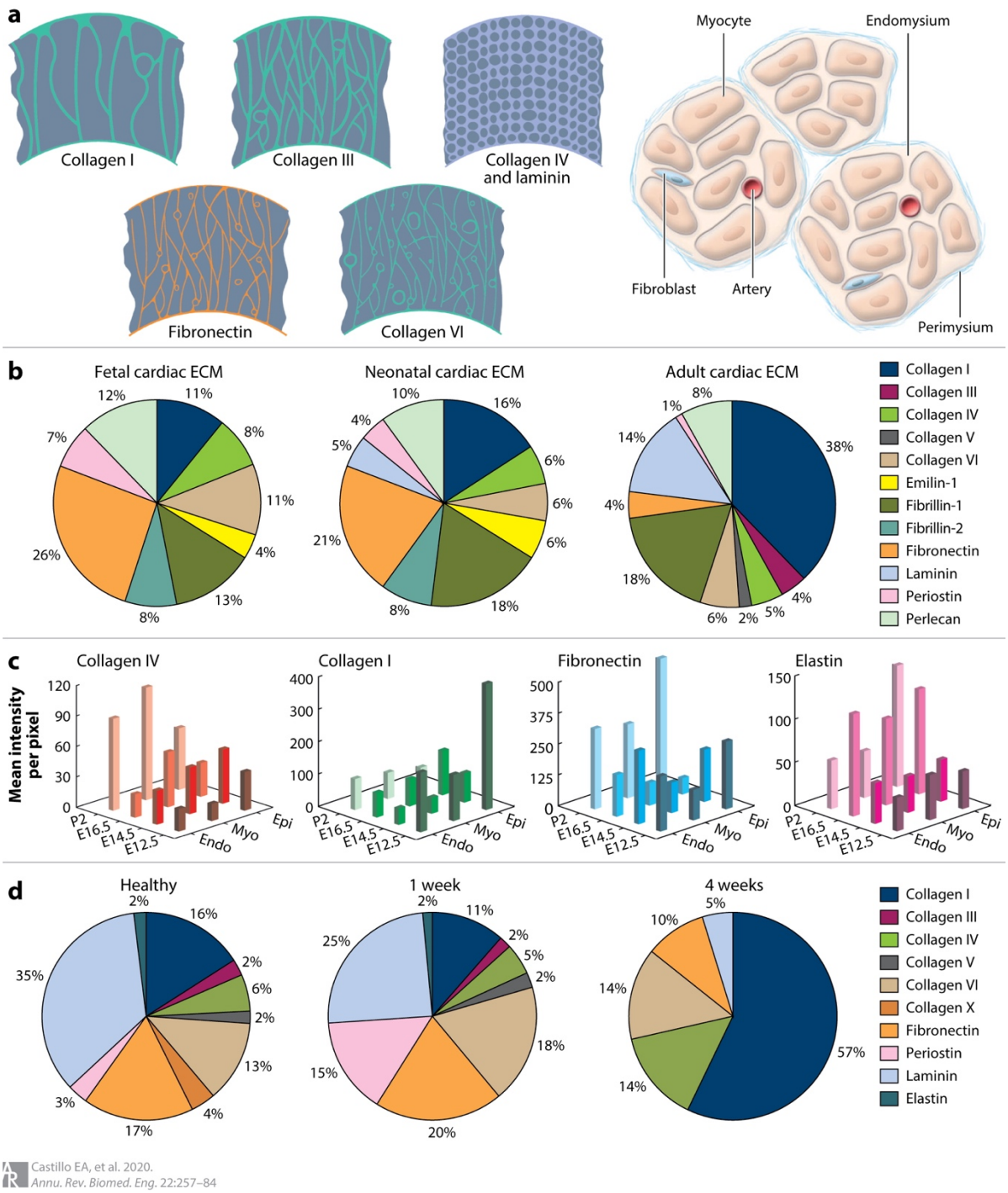

Figure 2-4. (a) The myocardial ECM is composed of a hierarchical network of proteins with distinct dominant spatial distributions. **(b)** The ECM protein composition dynamically changes throughout cardiac development (fetal, neonatal, adult stages). **(c)** ECM compositional changes vary among distinct heart tissue layers (Endo, Myo, Epi) during developmental stages (12.5, 14.5, 16.5, and P2). **(d)** In addition, ECM protein composition dynamically changes after myocardial infarction.

Abbreviations: ECM, extracellular matrix; Endo, endocardium; Epi, epicardium; Myo, myocardium; P2, postnatal day 2. The numbers 12.5, 14.5, and 16.5 refer to embryonic days 12.5, 14.5, and 16.5, respectively. Panels adapted with permission from (a) [111] and [128], (b) [117], (c) [114], and (d) [120].

A changing composition of collagens contributes to the complex mechanical properties and function of the myocardium [127, 129]. Important factors include spatial location and relative alignment, fiber structure and dimension, fiber density, and fiber cross-linking [127, 129]. For example, collagen composition changes dramatically with fibrosis, a compensatory remodeling mechanism that involves changes in the ECM that preserve the tissue's integrity. Many cardiac diseases increase the deposition or rearrange the organization of collagen, and imaging methods sensitive to collagen I and collagen III have been applied to observe this progression [111]. In general, with age, the myocardium's collagen concentration and number of crosslinks increase [127]. This increase in collagen within the myocardium increases muscle stiffness [127].

2.3.2.2. Collagen I

Collagen I is secreted from fibroblasts as procollagen, self-assembles into fibrils after being modified by enzymes, and is stabilized by covalent cross-links across the triple-helix structure [111, 127]. Collagen I fibers are typically composed of thick, densely packed fibrils with an average diameter of 75 nm [127]. At the adult stage, collagen I is located at high abundance in the perimysium and at lower abundance in the endomysium (rat) (Figure 2-4a) [121, 130]. A key role of collagen I is to provide structural support and strength within the myocardium [114, 121]. Collagen I

is a relatively stiff material that exhibits high tensile strength and provides rigidity [127, 131].

When observed for a period extending up to postnatal stage (P)2 (mouse), collagen I expression in the myocardium is highest at E12.5 (Figure 2-4c) [114]. The lower amount of collagen I in the myocardium during initial stages of development is thought to contribute to tissue elasticity during expansion [114]. In contrast, the same study showed that collagen I gene expression increased from E12.5 to P2 [114]. Studies using rat myocardium observed collagen I increasing steadily throughout the fetal, neonatal, and adult stages (Figure 2-4b) [115-117]. As the heart's functional capacity develops to meet the higher workload from E12.5 to P2, the collagen network within the ventricles increases in spatial mesh complexity and fiber structure [114]. After birth, the speed at which the collagen network develops increases drastically, reaching adult structure within 20 days postpartum (rat) [115]. The amount of collagen I does not change within 20 days postpartum [115]. The adult heart has a significantly higher amount of collagen I versus the fetal heart [116]. Collagen I is the most abundant protein in the adult heart (rat) [117].

Aging and several diseases or injuries can cause changes in expression of collagen I. As the myocardium ages, collagen I concentration increases substantially, and the number of fibers and thickness increase as well [111, 127]. Collagen I is crucial for heart tissue repair after injury or disease. If loss of CMs occurs, cardiac fibroblasts are recruited to the damaged region and compensate for muscle loss primarily by secreting collagen I [111]. One study found that collagen I increased at 4 weeks post MI and remained elevated at 10 weeks (rat) [118]. In the

same study, collagen I within the right ventricle peaked at 4 weeks post MI and started to decline toward baseline at 10 weeks [118]. This study highlights the temporal dynamics of the ECM as a function of spatial localization within the heart. One week after MI there was a small decrease in collagen I, but by week 4 the amount of collagen I had increased above healthy baseline values (rat) (Figure 2-4d) [120].

2.3.2.3. Collagen III

Collagen III is a homotrimer that forms a compliant fiber network [111]. Collagen III fibers are typically composed of thin, loosely packed fibrils with an average diameter of 45 nm [127]. Collagen III is secreted by smooth muscle cells and fibroblasts [127].

At the adult stage, collagen III is more abundant in the endomysium and less so in the perimysium (Figure 2-4a) [121]. Collagen III exhibits high tensile strength, contributes to structural support, and provides elasticity [127, 131]. A metric of relative stiffness within cardiovascular tissue is the ratio of collagen I to collagen III. This ratio is high during the human neonatal stage and contributes to a rigid heart during early development, then decreases after birth and reaches a steady state in adulthood [131]. A crucial function of collagen III is regulation of collagen I fibrillogenesis, making it necessary for normal cardiovascular development [111, 116].

Collagen III significantly increases as the heart matures from the fetal to adult stage (rat) [116]. A rat study showed an increase in collagen III concentration from the fetal to the neonatal to the adult stage (Figure 2-4b) [117]. Collagen III

transiently increased at 2 weeks post MI, then declined to baseline values at 4 weeks (rat) [118]. In another recent MI study, collagen III did not significantly change expression over the 8-week observation time (rat) [119]. The variations in temporal expression in these two studies could be due to differences in sample preparation and analysis [119]. In another adult rat MI study, collagen III was no longer present 4 weeks post MI (Figure 4d) [120].

2.3.2.4. Collagen IV

Collagen IV is nonfibrillar, with three heterotrimer variants composed of six different α chains [111]. Both cardiac fibroblasts and CMs secrete collagen IV [70]. In adult myocardium, collagen IV is confined to the basement membrane of myocardial, endothelial, and smooth muscle cells (Figure 2-4a) [121]. The basement membrane is rich in collagen IV [132]. Furthermore, collagen IV is present along the T-tubular network and is thought to provide structural support during contraction [113, 130]. Collagen IV serves as a cell-adhesive protein and links groups of CMs to the surrounding ECM [127].

Collagen IV increases in density and organization from E12.5 to P2 (mouse) (Figure 2-4c) [114]. At E14.5, collagen IV surrounds CMs in a disconnected circular configuration. By the postnatal stage, the collagen IV network was more interconnected throughout the myocardium and has a more fibrillar structure [114]. Within 3 days of birth, the collagen IV network becomes denser in the endomysium [115]. Collagen IV does not undergo any significant changes in expression during the fetal, neonatal, or adult phase (rat) [116]. Conversely, another study showed that collagen IV decreases during fetal, neonatal, and adult phases (rat) (Figure 2-

4b) [117]. After MI, the amount of collagen IV increased, reached a maximum at 2 weeks post MI, and then progressively decreased (rat) [119]. In another adult rat MI study, at week 4 the amount of collagen IV remained above healthy baseline values (Figure 2-4d) [119].

2.3.2.5. Other Collagen Types

Other collagens found in cardiac tissue include collagen V, collagen VI, and collagen XV. In a postnatal rat model, collagen V is located in the endomysium and basal lamina (a component of the basement membrane) [115]. In an adult rat MI study, collagen V was no longer present 4 weeks post MI [120]. In adult rat myocardium, collagen VI is abundant in the endomysium and less in the perimysium (Figure 2-4a) [121]. In an adult rat MI study, 1 week post MI there was a small increase in collagen VI, and by week 4 the level approached healthy baseline values (Figure 2-4d) [120]. Furthermore, a knockout study found that a collagen VI-deficient mouse had a reduction in chronic CM apoptosis and fibrosis compared with wild-type mice, which led to improved cardiac function after MI [133]. Collagen XV is involved with ECM organization within the heart [134]. In an adult rat MI study, collagen XV was no longer present 4 weeks post MI [120].

2.3.2.6. Laminin

Laminins are a family of glycoproteins that form a T-shaped heterotrimer and are composed of one α, one β, and one γ chain [111]. Fibroblasts and CMs can secrete laminin [70]. Laminin is found in the basement membrane of cardiac tissue and vasculature [121]. Laminin forms a fine network and is a major component of the basement membrane (Figure 2-4a) [132, 135]. The basement membrane in adult rat

cardiac ventricles has a striated laminin structure with a length similar to that of sarcomeres [132]. Laminin is the first ECM protein observed in the developing embryo and has an essential role in anchoring cells to ECM [135]. Another function of laminin is to cross-link other ECM proteins, including collagen IV, perlecan, and entactin [136].

Tissues from humans at gestational week 8 showed that the laminin β_1 and laminin β_2 chains are present in the ECM surrounding CMs [122]. In a rat model, the amount of laminin significantly increased during the fetal, neonatal, and adult phases [116]. Another rat study confirmed the increase in laminin from the fetal to the neonatal to the adult stage (Figure 2-4b) [117]. Transcriptome expression data of adult myocardium indicate abundant expression of laminin-221, and protein studies confirmed its presence (human) [123]. In an adult rat MI study, 1 week after MI there was a decrease in laminin, which was further reduced by the fourth week (Figure 2-4d) [120]. In another recent rat MI study, the amount of laminin did not significantly change over the 8-week observation period [119].

2.3.2.7. Fibronectin

Fibronectin is a glycoprotein with a rodlike structure that is composed of two subunits connected by disulfide bonds [111]. The subunits consist of repeating modules (types I, II, and III). At the adult stage, fibronectin is more abundant in the endomysium and less so in the perimysium (Figure 2-4a) [121]. It is generally thought that fibronectin has a role in connecting the surface of CMs to the endomysium [115]. Fibronectin plays an essential role during cardiac development via adhesion, migration, and differentiation, and it also plays a beneficial role during

the wound healing process [111, 124, 137]. Combinations of different subunits allow fibronectin to have different cell-binding properties and to cross-link with other ECM components [114]. Fibronectin has a strong affinity for collagen III and also binds to collagen I, fibrin, heparin, and syndecan [114, 115].

In rat myocardium, fibronectin was the most abundant protein in the fetal and neonatal stages (Figure 2-4b) [117]. The amount of fibronectin decreases significantly from fetal to adult age (Figure 2-4b) [111, 116, 117]. The organization of fibronectin increases during early stages of development. In mouse myocardium, at E14.5 fibronectin formed thin, isolated fibrils, and by P2 the network had become more interconnected [114]. Throughout the observation window of these early time periods (E14.5–P2), the amount of fibronectin remained relatively constant (Figure 2-4c) [114]. A study in a human heart after MI showed that fibronectin deposition rapidly increased within and around the infarcted area from 12 h to 14 days post MI [125]. Accumulation of fibronectin was also observed in a rat model 4-35 days post MI [124]. Results from another adult rat MI study showed a small increase in fibronectin 1 week post MI [120]. By 4 weeks post MI, the amount of fibronectin was below control values (Figure 2-4d) [120]. Following similar trends, a rat MI study showed fibronectin increasing in the peri-infarcted area 1 week post MI, and 6 weeks post MI expression decreased [97]. In a mouse pressure overload study, fibronectin accumulation increased over 4 weeks [126].

2.3.2.8. Elastin

Elastin is composed of tropoelastin monomers that contain alternating hydrophobic and hydrophilic domains [111]. Within the myocardium, elastin is

located within the interstitium and in the walls of coronary blood vessels [129]. A major structural function of elastin is to provide elasticity to the myocardium during cyclic loading [114]. Furthermore, elastin is essential to heart development and vasculature.

In the developing mouse myocardium (E12.5–P2), levels of elastin remained constant, with a transient peak at E16.5 (Figure 2-4c) [114]. At P2, elastin in the myocardium was organized into fibrils [114]. The transient elastin peak is thought to provide the elasticity needed to accommodate the increased growth and workload [114]. It is also thought that the relative decrease in elastin after birth may contribute to the maturation of CMs and their sarcomeres [114]. In a rat study, the elastin concentration did not significantly change throughout the 8 weeks after MI [119]. In another adult rat MI study, the elastin amount was unaltered 1 week post MI, and by 4 weeks post MI, elastin was no longer detected (Figure 2-4d) [120]. Post-MI mouse models indicate that fibrotic tissue is composed mostly of collagen I but also elastin, with tropoelastin significantly increased between 7 and 21 days post MI [138]. The role of elastin during fibrosis is to preserve elasticity.

2.4. *In vitro* protein-substrate interface

In vitro CM mechanobiology studies allow researchers to probe a cell's intrinsic properties and quantitatively measure its response. One way in which the *in vitro* cell-substrate interface differs from the native cell microenvironment is that the ECM protein is attached to the substrate via a linker (Figure 2-2a, 2-2b). Two common substrates in mechanobiology studies are polyacrylamide (PA) hydrogels and

polydimethylsiloxane (PDMS) [139, 140]. We review various linking strategies used to attach ECM proteins to the substrate and discuss differences in binding strength to the substrate.

2.4.1. Polyacrylamide Hydrogels

PA hydrogels are made up of a network of cross-linked acrylamide monomers. PA hydrogel properties, including stiffness and porosity, are determined by monomer and cross-linker concentration [34]. These variables can be tuned to create PA hydrogels with a wide range of physiologically relevant stiffnesses, useful for mechanobiology studies. Here we review methods used to attach proteins to PA hydrogel surfaces.

2.4.1.1. Covalent chemistries to bind proteins to polyacrylamide hydrogels

Attaching ECM proteins to the surface of a PA hydrogel for mechanobiology studies is nontrivial. The ECM protein is commonly attached to a substrate via physisorption or a chemisorption linker. PA hydrogels have no ability to adsorb protein [27]. PA hydrogel copolymerization with ECM proteins enables the proteins to be present at the surface or distributed throughout the network [28, 29]. Copolymerization is beneficial because it bypasses the need for surface modifications to attach proteins. However, the exact linking mechanism of copolymerization is not known. PA hydrogels must be modified in order to use a chemisorption linker to attach proteins.

Many protein adhesion methods create covalent bonds between the protein and the substrate via side chains that are introduced to the surface of the PA hydrogel.

Covalent attachments are the most secure way to bind proteins to PA hydrogels [141]. Sulfosuccinimidyl 6-(4′-azido-2′-nitrophenylamino)hexanoate (sulfo-SANPAH) is frequently used as a covalent linker between proteins and PA hydrogels [142-144]. Sulfo-SANPAH is a heterobifunctional cross-linker with a phenylazide and a *N*-hydroxysuccinimide (NHS) ester group. When activated by light, the phenylazide group binds to any chemically stable molecule (including the PA substrate) via a nonspecific covalent bond. The NHS ester group on the other end of the cross-linker binds to the amines in the protein [145]. Another surface modification method used to bind proteins to PA hydrogels involves hydrazine hydrate. Hydrazine hydrate is a reducing agent that converts inert amide groups on the surface of the PA hydrogel into hydrazine groups, which readily react to form covalent bonds with the aldehyde or ketone groups in proteins [34].

Linkers can also be added to the PA precursor solutions and dispersed throughout the hydrogel. Many of them work in a similar manner as sulfo-SANPAH, in that a linker forms a bond to amines in the protein's backbone. Examples include NHS acrylate [146], 6-acrylaminohexylaminohexanoic acid *N*-succinimidyl ester (N6) [147], and 1-ethyl-3-(3-dimethylaminopropyl)carbodiimide (EDC) [29]. NHS acrylate and N6 add ester groups that bind to amines in the protein's backbone [147], while EDC is used to add carboxylic groups that bind to a protein's amine backbone [29].

2.4.2. Polydimethylsiloxane

PDMS is a silicone-based polymer made by mixing prepolymer with a cross-linker. PDMS is low cost, transparent, and readily molded into various geometries

and setups, making it a versatile substrate for mechanobiology studies. Due to its hydrophobic nature, PDMS does not bind specifically to proteins well [148]. Here we discuss different methods used to attach proteins to PDMS substrates.

2.4.2.1. Adsorption of proteins onto polydimethylsiloxane

Physisorption is a common means of attaching proteins to PDMS substrates [140, 149-156]. Plasma surface treatment of the PDMS is used to encourage protein adsorption. Oxygen plasma inundates the PDMS surface, resulting in silanol groups that make the surface hydrophilic and increase protein adsorption [154, 155, 157]. PDMS surface roughness does not change upon plasma treatment; however, after protein absorption the surface becomes rough [156]. Plasma treatment alone can be used to adhere specific cell types directly to PDMS. Cells adhere selectively to plasma oxidation–patterned regions [158]. The protein-substrate interactions caused by adsorption are weak van der Waals bonds [159]. The bond strength of adsorbed proteins on PDMS is around 1 kN/m^2, and cells exerting a higher traction force can break this bond and detach [160].

2.4.2.2. Covalent chemistries to bind proteins to polydimethylsiloxane

Methods of bonding proteins to PDMS surfaces rely on adding reactive groups to the surface [148, 161, 162], which allows for the formation of covalent bonds between the protein and substrate. A common strategy employed with PDMS uses two molecules; the first molecule adds amine groups to the PDMS surface, and the second molecule links the added amine groups to the protein. A combination of (3-aminopropyl) triethoxysilane (APTES), which adds amine groups to the PDMS substrate, and glutaraldehyde (GA), which links the amine groups to the protein, is

frequently used in such strategies [148, 161]. This specific combination has been utilized to bind various proteins, including collagen [161], Protein A [150], and fibronectin [161]. Other molecules that can be used in place of GA include ascorbic acid [162] and EDC [148]. Distinct chemisorption linkers lead to differences in attached protein density. The protein attachment methods can be ranked from highest to lowest protein density as follows: APTES/EDC, APTES/GA, GA, and physisorption [148].

Another protein attachment method involves adding reactive groups throughout the PDMS prepolymer mixture. Phospholipids conjugated to functional groups can serve as chemisorption linkers. Some phospholipids will be exposed on the PDMS surface and can present functional groups to bind proteins [163].

Sulfo-SANPAH is commonly used to functionalize proteins on PDMS substrates. However, it does not covalently bind proteins to PDMS, as discussed in the following section [144].

2.4.3. Bond strength of the Linker at the Protein-Substrate Interface

In both PA hydrogel and PDMS substrates, chemistries are used to covalently bind proteins to the substrate. Protein attachment is essential for stable and consistent culture of cells on the substrate. Adhesion between protein and substrate can regulate cell behavior [160]. A mechanical test machine measured the protein–substrate binding strengths to be 1.28 kN/m^2 and 11.9 kN/m^2 for proteins adsorbed and covalently bound to PDMS, respectively. Focal adhesion size and actin cytoskeleton organization were higher in covalently versus adsorption-bound substrates [160].

Characterization of the protein-substrate interface and binding strength of the linker to the substrate can be used to compare cellular responses among different substrates and linkers. Protein-substrate adhesion strength can be varied with different linker strategies. As discussed above, the linker sulfo-SANPAH forms covalent bonds with the PA hydrogel network. Characterization via atomic force microscopy demonstrated that proteins cannot be covalently bound to PDMS via sulfo-SANPAH, because PDMS does not contain free amines [144]. This study also showed that ultraviolet treatment of PDMS in the presence of sulfo-SANPAH does not add amine groups to the surface or change the strength of the bond between PDMS and protein (Figure 2-5a). Instead, PDMS can be treated with APTES, resulting in the addition of primary amines on the surface that then react with the sulfo-succinimidyl group of sulfo-NHS-biotin to form a covalent bond (Figure 2-5c). PA hydrogel/sulfo-SANPAH/collagen has a binding strength comparable to that of PDMS/APTES+sulfo-NHS-biotin (Figure 2-5b).

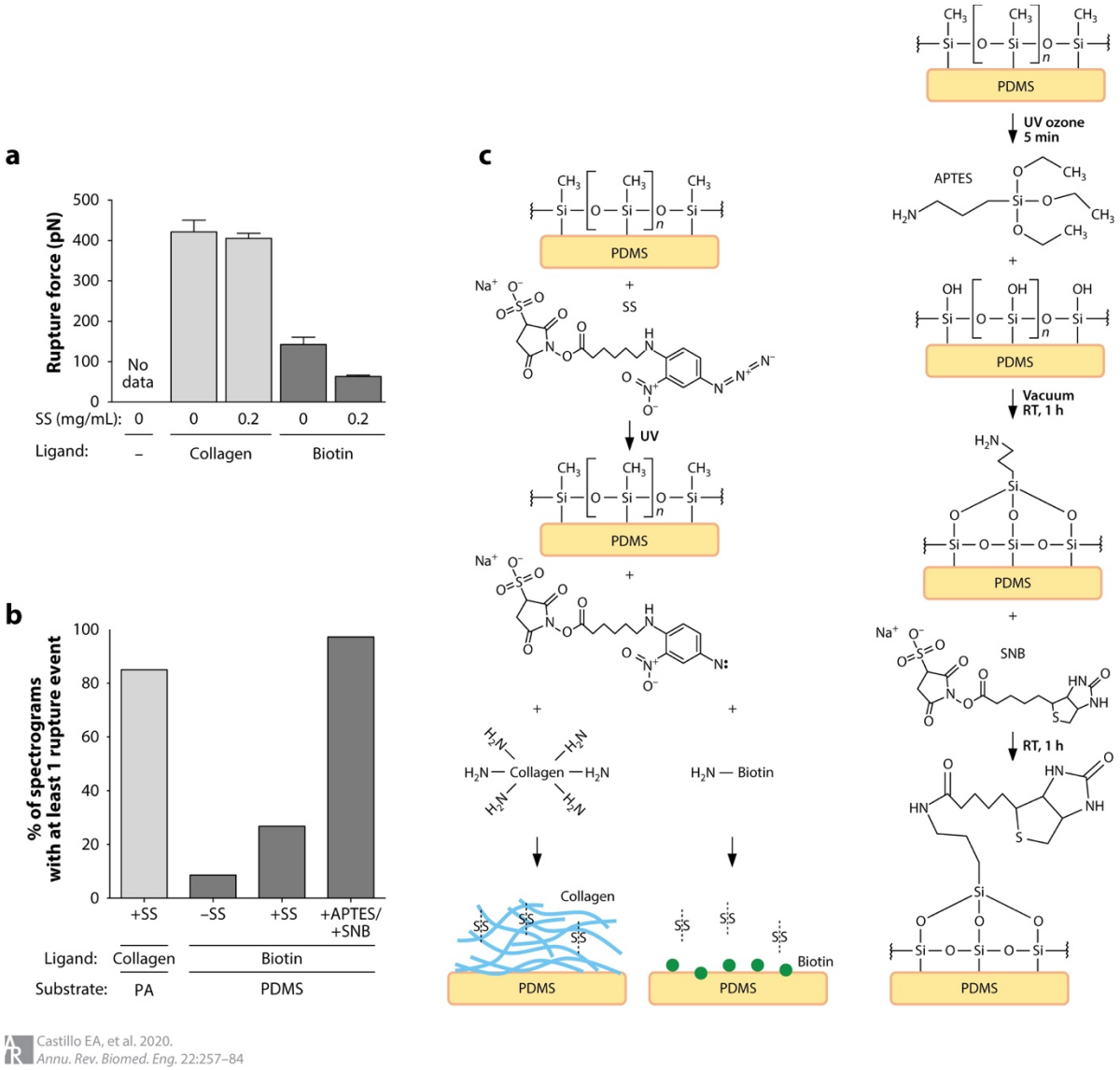

Castillo EA, et al. 2020.
Annu. Rev. Biomed. Eng. 22:257–84

Figure 2-5. Characterization of the binding strength of the protein–substrate interface can be utilized to compare mechanobiology results across various cell–substrate interface platforms (e.g., PDMS versus PA hydrogel). **(a)** Functionalizing PDMS with or without sulfo-SANPAH (SS) does not change the rupture force suggesting collagen nonspecifically adsorbs to PDMS. **(b)** Different substrate and linker combinations lead to differences in binding strength of the protein–substrate interface. **(c)** Chemical groups and residues available at the substrate interface, linker, and ECM protein. Diagram for PDMS treated with SS and APTES/SNB linker. Abbreviations: APTES, (3-aminopropyl) triethoxysilane; ECM, extracellular matrix; NHS, N-hydroxysuccinimide; PA, polyacrylamide; PDMS, polydimethylsiloxane; RT, room temperature; SNB, sulfo-NHS-biotin; sulfo-SANPAH,

sulfosuccinimidyl 6-(4′-azido-2′-nitrophenylamino)hexanoate; UV, ultraviolet. Figure adapted from [144].

2.5. *In vitro* biomaterials approaches to recapitulate the cardiomyocyte microenvironment

The microenvironment's biochemical and biophysical properties modulate CM adhesion, morphology, differentiation, cytoskeleton structure, mechanical output, contractility, and degree of maturity. Biomaterials can be leveraged to systematically tune the properties of a cell's microenvironment [84]. The complexity of cell-adhesive domains, reproducibility, and tunability is a function of biomaterial sources (naturally derived, hybrid/semisynthetic, fully defined) [164]. Decellularized cardiac tissue incorporates the complexity of native myocardium's ECM composition and structure but offers limited ability to modulate the cell-substrate interface [164-167]. For a more in-depth discussion of biomaterial approaches designed to support CM differentiation and maturity, we direct the reader to several excellent reviews [168-170]. In the following subsections, we review biomaterial approaches to the control of ligand composition, matrix mechanics (e.g., stiffness), dimensionality (e.g., two versus three dimensions), and matrix structure (e.g., topography) used in CM mechanobiology studies.

2.5.1. Ligand Composition

Ligand composition influences both cell adhesion and differentiation toward specific lineages. The native myocardial ECM composition changes throughout cardiac development. ECM ligand composition *in vitro* can be varied by using individual or a combination of ECM protein types. Ligand composition can influence

CM adhesion. Borg, et al. [171] observed that adult rat CMs adhere more efficiently to laminin and collagen IV than to other proteins, while neonatal CM adhesion does not depend on protein type. Changes in integrins and other ECM receptors are likely responsible for these observed differences in cell adhesion [111]. Burridge, et al. [11] compared multiple defined proteins, including recombinant human E-cadherin, recombinant human vitronectin, recombinant human laminin-521, truncated recombinant human laminin-511, and vitronectin peptide. All of them supported efficient PSC cardiac differentiation; however, the laminin-based proteins best supported long-term (day 15+) adhesion of PSC-CMs. Differences in integrin-ECM protein interactions are thought to be responsible for the observed CM adhesion. Human recombinant laminin-211 also supports small-molecule-based PSC cardiac differentiation [172]. Patel, et al. [173] identified specific chemical moieties in three fully synthetic polymers, $C2H6N^+$ (amine), $C5H5O^+$ (furan ring), and $C10H17^+$ (isobornyl ring), that promoted greater PSC-CM adhesion and spread area. The synthetic polymers ionically interacted with the PSC-CMs.

Other studies showed that ligand composition can influence differentiation toward a specific cell lineage [59]. Battista, et al. [174] placed mouse PSCs within three-dimensional (3D) semi-interpenetrating polymer networks composed of collagen I and various amounts of fibronectin or laminin. Addition of laminin increased the PSCs' ability to differentiate into beating CMs, whereas addition of fibronectin stimulated endothelial cell differentiation. Jung, et al. [175] utilized 1-kPa poly(ethylene glycol) (PEG) hydrogels to entrap murine PSCs and a mixture of ECM proteins. Using a design-of-experiments approach, these authors found that the

optimal composition to induce *in vitro* cardiac differentiation without additional soluble factors was 61% collagen I, 24% laminin-111, and 15% fibronectin.

2.5.2. Stiffness

Matrix stiffness influences cell contractility, cytoskeleton structure, differentiation, and adhesion area [176, 177]. During cardiac development, the stiffness of native myocardial tissue increases from 1 kPa at the embryo stage to 10-15 kPa at the adult stage [38, 178]. After MI, the stiffness increases to 35-70 kPa [37]. Substrate stiffness can alter CM contractility and cytoskeleton structure. By tuning PA hydrogel stiffness, Engler, et al. [179] demonstrated that embryonic CMs on substrates with a physiologically relevant stiffness (11-17 kPa) promoted actomyosin striation and optimal work transfer to deform the substrate. However, embryonic CMs on stiffer substrates (34 kPa) had fewer myofibril striations, overstrained themselves, and stopped contracting, whereas embryonic CMs on softer substrates (1 kPa) contracted but did not transfer work to the substrate. Chung, et al. [180] observed a temporal regulation of PSC-CMs' spontaneous contractility depending on the 3D hydrogel's cross-linking density (inherently varying stiffness). At the lowest crosslink density (0.45 kPa), the PSC-CMs began to spontaneously contract at day 1. In contrast, within the highest cross-link density (2.4 kPa), contraction was delayed until day 6. Hirata & Yamaoka [181] examined the role of substrate stiffness (9-, 20-, and 180-kPa PA hydrogels; tissue culture polystyrene) on mouse PSC cardiac differentiation. The cells on tissue culture plastic exhibited the highest expression of early cardiac differentiation marker genes. By contrast, the 20-kPa PA hydrogels showed the highest expression of

cardiac contraction-related genes. These results suggest that a single culture substrate is not optimal for the various stages of cardiomyocyte differentiation. Kong, et al. [182] demonstrated that substrate stiffness modulates indirect cardiac reprogramming of mouse embryonic fibroblasts. Mechanoresponsive signals (cell traction, cell area, Yes-associated protein) were able to predict cardiac reprogramming better than individual material properties (matrix modulus, ligand density, ligand type). Corbin, et al. [177] developed a platform to instantaneously tune and reverse substrate stiffness (range 10-55 kPa) with magnetic fields. PSC-CMs seeded on soft and stiff substrates exhibited a small (2,600 μm^2) and a large (4,800 μm^2) spread area, respectively. The starlike shape of the PSC-CMs did not change with substrate stiffness.

2.5.3. Dimensionality: Two Versus Three Dimensions

Dimensionality can influence cell differentiation and degree of maturity. CMs natively exist within a 3D microenvironment. Branco, et al. [183] demonstrated that cardiac differentiation of PSCs in a 3D microwell undergoes faster structural and functional maturation than in two-dimensional (2D) culture. Kerscher, et al. [184] examined cardiac differentiation while PSCs maintained continuous 3D engagement with a PEG-fibrinogen hydrogel. Using the same small-molecule differentiation protocol, these authors found that 2D and 3D cultures showed similar differentiation efficiency, cardiac gene expression, and calcium handling. PSC-CMs within the 3D hydrogel developed ultrastructural maturation, which was confirmed by the presence of transverse tubules on and after day 52. Zhang, et al. [185] showed that PSC-CMs in a 3D microenvironment exhibited enhanced structural and functional

maturation compared with 2D. Lemoine, et al. [186] investigated differences in PSC-CM maturity within 2D and 3D cultures. PSC-CMs placed within a 3D microenvironment had upstroke velocities, morphology, and sodium current densities that were more physiologically relevant and similar to adult CMs in comparison to PSC-CMs in a 2D monolayer culture.

2.5.4. Topography

Topography can influence cell differentiation and maturation. The myocardial ECM contains a network of densely packed, aligned collagen I fibrils with an average diameter of 75 nm [127]. Carson, et al. [187] designed polyurethane acrylate nanoscale structures with various groove widths to probe the role of nanotopography. PSC-CM organization and structural maturation were controlled by nanogroove width in a biphasic manner. CM structural maturation indicators such as cell area, perimeter, alignment, circularity, and sarcomere length were improved using 700-1,000-nm widths. Seo, et al. [188] observed CM differentiation promoted in multipotent mesodermal precursor cells on 200-280-nm-diameter polystyrene nanopillars. Abadi, et al. [189] transferred primary human CM micro- and nanoscale topography features onto a PDMS substrate. The authors then showed that these submicrometer topographies on PDMS influence PSC-CMs' differentiation rate and maturity. Protein adsorption on PDMS is known to be influenced by topography; thus, special care must be taken to decouple properties such as protein density and topography [190].

2.6. Summary and Future Directions for Controlling the Microenvironment of Cardiomyocytes via Biomaterials

The goal of mimicking different components of the native cardiac microenvironment is to recapitulate the desired CM responses *in vitro*. Knowledge of what integrin types CMs use to natively interact with their microenvironment can be used to rationalize the design of specific binding sites in a biomaterial. Outside-in signaling allows the ECM to control integrin expression [191] and, thus, downstream mechanical signaling. Most *in vitro* CM mechanobiology platforms have focused on cell-ECM interactions, but opportunities exist to vary and probe the nature of the ligand and its attachment, as well as the role of cell-cell interactions. For example, myocardial tissue samples demonstrate the prevalence of intercalated discs whereby neighboring cells form physical and electrical connections. Connexin-43 and N-cadherin are, respectively, the most common gap junction protein and adherens junction protein expressed in CMs [80, 192]. Studies of pairs of CMs on hydrogels found that the cell-cell interface transitioned from dominantly cell-ECM to cell-cell adhesion proteins over time [41]. CMs on N-cadherin-coated PA hydrogel sustained forces similar to those of CMs on ECM-coated substrates, but they had different cytoskeleton architectures [18]. CMs can also be mechanically coupled via underlying substrate deformations and can experience long-term modification after the mechanical stimulus is removed [193].

Current *in vitro* approaches lack temporal changes in the microenvironment's biochemical and biophysical properties that recapitulate heart development, and PSC-CMs exhibit properties of early to late fetal CMs [80]. Thus, localized control of

ligand type and placement, and of stiffness and cyclic stretch, would enable more precise studies of the variations and dynamics in the myocardium. Temporal and reversible control over biochemical and biophysical properties will better allow researchers to mimic heart changes in the microenvironment during development or a disease state. An open question in the field is whether mimicking the evolution of the cardiac environment *in vitro* can increase the maturity and utility of PSC-CM models. More research is needed to control and tune specific biointerface properties; to quantify biomaterial and cell-adhesive properties; and to enable precision studies of the role of cardiac cell-ECM and cell-cell interactions in development, homeostasis, and disease.

3. Wafer-Scale Patterning of Protein Templates for Hydrogel Fabrication

This chapter is reprinted and reformatted from the following: Kim, A. A., Castillo, E. A., Lane, K. V., Torres, G. V., Chirikian, O., Wilson, R. E., Lance, S. A., Pardon, G., and Pruitt, B. L., “Wafer-Scale Patterning of Protein Templates for Hydrogel Fabrication”. Micromachines, 12(11):1386, 2021. [51], CC by license: https://www.mdpi.com/openaccess. This chapter includes the entire manuscript, including figures and tables. In this chapter, I describe a study I performed as co-first author (with Dr. Anna Kim and Dr. Erica Castillo) on scaling up a photoresist lift-off protein patterning technique developed in the Pruitt lab. We scaled up the lift-off patterning method, which increases yield and reduces variability, from 1 to 16 devices per run. We found that with the scaled patterning, we can transfer the pattern to a polyacrylamide hydrogel and culture hiPSC-CMs as efficiently as with the unscaled approach. As co-first author I led the experimental work focusing on protein transfer to polyacrylamide hydrogel and hiPSC-CM culture. I contributed to the writing and editing of the manuscript and the design of the manuscript figures.

3.1. Abstract

Human-induced pluripotent stem cell-derived cardiomyocytes are a potentially unlimited cell source and promising patient-specific *in vitro* model of cardiac diseases. Yet, these cells are limited by immaturity and population heterogeneity. Current *in vitro* studies aiming at better understanding of the mechanical and chemical cues in the microenvironment that drive cellular maturation involve

deformable materials and precise manipulation of the microenvironment with, for example, micropatterns. Such microenvironment manipulation most often involves microfabrication protocols which are time-consuming, require cleanroom facilities and photolithography expertise. Here, we present a method to increase the scale of the fabrication pipeline, thereby enabling large-batch generation of shelf-stable microenvironment protein templates on glass chips. This decreases fabrication time and allows for more flexibility in the subsequent steps, for example, in tuning the material properties and the selection of extracellular matrix or cell proteins. Further, the fabrication of deformable hydrogels has been optimized for compatibility with these templates, in addition to the templates being able to be used to acquire protein patterns directly on the glass chips. With our approach, we have successfully controlled the shapes of cardiomyocytes seeded on Matrigel-patterned hydrogels.

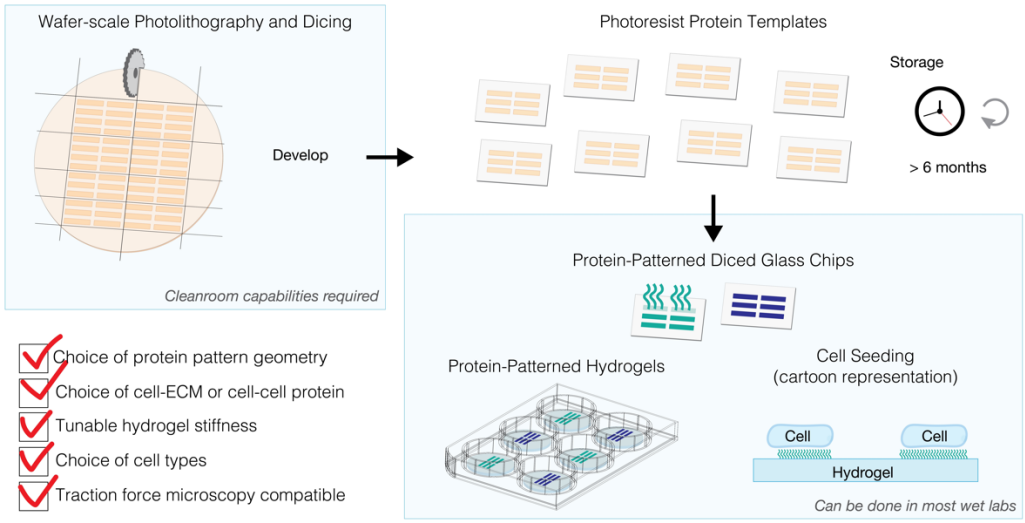

Figure 3-0. Wafer-scale protein patterning graphical abstract.

3.2. Introduction

Human-induced pluripotent stem cell-derived cardiomyocytes (hiPSC-CMs) have gained significant traction over the last decade as a powerful model for understanding cardiac development, modeling cardiac diseases, drug screening, and cardiotoxicity screening [194]. hiPSCs have become more widely used because primary adult cardiomyocytes (CMs) do not regenerate and present difficulty when creating *in vitro* cultures [195]. hiPSC-CMs are derived from patient somatic cells, reprogrammed to a pluripotent state, and then differentiated into cardiomyocytes [13]. They hold great promise for personalized medicine and can be genetically edited to display various mutations linked to diseases, making them an attractive model [196]. Despite the potential of hiPSC-CMs as powerful models, they are limited by the immaturity and heterogeneity that is observed not only across different lab groups and lab members, but also across batches, even when using the same protocols [194]. hiPSC-CMs display a fetal-like phenotype in terms of a sarcomere structure, t-tubule organization, metabolism, calcium handling and overall morphology [22]. Current methods to improve CM maturity include a prolonged culture time, the addition of biochemical cues, biophysical stimulation, altering substrate stiffness and/or extracellular matrix (ECM) proteins [22, 197]. The *in vitro* microenvironment can have a drastic effect on hiPSC-CM maturation and promote a more adult, rod-like CM structure and organized sarcomeres [197]. Amongst the most common methods currently used to culture hiPSC-CMs *in vitro*, one features a monolayer of CMs cultured on polystyrene tissue culture plastic that has been physisorbed with ECM proteins such as laminin, fibronectin, collagen, or Matrigel [198-200].

Tunable micropatterned protein platforms for cell cultures are becoming widely used to manipulate cells because they can control cellular spatial organization and mimic properties of the local microenvironment with a reductionist order approach [201]. The ability to manipulate the *in vitro* microenvironment and to provide physiologically relevant cues is important for the development of the mechanobiology field as cells are known to sense their local environment, leading to changes in gene transcription, morphology (i.e., cell shape, internal cell organization and cell and tissue architecture) and function (i.e., migration, division and differentiation) [202]. In the case of cardiomyocytes, tunable hydrogel devices are promising because they can also recapitulate the native mechanical microenvironment properties [197]. Hydrogels are composed of a polymer network swollen with water, allowing for inclusion of micropatterns of specific cell adhesion ligands [203, 204]. They are highly tunable in terms of their mechanical stiffness, pore size and swelling based on the polymer type, pre-polymer concentration and crosslinking density.

Studies have shown that the substrate stiffness and extracellular matrix components can modulate the cardiomyocyte contractility, cytoskeleton structure, differentiation lineage and adhesion area [171, 174, 205, 206] (reviewed in [50]). Furthermore, protein micropatterning platforms reduce the cell population heterogeneity by constraining the cell shape, which allows for easier cell normalization [207]. Assessing the functional contractility of CMs is important for understanding the relationship between cell structure and function. These hydrogel platforms allow for fiducial microbeads to be embedded into the platform, enabling

functional contractility measurements, such as traction force microscopy [15, 208, 209]. Other methods for assessing changes in the active forces that CMs generate have been reviewed in [210].

Native CM cytoskeleton structure, anisotropic contraction direction, and contractility have been recapitulated by manipulating the microenvironment. One study found that neonatal rat ventricular myocytes cultured on rectangular extracellular matrix (ECM) patterns of various aspect ratios aligned their sarcomeres in predictable and repeatable patterns, which is in contrast to circular myocytes [30]. hiPSC-CMs with 7:1 aspect ratio (length by width) protein patterns had increased myofibril alignment and contractile force output when compared to smaller pattern aspect ratios (3:1, 1:1 and non-patterned) [15]. The protein micropatterning platforms can yield cells that adhere in known spacing intervals, which is ideal for image acquisition and can be aligned with high throughput screens [211-214].

Many methods to yield protein-micropatterned hydrogels exist [203]; however, these methods often require cleanroom facilities and microfabrication expertise. Additionally, current technology is often made serially which results in a slow fabrication workflow. Lastly, the challenge of obtaining reproducible and high-quality protein patterns remains [215]. To study cell–ECM and cell–cell protein interactions and spatially confine cells, cell culture substrates may be functionalized with proteins of interest using micropatterning techniques. Microcontact printing (μCP) is a commonly used technique for protein micropatterning on both soft and rigid substrates. The technique utilizes a flexible microfabricated stamp that is inked with

a protein and put in contact with a cell culture platform to transfer the protein pattern.

Many groups have used μCP because the protocols are straightforward and widely accessible; however, the technique is limited by the resulting pattern accuracy and resolution [29]. To increase throughput, it is possible to generate protein patterns over large areas on glass by selectively oxidizing biopassive poly(l-lysine)-grant-poly(ethylene glycol) (PLL-g-PEG) copolymers and backfilling exposed regions with a protein [29, 211, 216, 217]; however, most methods involving PLL-g-PEG require microfabrication equipment that is not commonly available in many laboratories. We have recently established a photoresist lift-off patterning method that is more reproducible than μCP [29]. This method has created higher fidelity patterns and allowed for storage of the photoresist protein templates; however, the method relies on a serial process, and hence it is time-consuming to generate many individual microscopy coverslips and requires working in specialized microfabrication facilities.

Here, we present a batch wafer-scale approach for the photoresist lift-off patterning method that (1) generates a high-yield of glass chips (16 chips per 4” wafer) for (2) protein patterns with high reproducibility and accuracy with (3) long shelf stability. This batch method results in photoresist protein templates on glass chips that can be used to either make protein-patterned hydrogels or protein patterns directly on the chips. We scaled up the photolithography processing step, since this part of the lift-off protocol was one of the main bottlenecks and still allows for a high degree of flexibility in the design and subsequent fabrication of protein-

patterned hydrogels, for example, tuning the mechanical properties of hydrogels (e.g., stiffness), and the selection of extracellular matrix proteins occurs at a later stage in the protocol [34]. In addition, the original photolithography step was the most time-intensive part of fabrication since each template was created serially.

Importantly, our wafer-scale method can be used to generate a large quantity of pattern templates that can be used for more than six months after wafer fabrication and dicing. The shelf stability of the photoresist-patterned glass chips makes it possible to externally source the pattern templates and thus removes the requirement from labs to have cleanroom infrastructure and expertise. The remaining steps in the fabrication of hydrogels do not require specialized equipment besides a chemical fume hood. Further, we have integrated spacers into the hydrogel fabrication method for precise and uniform control of the final hydrogel thickness, which is an important parameter for high-resolution microscopy. Here, we demonstrate the transfer of protein patterns onto hydrogels for a wide range of cell culture substrates, ranging from multi-well cell culture plates to coverslips. Finally, we characterize the performance of Matrigel-patterned hydrogels by demonstrating how single-cell hiPSC-CMs adhere, spread to a high aspect ratio (above 3:1) and actively contract on the hydrogels.

3.3. Materials and Methods

The final hydrogels used for cell-seeding and imaging were protein-patterned hydro- gels with a stiffness of 10 kPa, adhered to a cell culture substrate, in our case, a glass-bottom 6-well plate. The protein patterns inform protein interactions

for the cells within a defined space; we designed the patterns to study single hiPSC-derived cardiomyocytes. The protein patterns had an area of 1500 μm^2 with an aspect ratio of 7:1 (length by width), which helps guide the alignment of myofibrils, thus facilitating a more mature cell phenotype. The single-cell patterns were spaced at intervals of 50 μm along the x- and y-axis, filling the entire 5x7 inch mask so as not to require alignment during the dicing process. This section describes the fabrication process of the hydrogels, including the (1) wafer fabrication process on 4” glass wafers using photolithography and dicing to obtain individual chips and (2) the development and (3) transfer of protein patterns to hydrogels using lift-off and copolymerization techniques.

3.3.1. Wafer Fabrication Process and Dicing

To scale up the photolithography process (summarized in Figure 3-1), we selected 4” glass wafers for their similarity in surface properties to the currently used glass microscopy coverslips [29] (e.g., 48382-085, VWR). We chose 500-μm-thick D263 glass wafers (1617, University Wafer, Boston, MA, USA) due to their low cost and robustness. Thinner glass wafers can also be used. We tested 200-μm-thick borosilicate glass wafers (2248, University Wafer); however, they were significantly more delicate to handle and release from the dicing tape.

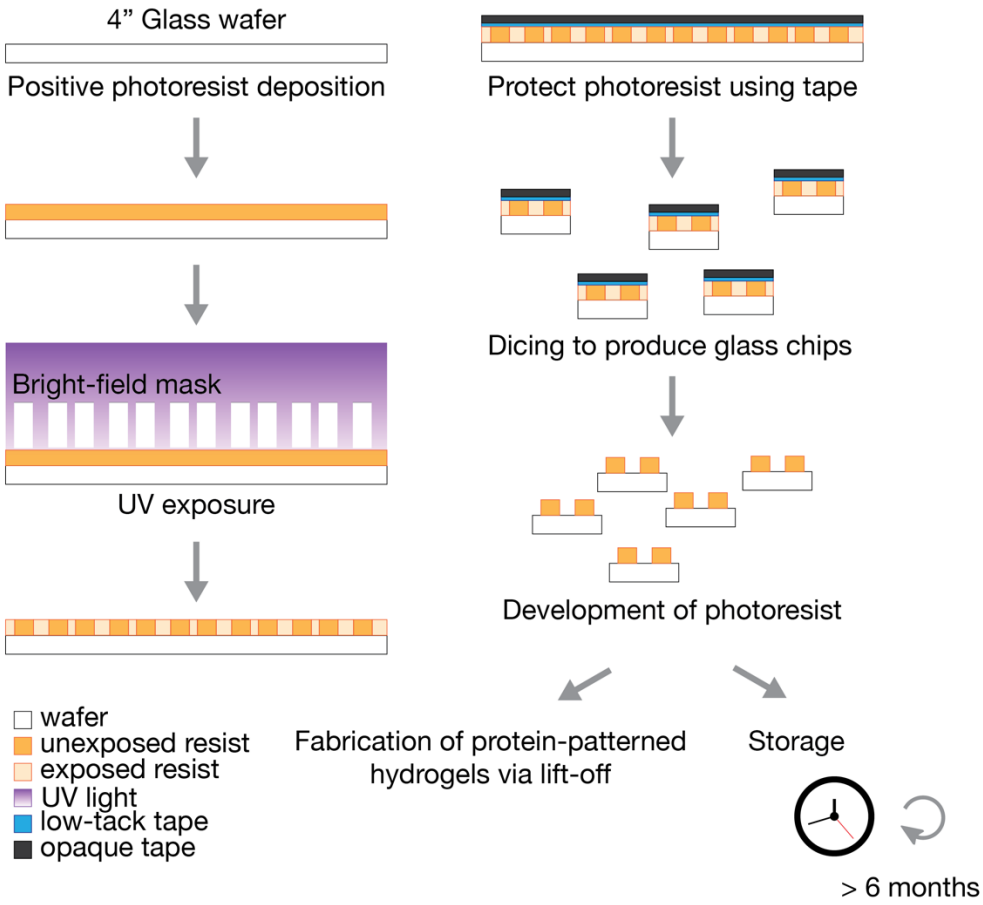

Figure 3-1. Wafer fabrication of 4” glass wafers using photolithography, from photoresist deposition to dicing to obtain individual glass chips, and development of the photoresist. Developed glass chips can be stored for at least six months in a light-protected environment prior to the fabrication of protein-patterned hydrogels.

The 4” glass wafers were thoroughly cleaned with acetone, followed by isopropanol, and then deionized water. Plasma treatment is not recommended as it changes the surface properties of the material, and we observed that this treatment could lead to detachment of the photoresist at the development step. The wafers were dried using a flow of nitrogen gas and then dehydrated on a hotplate for 5 min at 180°C. Positive photoresist AZ1512 (Merck Performance Materials, Merck KGaA,

Darmstadt, Germany) was spun first at 500 rpm for 10 s and then ramped up to 2000 rpm for 45 s in order to achieve a 2-μm-thick resist layer. A soft bake was performed with a level hotplate for 2 min at 100°C. The photoresist was exposed (Karl Suss MA6 aligner, SÜSS MicroTec, Garching, Germany) to achieve 50 mJ/cm^2 at 365 nm using a bright-field mask for transparency (CAD/Art Services, Bandon, OR, USA). The exposure time was based on a daily calibration of the light source using a power meter. For example, when the power meter measured 9 mW/cm^2, the exposure time was adjusted to 5.6 s. For exposure, we used soft or hard contact modes to extend the mask lifetime.

Low-tack surface protection tape (6317A18, McMaster-Carr, Elmhurst, IL, USA) was gently applied on the photoresist-covered wafer, followed by cleanroom masking tape (76505A8, McMaster-Carr) to protect the photoresist from further exposure to light. Excess tape was cut away with a microtome blade. The tape-covered wafers were diced using a dicing saw (ADT 7100, Advanced Dicing Technologies Ltd., Zhengzhou, China) with a thermocarbon diamond blade (2.817-4C-30R-3, Thermocarbon Inc., Casselberry, FL, USA) at a spindle speed of 25,000 rpm, a cut speed of 5 mm/s and a reduced cut water pressure of 0.6 splm to reduce tape delamination. The 4” glass wafer was cut 7×7 times at 0° and 90° angles. The dimensions of each glass chip were 15 mm × 15 mm, yielding more than 16 chips per wafer.

3.3.2. Development

The glass wafer was attached to the dicing fixture with ultraviolet (UV)-release tape. Since the wafer is transparent with photoresist patterns, we did not use UV

light to release the tape. Instead, the chips were carefully peeled away from the tape and the photoresist AZ1512 was developed in AZ 300 MIF (Merck Performance Materials, Merck KGaA, Darmstadt, Germany) for 60 s and rinsed with distilled water. Several chips were developed at the same time using a mini-rack holder (Z688568, Merck KGaA, Darmstadt, Germany). Diced glass chips with a developed photoresist can be stored in a light-protected environment for more than six months prior to lift-off protein patterning and hydrogel fabrication.

3.3.3. Fabrication of Hydrogels with Protein Patterns

The transfer of protein patterns to hydrogels using lift-off is described in detail in [29]. Briefly, glass chips with developed photoresist patterns were incubated with PLL-g-PEG (SuSoS, Dübendorf, Switzerland) for 60 min at 100 µg/mL. The remaining photoresist was lifted off using varying concentrations of N-methyl-2-pyrrolidone (NMP, Merck Performance Materials, Merck KGaA, Darmstadt, Germany) in MilliQ water (Milli-Q, MilliPoreSigma, Merck KGaA, Darmstadt, Germany). The glass chips were first submerged in a mixture of ⅔ MilliQ, ⅓ NMP for 20 s, then pure MilliQ water for 10 s. The glass chips were then submerged and sonicated in pure NMP for 6 min, then submerged and sonicated in a mixture of ½ MilliQ, ½ NMP for 1 min. Finally, the chips were rinsed in fresh MilliQ water for 5 min before we incubated the protein of interest on them. We used fluorescent labeled gelatin (G13186, Thermo Fisher Scientific, Waltham, MA, USA) to visualize the transferred protein patterns on the hydrogels, which we incubated on the glass chips for 60 min at room temperature. For hydrogels that were seeded with hiPSC-CMs, we used Matrigel (356252, Corning, Corning, NY, USA) as the ECM protein at

a concentration of about 1000 µg/mL, which we incubated on the glass chips for 1 h at room temperature.

The polyacrylamide hydrogel was adhered by chemically treating the glass coverslip or glass well plate with bind-silane. Briefly, the bind-silane solution (3 µL bind-silane, 50 µL acetic acid and 950 µL 95% ethanol) was prepared in a chemical fume hood. The bind-silane was purchased from Sigma (3-(trimethoxysilyl) propyl methacrylate (M6514, Merck KGaA, Darmstadt, Germany). Next, the glass was treated with oxygen plasma for 15 s at 80 W or at a high setting. Immediately following plasma, ~50 µL of the bind-silane mixture was added to cover the entire glass substrate. After reacting for 1 min, the excess bind-silane was removed and the remaining solution was allowed to react for 10 min. Finally, the glass substrates were rinsed twice with 1 mL of ethanol, dried with nitrogen gas and allowed to dry in a desiccator until ready for use.

After protein incubation, polyacrylamide (PA) precursor solutions were prepared for casting the hydrogels using a previously published protocol with slight adjustments [35]. Briefly, we prepared 0.5 g/mL acrylamide (01696, Merck KGaA, Darmstadt, Germany) and 0.025 g/mL bis-acrylamide (146072, Merck KGaA, Darmstadt, Germany) solutions in MilliQ water. We combined 198 µL of the acrylamide solution and 40 µL of the bis-acrylamide solution, following the formulation for 10% T and 1% C hydrogels [35]. We added 21.6 µL of red fluorescent microbeads (F8812, Thermo Fisher Scientific, Waltham, MA, USA), a necessary element for traction force microscopy analysis, along with 140.5 µL of 250 mM HEPES buffer (N-2-hydroxyethylpiperazine-N-2-ethane sulfonic acid,

15630080, Thermo Fisher Scientific). We adjusted the volume of MilliQ water to 594.4 µL to account for the added volume of fluorescent microbeads and HEPES buffer. Separately, we prepared a 10% weight/volume solution of ammonium persulfate (APS, A9164, Merck KGaA, Darmstadt, Germany) in MilliQ water. We degassed the PA precursor solutions and the APS solution in a vacuum desiccator for 1 h.

To prepare for casting the hydrogels, 250-µm-thick polydimethylsiloxane (PDMS) spacers were introduced to define hydrogel thickness and make the hydrogel fabrication method compatible with different types of cell culture substrates when using 500 µm diced glass chips. Spacers are not needed when using glass microscopy coverslips due to the difference in weight. Figure 3-2 outlines the process for fabricating protein-patterned hydrogels with diced glass chips and microscopy coverslips. For diced glass chips, PDMS spacers were placed in the well of a glass-bottom 6-well plate (P06-1.5H-N, Cellvis, Mountainview, CA, USA). The patterned glass chip was then placed on top of the PDMS spacers, with the patterned side of the glass facing downward. As the hydrogel polymerizes, the ECM protein pattern is transferred and anchored to the hydrogel via the copolymerization physisorption method [28, 208].

To begin polymerization, 5 µL of the 10% APS solution and 0.5 µL of N,N,N′,N′-tetramethylethylenediamine (TEMED, 411019, Merck KGaA) were added to the precursor solution. The solution was carefully mixed with a pipette, ensuring air bubbles were not introduced to the solution. For the diced glass chips, the solution was pipetted between the PDMS spacers until the solution spread throughout the

entire sandwich, approximately 60 µL of solution total. For microscopy coverslips, 50 µL of the hydrogel solution was pipetted onto the cell culture substrate, then the coverslip was placed on top of the hydrogel solution, patterned side down. Following casting, the hydrogels were protected from light and left for 30 min to begin polymerization. After 30 min, the hydrogels were hydrated with phosphate buffered saline (PBS, 10010049, Thermo Fisher Scientific) and left to polymerize further at 4°C for 6–8 h. After full polymerization, the diced glass chips and microscopy coverslips were removed from the hydrogels and discarded.

It is important to note that hydrogels are not shelf stable [35] and should be stored in a buffer solution. We recommend that cells are seeded on hydrogels within 72 h of full polymerization.

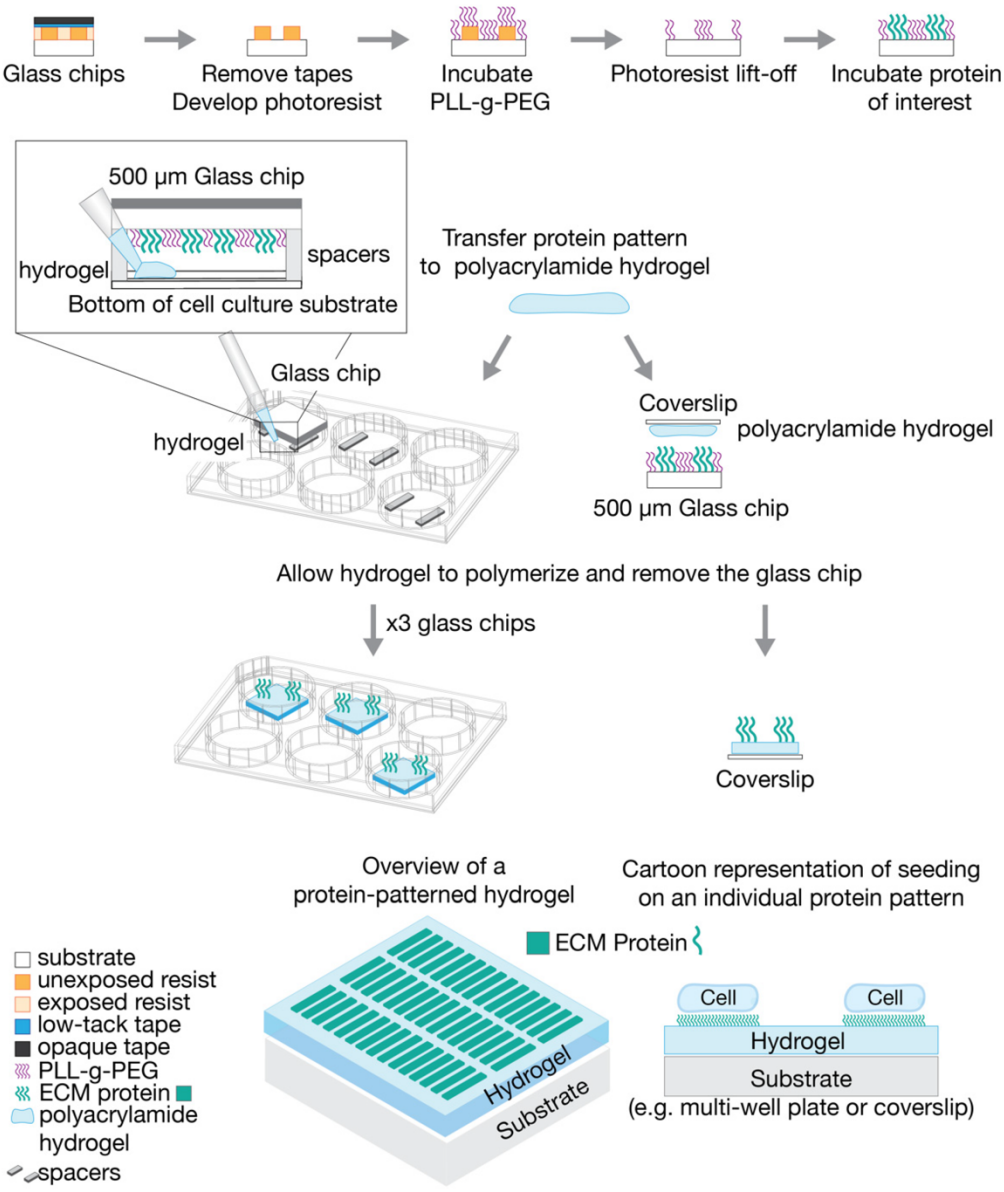

Figure 3-2. Protocol for generating protein patterns on diced glass chips from photoresist templates by lift-off and subsequent fabrication of protein-patterned hydrogels with protein patterns by transfer method.

3.3.4. Maintenance of Induced Pluripotent Stem Cells and hiPSC-Derived Cardiomyocytes

Human-induced pluripotent stem cells (hiPSCs), with GFP-labeled alpha actinin, were purchased from Coriell Institute (AICS-0075-085, Camden, NJ, USA). hiPSCs

were propagated on tissue culture plates coated with Matrigel (356252, Corning) using feeder-free culture conditions in standard culturing environments consisting of 5% carbon dioxide at 37°C. The Essential 8 Medium (Gibco, Thermo Fisher Scientific, Waltham, MA, USA) was changed daily and cells were passed using EDTA when confluency reached 80%. hiPSCs were differentiated into hiPSC-derived cardiomyocytes (hiPSC-CMs) using previously published methods [218]. Upon the initiation of beating (day 7–8), glucose starvation was utilized to purify hiPSC-CMs from other contaminating cell types. On day 12, we utilized the previously published expansion protocol [219] to propagate a significant number of hiPSC-CMs for the entirety of this study. After two passages of expansion treatment, hiPSC-CMs were lifted using EDTA and cryopreserved using xeno-free cryopreservation media Bambanker (Lymphotec, Tokyo, Japan) at a density of 1 million cells/mL. hiPSC-CMs were cooled at a rate of 1°C per minute using a Nalgene Mr. Frosty in a −80°C freezer for 24 h. The following day hiPSC-CM cryovials were transferred and remained in liquid nitrogen until thawed.

When protein-patterned hydrogels were ready for seeding, hiPSC-CMs were thawed for 2 min in a 37°C water bath and centrifuged at 1000 rpm for 5 min. Subsequently, the cryopreservation medium was removed, the hiPSC-CMs were resuspended in replating media (RPMI supplemented with B27 + Thiazovivin (2 μM) + 10% KnockOut Serum Replacement Media) and then replated on our protein-patterned hydrogels at a final density of 250,000 cells.

3.3.5. Microscopy and Data Analysis

We verified that the hiPSC-CMs were adhered and beating on the Matrigel-patterned hydrogels (Video S1) at 4 days post-seeding. The cells were fixed in 4% paraformaldehyde diluted with PBS (10010049, Thermo Fisher Scientific) for 5 min and then rinsed three times with PBS and stored in PBS at 4°C.

Microscopy images were acquired with a Zeiss Axio Observer 7 inverted microscope and a Photometrics Prime 95b camera. For high magnification images, a 40x objective (Zeiss, Jena, Germany, LD Plan-Neofluar 0.6 NA) was used. Overviews of the entire protein-patterned hydrogels were acquired using Zeiss Zen 2.5 blue microscopy software together with ConTraX [214], which is a software developed in our lab for high-throughput single cell imaging and traction force measurement, for which a 10x objective (Zeiss, Jena, Germany, Plan Apochromat 0.45 NA) was used.

We applied the following morphology selection filter to analyze single hiPSC-CMs that took up an elongated aspect ratio within the ECM micropattern width and area. For the hiPSC-CM morphology data, we included the analysis for cells with a high aspect ratio (above 3:1). We note that it is possible to re-run the ConTraX cell morphology analysis with the same images and apply a different selection criteria if needed. For this reason, Excel File S1 contains the ConTraX data for all identified objects.

We performed further data selection and representation in Matlab 2019b (MathWorks, Natick, MA, USA) using the Statistics and Machine Learning toolbox. Identified objects with an area below 200 μm^2 were discarded as debris. Stringent selection criteria only analyze high aspect ratio cells (between 3:1 and 9:1), and

discard cells growing well outside the defined protein patterns (width > 16 μm) and likely cell doublets (area above 1900 μm^2). Microscopy images were opened in Fiji [220] and illumination was pseudo-corrected when appropriate using the BioVoxxel toolbox [221].

3.4. Results

3.4.1. Wafer Fabrication and Protein Pattern Transfer to Hydrogels

Wafer-scale fabrication of photoresist protein templates is a convenient and facile method for generating multiple glass chips to enable on-demand and consistent fabrication of protein-patterned hydrogels. This method makes it easy to make multiple hydrogels with different properties in terms of the stiffness or choice of extracellular matrix proteins. In addition, the glass chips are compatible with different types of cell culture substrates, from glass microscopy coverslips to multi-well plates. Figure 3-3 illustrates how the photoresist patterns (Figure 3-3A) translate into protein patterns on a hydrogel (Figure 3-3B) using fluorescent labeled gelatin. The diced glass chips with photoresist templates were stored for approximately six months prior to lift-off and protein pattern transfer to a hydrogel.

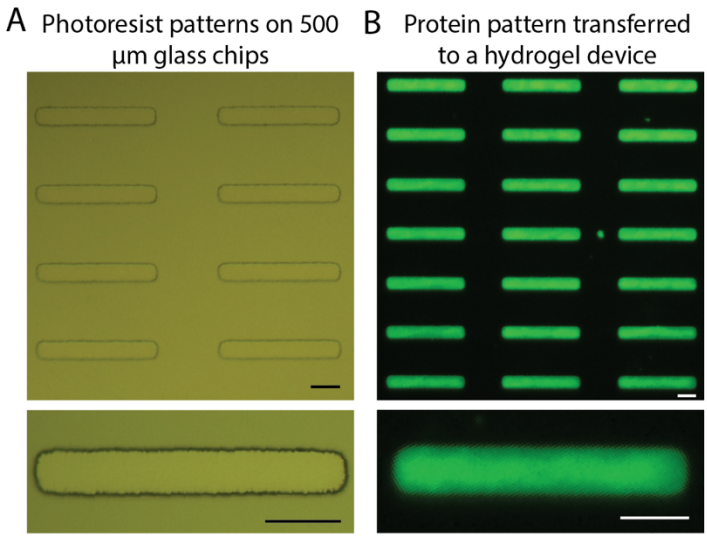

Figure 3-3. Transfer of protein templates in photoresist on glass chips into protein patterns on hydrogels. **(a)** Developed photoresist templates on glass chips. The developed photoresist templates were stored in a light-protected environment for approximately six months prior to hydrogel fabrication. **(b)** Protein patterns on hydrogels were visualized using fluorescent gelatin. Fluorescent gelatin was transferred from glass chips using polydimethylsiloxane (PDMS) spacers to define the hydrogel thickness. Scale bars denote 25 µm.

To obtain high-quality protein patterns on hydrogels, it is important to have photoresist patterns that are clean from debris and contaminations. For this reason, we developed the photoresist post-wafer dicing, but it then becomes critical that the photoresist is minimally exposed to light at all steps of the fabrication process. We used masking tape during dicing to ensure protection from light exposure. This light sensitivity limited our ability to release UV tape on glass wafers using UV exposure and so using thicker glass wafers, namely 500 µm here, significantly increased our yield of glass chips with photoresist patterns; however, thicker glass chips are also heavier than microscopy coverslips and we introduced spacers in the hydrogel fabrication method. The spacers serve three important purposes, where they (1)

prevent the hydrogel from collapsing under the weight of the glass chips, (2) define the hydrogel thickness and (3) ensure even hydrogel thickness for high-resolution microscopy. This was critical to making the method compatible for different types of cell culture substrates when used with 500 μm glass chips and improving imaging capabilities.

The transfer of photoresist templates from glass coverslips to protein-patterned hydrogels has been characterized in [29]. We did not observe differences in quality among the glass chips, which are taken from the center of the wafer and exclude ~10% from the edges. We attributed this to the uniformity of the photoresist due to its thinness and processing (the use of a level hotplate); however, we did observe a decrease in quality of the transferred patterns close to the edges of the diced glass chips.

3.4.2. Single-Cell Cardiomyocytes on Protein-Patterned Hydrogels

Expanded hiPSC-CMs were thawed and cultured for 10 days. The cardiomyocytes were seeded on single-cell Matrigel patterns on hydrogels with an aspect ratio of 7:1 and area of 1500 μm^2. The cells were continuously monitored for their health and adhesion to the hydrogels. We verified that the cardiomyocytes were healthy and beating (Video S1) at 4 days after cell seeding onto the protein-patterned hydrogels. Furthermore, we compared the cell distributions for CMs seeded on protein-patterned hydrogels fabricated with (1) microscopy coverslips in a serial process described in [29] and (2) diced glass chips using the method reported in this paper. For comparison, we used a serial fabrication process [29] with the same single-cell protein templates (described in the Materials and Methods

section) and seeded expanded cardiomyocytes. We found that the cell distribution on protein-patterned hydrogels using both fabrication methods was comparable (illustrated in Figure 3-4A). Protein-patterned hydrogels for these experiments were generated using diced glass chips with photoresist templates fabricated more than six months prior.

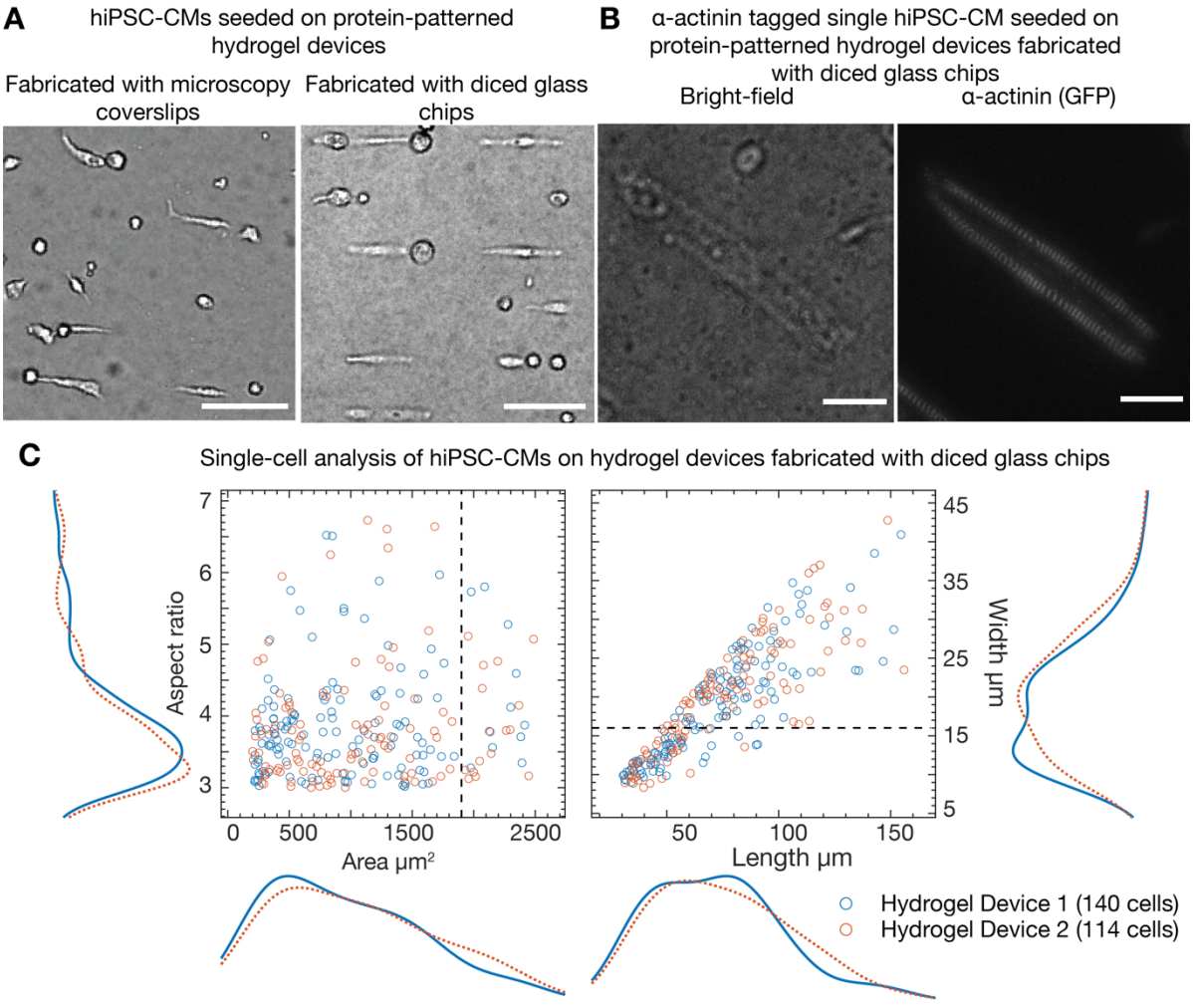

Figure 3-4. Human-induced pluripotent stem cell-derived cardiomyocytes (hiPSC-CMs) seeded on protein-patterned (Matrigel) hydrogels. **(a)** Comparison between cells seeded on hydrogels with protein transferred from microscopy coverslips fabricated in a serial process using the method described in [29] [30] and from diced glass chips fabricated in a batch wafer-scale process as described in this paper. Scale bars denote 100 μm. (B,C) Analysis of cells on protein-patterned

hydrogels fabricated from diced glass chips. **(b)** Microscopy images of an alpha-actinin labeled hiPSC-CM seeded on a hydrogel with protein transferred from a diced glass chip. Scale bars denote 25 μm. **(c)** Two-dimensional scatter plots of the aspect ratio and area and length and width, along with the marginal distributions of the parameters. The results are grouped by hydrogel with debris (objects with area below 200 μm^2) filtered out and high aspect ratio cells selected (between 3:1 and 9:1). The criteria for cells that extend well beyond the protein patterns (width above 16 μm) and likely cell doublets (area above 1900 μm^2) are indicated by the dashed lines. Cells were fixed for the analysis.

Using fluorescently-tagged alpha actinin cells, we have demonstrated the internal structure of high aspect ratio cardiomyocytes on protein-patterned hydrogels (Figure 3-4B). We studied how the cells adhered to the protein patterns by analyzing the distributions of cell area, aspect ratio, length, and width in fixed cells (Excel File S1). We have found that, per hydrogel from a 15 mm x 15 mm glass chip and assuming a usable area of 100 mm^2 due to edge effects, >1000 cells adhere, occupying up to 15% of the total available micropatterns. Of these cells, ~120 cells (10%) adapted to the high aspect ratio (above 3:1) provided by the protein patterns (Figure 3-4C). Seeding at a higher cell density or growing cells on hydrogels for longer are potential strategies to increase the percentage of occupied patterns; however, this comes at the cost of an increased number of cell doublets and cells growing outside of the protein patterns. Already, we could see many cells growing well outside of the protein patterns (width above 16 μm) and likely cell doublets (area above 1900 μm^2); however, even when using this stringent set of criteria, we typically obtained ~50 cells per hydrogel, which is sufficient for most high throughput experiments that would, in addition, use several hydrogels.

3.5. Discussion

In this work, we have presented a batch wafer-scale approach based on photolithography for lift-off protein patterning on polyacrylamide hydrogels that (1) generates a high-yield of glass chips for (2) protein patterns with high reproducibility and accuracy with (3) long shelf-life stability. A previous work has utilized individual small glass microscopy coverslips during the lithography stage [29]. This serial fabrication process ultimately results in a slow fabrication speed. In contrast, our wafer-scale approach creates many photoresist-patterned glass chips in parallel using a single wafer. We streamlined the photolithography part of the process to render the lift-off patterning method more accessible and scalable. Our work could be used as a roadmap to establish future collaboration with a cleanroom expertise team, in which wafer processing, lithography and dicing are common techniques. After the diced glass chips with photoresist patterns are made, the rest of the protocol is straightforward and can be performed with standard laboratory equipment. Furthermore, our work shows that the diced and developed photoresist glass chips can be stored for at least six months. This is significant since it allows for streamlined batch processing and decreases the required cleanroom time. This shelf-stability also allows for flexibility around cell culture maintenance.

Our work shows that lift-off patterning and the copolymerization transfer technique with polyacrylamide hydrogels is compatible with single cell hiPSC-CMs on Matrigel rectangular protein patterns. Previous work using lift-off protein patterning utilized Madin–Darby Canine Kidney (MDCK) cells on collagen I and gelatin protein patterns [29]. Furthermore, while we have only presented results with

the polyacrylamide hydrogel formulation for 10 kPa here, previous work has also shown that lift-off is compatible with various hydrogel stiffness (e.g., 5, 10 and 25 kPa). Hence, our approach retains the previously demonstrated possibilities to work with varying cell types, single cell or multiple cells, ECM protein types, protein pattern geometries, and hydrogel stiffness. Additionally, since this platform has compatibility for live cell microscopy, other cell functional readouts can be easily added, such as traction force microscopy [15]. Our approach presented here can be used in future studies to increase our understanding of mechanobiology and how the microenvironment influences cell structure and function in both healthy and disease states.

3.6. Supplementary Materials

The following are available online at https://www.mdpi.com/article/10.3390/mi12111386/s1, Video S1: recording of a single hiPSC-CM beating on a protein-patterned hydrogel; real time, Excel File S1: Area, aspect ratio, length, and width data of fixed single hiPSC-CMs adhered to protein-patterned (Matrigel) hydrogels. Hydrogels were scanned in entirety to obtain this data.

4. Mimicking CM-CM and CM-ECM Interactions with Dual-Protein Patterning

4.1. Background and Motivation

Patterning single CMs on rectangular extracellular matrix (ECM) proteins to replicate CM-ECM interactions has been commonly used to improve CM structure and function [15, 30, 31] (see Chapter 1 for more discussion). However, few studies have investigated CM-CM interactions, and the few that have had used rodent models, limiting their translatability to the human heart [18, 49]. In this work, we sought to bridge this gap, investigating the effects of N-cadherin, a protein associated with CM-CM interactions, on hiPSC-CM structure and function.

In early patterning experiments, Bray, et al. patterned rat neonatal ventricle myocytes on glass substrates with circular and rectangular fibronectin patterns, with the rectangular patterns having aspect ratios of 1:1 to 1:7 [30]. They found that the geometric cues from rectangular patterns, like corners, lead to distinct sarcomere alignment patterns, with higher aspect ratio rectangles leading to greater sarcomere organization and contractility [30]. This influenced further investigation into patterning of CMs, especially for hiPSC-CMs, which present a more immature phenotype when unpatterned [15]. Ribeiro, et al. patterned single hiPSC-CMs on PA hydrogels patterned with Matrigel, using rectangles with aspect ratios from 1:1 to 7:1 and found that with increasing pattern aspect ratio, hiPSC-CMs had increased sarcomere alignment, greater force production, and more anisotropic calcium transients, all metrics associated with improved sarcomere contractility [15]. This further solidified the use of protein patterning to improve the structure and

function of hiPSC-CMs, and studies have used the patterned hiPSC-CM model to investigate disease mutations in hiPSC-CM lines [31]. For example, Wang, et al. demonstrated the use of the single-cell hiPSC-CM model by studying 7:1 fibronectin-patterned hiPSC-CMs that had been genetically edited to include mutations with Barth syndrome. They found that the mutations interfered with sarcomere formation, leading to less organized myofibrils and weaker contraction [31]. These studies demonstrate the value of protein patterning for hiPSC-CM studies, but do not investigate the role of CM-CM interactions in addition to the CM-ECM interactions.

While there remains a gap in studies patterning hiPSC-CMs with N-cadherin, there have been a few studies that have cultured rat CMs on N-cadherin-coated polyacrylamide (PA) hydrogels [18] and N-cadherin-patterned glass [49]. Chopra, et al. cultured single-cell rat CMs on N-cadherin-coated hydrogels and found that the CMs produced traction force with a similar magnitude as single-cell rat CMs on ECM proteins but that N-cadherin-mediated mechanotransduction is distinct from ECM-mediated mechanotransduction [18]. In another study, Chopra and colleagues patterned single-cell rat CMs on N-cadherin patterns on glass to learn that alpha-catenin serves as an adapter protein for N-cadherin-mediated mechanotransduction [49]. While these studies have provided useful insight into the role of N-cadherin in CM mechanotransduction, their translatability is limited because they are in rat CMs, which have key physiological differences compared to human CMs [4, 5].

Beyond culturing CMs on N-cadherin, previous studies have investigated the role of N-cadherin and CM-CM junctions in the organization and functioning of the

subcellular contractile machinery in rat, mouse, cat, and chick CMs [19, 222-225]. In an *in vitro* study, Goncharova, et al. found that blocking N-cadherin inhibits the development and organization of sarcomeres in single-cell rat and chick CMs cultured on glass [222]. Simpson and colleagues showed that cell-cell contacts are necessary for *in vitro* feline CMs cultured on laminin-coated petri dishes to stabilize myofibrils and to beat on their own [223]. In an *in vitro* study of mouse myocytes, Luo, et al. found that an N-cadherin knockout restricted the ability of the myocytes to align their myofibrils with neighboring myocytes, leading to decreased contractility [19]. In an *in vivo* whole animal study, Wu and colleagues showed that N-cadherin and integrin-mediated stabilization of myofibrils occur independently during development [224]. Kostetskii and colleagues found *in vivo* N-cadherin knockout mice had shorter sarcomere lengths and arrhythmias, which they attributed to the lack of N-cadherin at the plasma membrane to anchor myofibrils [225].

These previous *in vivo* and *in vitro* studies demonstrate the importance of N-cadherin in CM subcellular structure, function, and development [18, 19, 49, 222-225]. One of the biggest advantages of the hiPSC-CM model is the ability to investigate dynamic subcellular structures in live cells [6, 15, 16], and one of the main disadvantages is the immature phenotype, similar to that of fetal CMs [22, 23]. With this in mind, we sought to investigate the effects of N-cadherin patterning on hiPSC-CM sarcomere structure and function, with the hypothesis that N-cadherin patterning would improve markers of hiPSC-CM maturity.

4.2. Single hiPSC-CMs on N-cadherin and Matrigel Patterns on PA Hydrogels

The first studies we conducted to investigate the interactions between neighboring CMs consisted of patterning hiPSC-CMs on single protein N-cadherin islands.

4.2.1. Methods

4.2.1.1. Cell Culture and Differentiation

For this work, we used GFP-tagged alpha-actinin hiPSC-CMs. The hiPSCs were alpha-actinin-2 (cell line 75) developed at the Allen Institute for Cell Science (allencell.org/cell-catalog) and available through Coriell (AICS-0075-085) [16, 20].

hiPSCs were cultured on tissue culture plastic coated in Matrigel (Corning, 356252) using feeder-free culture conditions in standard conditions of 5% carbon dioxide at 37°C. hiPSCs were cultured in Essential 8 Medium (Gibco, ThermoFisher, A1517001) which was changed daily. Cells were passed with EDTA when confluency reached 75%. hiPSCs were differentiated into cardiomyocytes (hiPSC-CMs) using a previously published protocol [218]. Briefly, once the hiPSC-CMs reached 75% confluency (day 0), the media was changed to RPMI/B27 without insulin media (B27-INS - ThermoFisher, RPMI - 11875119, B27 without insulin - A1895601) with 6μM CHIR-99021 (SelleckChem, S2924), a GSK3-β inhibitor. After 48 hours (day 2), the media was changed to B27-INS. After 24 hours (day 3), the media was changed to B27-INS with 2μM Wnt-C59 (SelleckChem, S7037), a Wnt inhibitor. After 48 hours (day 5), the media was changed to B27-INS. From day 7 onward, the media was changed to fresh RPMI/B27 (B27; ThermoFisher, RPMI - 11875119, B27 - 17504044) every two days. After the onset of beating, around day

10, the hiPSC-CMs were purified using glucose starvation [218]. After purification, the media was changed to fresh B27 every two days until they were seeded on devices.

4.2.1.2. Protein Patterning

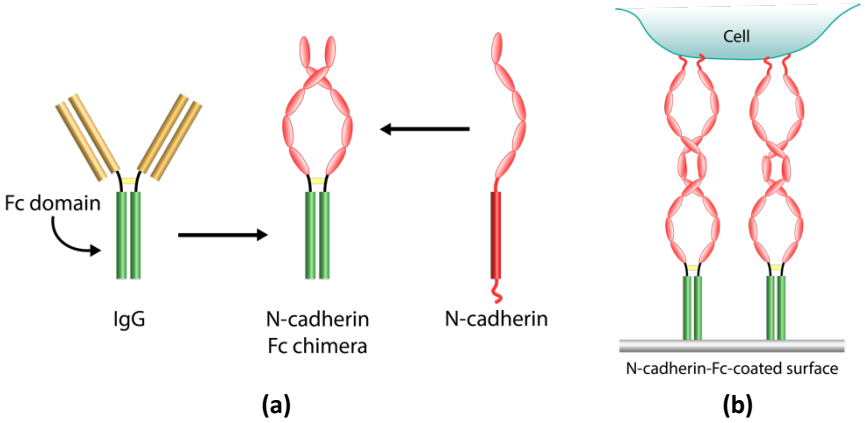

Figure 4-1. (a) Structure of an N-cadherin Fc chimera. (b) Schematic of N-cadherin Fc chimera-functionalized surface attaching a cell. Adapted from Nag, et al. [226] (CC by 3.0: http://creativecommons.org/licenses/by/3.0).

To functionalize devices with N-cadherin, we used an N-cadherin Fc chimera (R&D Systems, 1388-NC-050) and a linking protein, Protein A (Sigma, 1578805). The Protein A attaches to the Fc region of the N-cadherin chimera protein, ensuring the extracellular binding domain of the N-cadherin protein is presented at the surface of the hydrogel (Figure 4-1).

Protein patterning was achieved using a previously published protocol [29]. Briefly, glass coverslips were patterned with AZ1512 photoresist using photolithography (Figure 4-2). These coverslips were then incubated with a blocking molecule, poly(L-lysine)-g-poly(ethylene glycol) (PLL-g-PEG, SuSoS), at a concentration of 100 µg/mL. Then, the photoresist patterns were removed with N-

methyl-2-pyrrolidone (EMD Performance Materials), leaving behind Pll-g-PEG in the inverse pattern on the coverslip. After removing the photoresist, either Protein A or Matrigel was incubated for 4 hours at 4°C. Protein A was at a concentration of 100µg/mL, diluted in phosphate buffered saline (PBS; Gibco, ThermoFisher, 10010023), and Matrigel was diluted 1:10 from the stock concentration in Dulbecco's Modified Eagle Medium/Nutrient Mixture F-12 (DMEM, ThermoFisher, 11330057).

For studies on glass, the Matrigel-patterned coverslips were washed and stored in PBS until seeding. The Protein A-patterned coverslips were incubated with N-cadherin at a concentration of 100µg/mL for 3 hours at 4°C. After the N-cadherin incubation, the N-cadherin coverslips were washed and stored in PBS until seeding.

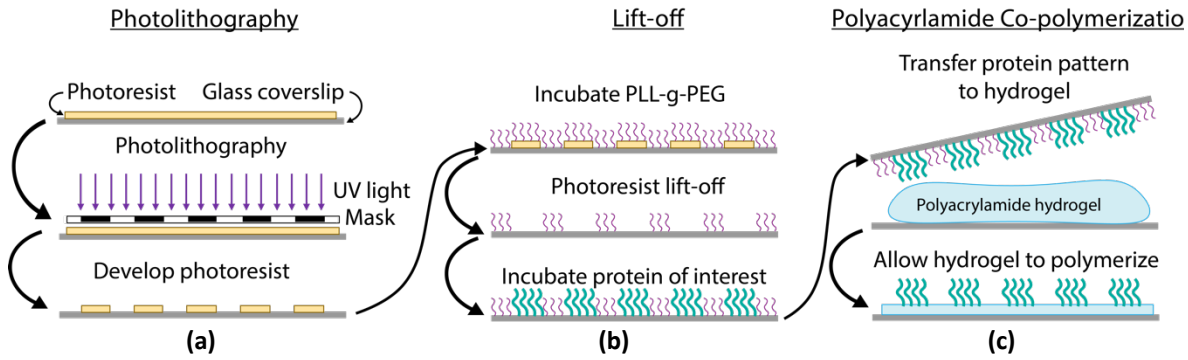

Figure 4-2. Process flow for creating protein-patterned PA hydrogels**: (a)** photolithography, **(b)** liftoff, **(c)** and PA polymerization and protein transfer. Adapted from Moeller, et al. [29] (CC0 1.0: https://creativecommons.org/publicdomain/zero/1.0/).

4.2.1.3. Polyacrylamide Hydrogel Fabrication

To prepare the PA hydrogels, we followed a previously published protocol [35]. We treated glass bottom dishes (#1.5, Cellvis) with 3-(trimethoxysilyl)propyl methacrylate (bind-silane, Sigma) to secure the bottom of the PA hydrogel to the

glass dish. Briefly, we prepared a solution with 950μL of 100% ethanol, 50μL of acetic acid, and 3μL of 3-(Trimethoxysilyl)propyl methacrylate (bind-silane; Sigma, M6514). Then, we treated the glass with oxygen plasma for 30 seconds at 18W (Harrick, PDC-32G). Directly after plasma treating the glass, we added ~50μL of the bind-silane solution to the glass surface. The solution was incubated on the glass for 1 minute, after which the excess bind-silane solution was removed. The remaining solution was left to react for 10 minutes, after which the glass was rinsed twice with 1mL of 100% ethanol and dried with compressed nitrogen.

We followed a previously published recipe [35] to prepare PA hydrogels with a stiffness of ~10kPa. We combined 40μL of a 0.025g/mL N,N'-Methylenebis(acrylamide) (bis-acrylamide; Sigma, 146072) solution, 198μL of a 0.5g/mL acrylamide (Sigma, 01696) solution, 594.4μL of water, 140.5μL of 250mM N-2-hydroxyethylpiperazine-N-2-ethane sulfonic acid (HEPES; Thermo, 15630080), and 21.6μL of red fluorescent microbeads (diameter 0.5μm, Thermo, F8812). Separately, we prepared a 10% weight by volume (w/v) solution of ammonium persulfate (APS; Sigma, A9164) in MilliQ water. We degassed the PA precursor solution and the APS solution for 1 hour in a vacuum desiccator to remove bubbles.

To begin polymerization, we added 0.5μL of N,N,N',N'-tetramethylethylenediamine (TEMED; Sigma, 411019) and 5μL of the 10% w/v APS solution to the PA precursor solution. The solution was mixed gently with a P1000 pipette and 50μL of the solution was pipetted onto the bind-silane-treated glass surface. The protein patterned coverslip was then placed on top of the solution, sandwiching the PA solution between the bind-silane-treated glass and the protein

patterned glass. After casting, the hydrogels polymerized in the dark for 30 minutes before being hydrated with PBS and left to fully polymerize at 4°C for 6-8 hours. After full polymerization, the protein patterned top coverslip was removed and discarded and the hydrogels were washed three times with PBS.

Then, we removed the top coverslip and washed the hydrogels three times with PBS. I stored the Matrigel hydrogels at 4°C until cell seeding. We incubated the Protein A hydrogels with N-cadherin at a concentration of 100µg/mL for 3 hours at 4°C. After N-cadherin incubation, all devices were seeded with hiPSC-CMs at the same time. N-cadherin patterns were verified with anti-rabbit-pan-cadherin antibody (Sigma) and AlexaFluor 488 polyclonal antibody (AF488, ThermoFisher).

The Matrigel-patterned hydrogels were stored in PBS at 4°C until seeding. The Protein A-patterned hydrogels were incubated with N-cadherin at a concentration of 100µg/mL for 3 hours at 4°C. After the N-cadherin incubation, the N-cadherin hydrogels were washed three times and stored in PBS until seeding. N-cadherin patterns were verified with anti-rabbit pan-cadherin primary antibody (Sigma, C3678) and AlexaFluor 488 anti-rabbit secondary antibody (ThermoFisher, A-11034).

4.2.1.4. Oxidized HEA Functionalized Polyacrylamide Hydrogel Fabrication

The oxidized N-Hydroxyethyl acrylamide (HEA; Sigma, 697931) PA hydrogels were prepared following a previously published protocol with some modifications [33]. Briefly, we began by oxidizing HEA by adding 0.01g of sodium metaperiodate

(Sigma, 71859) to 2.338mL of HEA, then incubating in the dark on a shaker for 4 hours.

To prepare the PA hydrogel solution, we combined 732µL of 40% Acrylamide solution (Bio-Rad, 1610140) and 260µL of 2% Bis-acrylamide solution (Bio-Rad, 1610142) with 4.008mL MilliQ water. Finally, we added 200µL of oxidized HEA, bringing the total volume to 5.2mL. Separately, we prepared a 10% weight by volume (w/v) solution of APS in MilliQ water.

To begin polymerization, we added 2.6µL of TEMED and 260µL of the 10% w/v APS solution to the PA solution. The solution was mixed gently with a P1000 pipette and then 50µL of the solution was pipetted onto the bind-silane-treated glass surface. The protein patterned coverslip was then placed on top of the solution, sandwiching the PA solution between the bind-silane-treated glass and the protein patterned glass. After casting, the hydrogels polymerized in the dark for 30 minutes before being hydrated with PBS and left to fully polymerize at 4°C for 6-8 hours. After full polymerization, the protein patterned top coverslip was removed and discarded.

Following the removal of the top coverslip, the PA hydrogels were incubated with N-cadherin. The PBS was aspirated from the dish and ~50µL of 100µg/mL N-cadherin solution was added to the hydrogel surface and left to incubate for 3 hours at 4°C. After 3 hours, the PA hydrogels were washed three times with 1mL PBS and then stored at 4°C in PBS until cell seeding.

4.2.1.5. Cell Seeding

Cells were seeded on devices at a density of ~100,000 cells/cm^2 between day 25-30 and imaged 3-4 days after seeding (day 30-35). To begin seeding, we prepared replating media, consisting of 60% B27, 40% Knock Out Serum Replacement (KOSR; ThermoFisher, 10828028), and 0.014% Thiazovivin (Sigma, SML1045-25MG). We lifted up the hiPSC-CMs using TrypLE 10X (ThermoFisher, A1217702) for 5-10 minutes at 37°C. After 5-10 minutes, we diluted the TrypLE 10X by adding 1mL of replating media. The solution was triturated to further lift up the cells and then collected in a 15mL conical tube containing 3mL of replating media to further dilute the TrypLE 10X. The 15mL conical tube was spun in a centrifuge at 200g for 3 to 5 minutes, until a pellet formed at the bottom of the tube. The supernatant was aspirated and the pellet was resuspended with 1mL of replating media. We stained a sample of the resuspended cells with Trypan Blue (ThermoFisher) and counted cells on a hemocytometer to achieve the desired density of 10,000 cells per device. Then, we flooded the devices with the resuspended cell solution and left them in the incubator at 37ºC for 48 hours. After 48 hours, we changed the media in the devices to B27 with 1% Penicillin-Streptomycin (Pen-Strep; ThermoFisher, 15140122) every two days. We imaged the hiPSC-CMs on devices 3-5 days after seeding.

4.2.1.6. Microscopy

All data were imaged on one of two microscope setups: i) a Zeiss Axio Observer 7 inverted microscope with high speed camera (Photometrics Prime 95b) and 5X (NA = 0.16, Zeiss) and 10X (NA = 0.45, Zeiss) air objectives and ii) a Leica

DMI6000B inverted microscope with high resolution camera (pco.panda 4.2) and 10X air objective (NA = 0.3, Leica).

4.2.2. Results

4.2.2.1. N-cadherin Was Successfully Patterned on Glass and PA Hydrogel Substrates

To study the effect of CM-CM interactions on hiPSC-CM maturity, we aimed to isolate cell-cell contacts from cell-ECM contacts. To do this, we patterned N-cadherin in rectangles with an aspect ratio of ~7:1 – with a width of ~15μm and length of ~100μm. Adult human ventricular CMs have aspect ratios ranging from 5:1 to 7:1 and previous studies found that hiPSC-CMs patterned in an aspect ratio of 7:1 had greater sarcomere alignment, force production, and other markers of maturity [15, 30, 31].

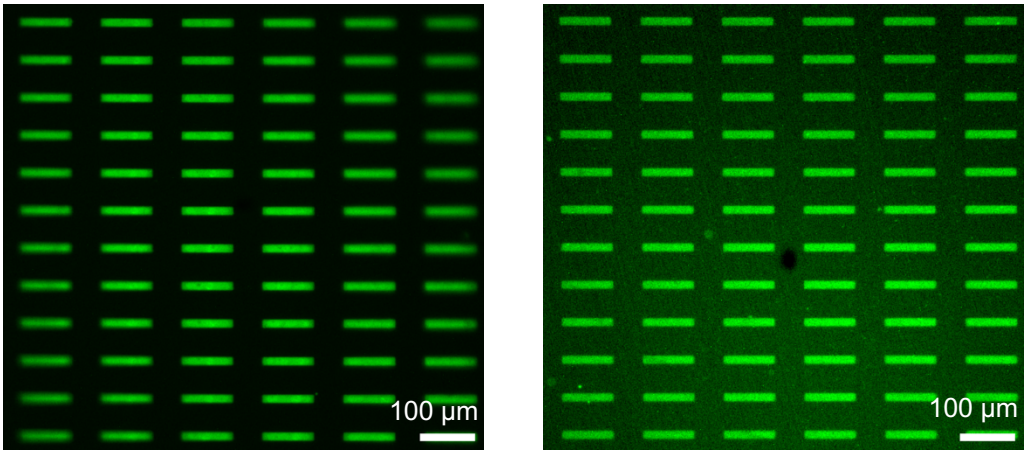

Figure 4-3. N-cadherin patterns on glass and PA hydrogel. Fluorescence images of lift-off-patterned N-cadherin on **(a)** glass and **(b)** hydrogel devices, visualized with pan-cadherin primary antibody and AlexaFluor 488 secondary antibody.

To verify the N-cadherin patterning, we stained unseeded devices with a pan-cadherin antibody (Figure 4-4a). To further confirm the presence of N-cadherin, we tested the specificity of the antibodies. To demonstrate the pan-cadherin antibody did not bind non-specifically to the substrate, we stained a device without any protein. We performed lift-off patterning on a coverslip but did not backfill with any protein and then stained the coverslip with the pan-cadherin antibody and the AlexaFluor 488 secondary antibody (Figure 4-4b). To show that the AlexaFluor 488 antibody was not binding non-specifically to the substrate, we repeated the same lift-off patterning without backfilling with a protein, and then stained with just the AlexaFluor 488 secondary antibody (Figure 4-4c). To check that the pan-cadherin antibody did not bind non-specifically to other proteins, we backfilled lift-off-patterned coverslips with laminin, an ECM protein, and then stained with pan-cadherin and AlexaFluor 488 (Figure 4-4d). Finally, we stained lift-off-patterned coverslips backfilled with Protein A to determine if the pan-cadherin antibody could bind to the N-cadherin-binding region of Protein A (Figure 4-4e).

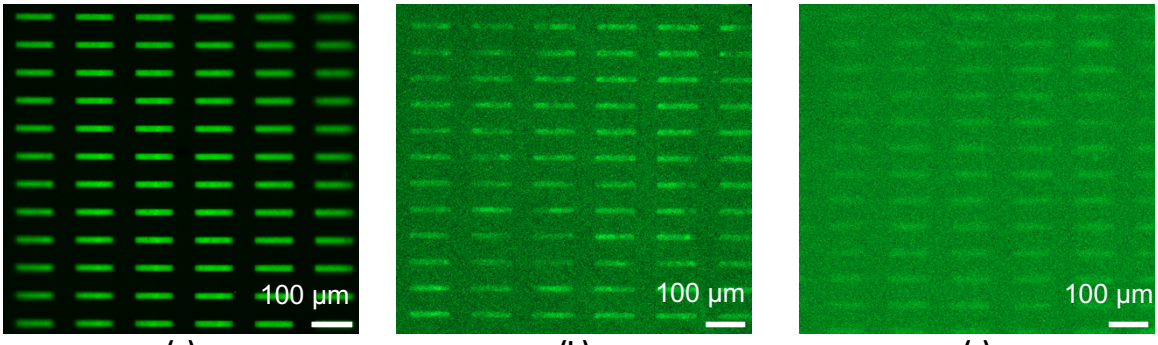

(a) (b) (c)

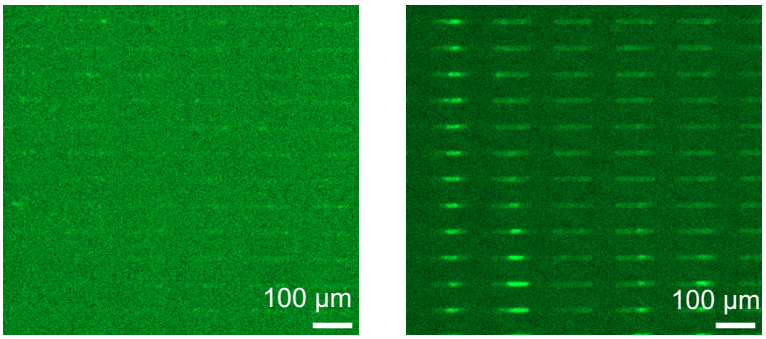

Figure 4-4. N-cadherin signal is not due to a lack of antibody specificity. Fluorescence images of **(a)** N-cadherin protein pattern on glass, and immunostaining controls on glass: **(b)** no protein devices stained with pan-cadherin and AF488 antibodies, **(c)** no protein devices stained with AF488 antibody, **(d)** devices patterned with laminin stained with pan-cadherin and AF488 antibodies, and **(e)** devices patterned with Protein A stained with pan-cadherin and AF488 antibodies.

4.2.2.2. Patterning hiPSC-CMs on N-cadherin-Functionalized Devices

hiPSC-CMs Attach to N-cadherin Patterns on Glass Coverslips

After verifying N-cadherin patterning, we seeded hiPSC-CMs on devices. For each experiment, we used Matrigel-patterned glass and PA hydrogels as our cell-ECM condition and N-cadherin-patterned glass and PA hydrogels as our cell-cell condition. Additionally, the Matrigel devices served as cell-seeding controls, as cells attach robustly to Matrigel [6, 15, 141]. Following seeding, we saw successful hiPSC-CM attachment and patterning on both Matrigel devices (glass and PA hydrogel) and on the N-cadherin glass device (Figure 4-5). No hiPSC-CMs attached to the N-cadherin PA hydrogel device (Figure 4-5).

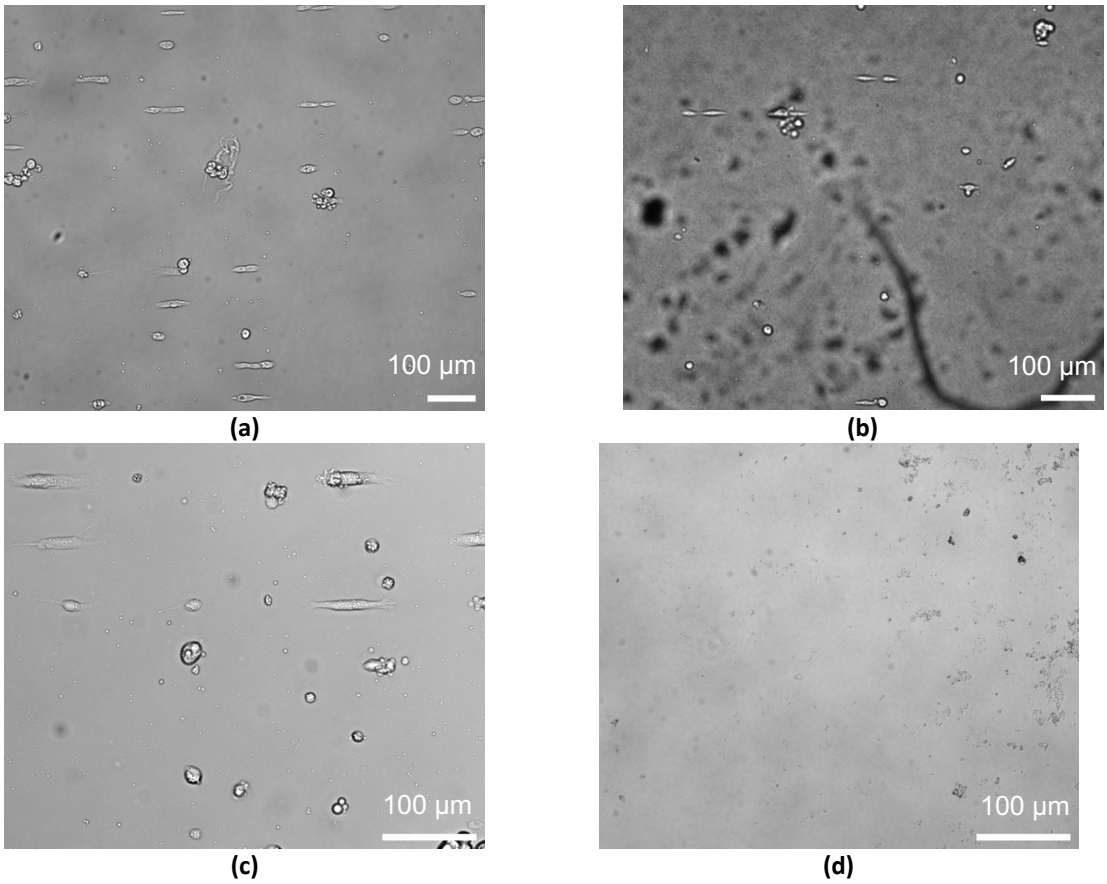

Figure 4-5. hiPSC-CMs attach to Matrigel on glass and PA hydrogel, and N-cadherin on glass, but not N-cadherin on PA hydrogel. Brightfield images of hiPSC-CMs seeded on **(a)** Matrigel patterned on glass, **(b)** Matrigel patterned on PA hydrogel, **(c)** N-cadherin patterned on glass, and **(d)** N-cadherin patterned on PA hydrogel.

hiPSC-CMs Did Not Attach to N-cadherin-Patterned PA Hydrogels

No hiPSC-CMs attached to N-cadherin-patterned PA hydrogels (Figure 4-5d). To examine the impact of patterning on cell attachment to N-cadherin-functionalized PA hydrogels, I made glass and PA hydrogel devices with N-cadherin covering the entire surface. These devices were made following the same protocol as the patterned devices, without the photolithography and lift-off processes.

hiPSC-CMs attached readily to the unpatterned N-cadherin on glass and resumed beating. Because they were not patterned, these hiPSC-CMs

demonstrated a more immature phenotype, specifically in their rounded morphology. Like the patterned N-cadherin, no cells attached to the unpatterned N-cadherin on hydrogel devices (Figure 4-6).

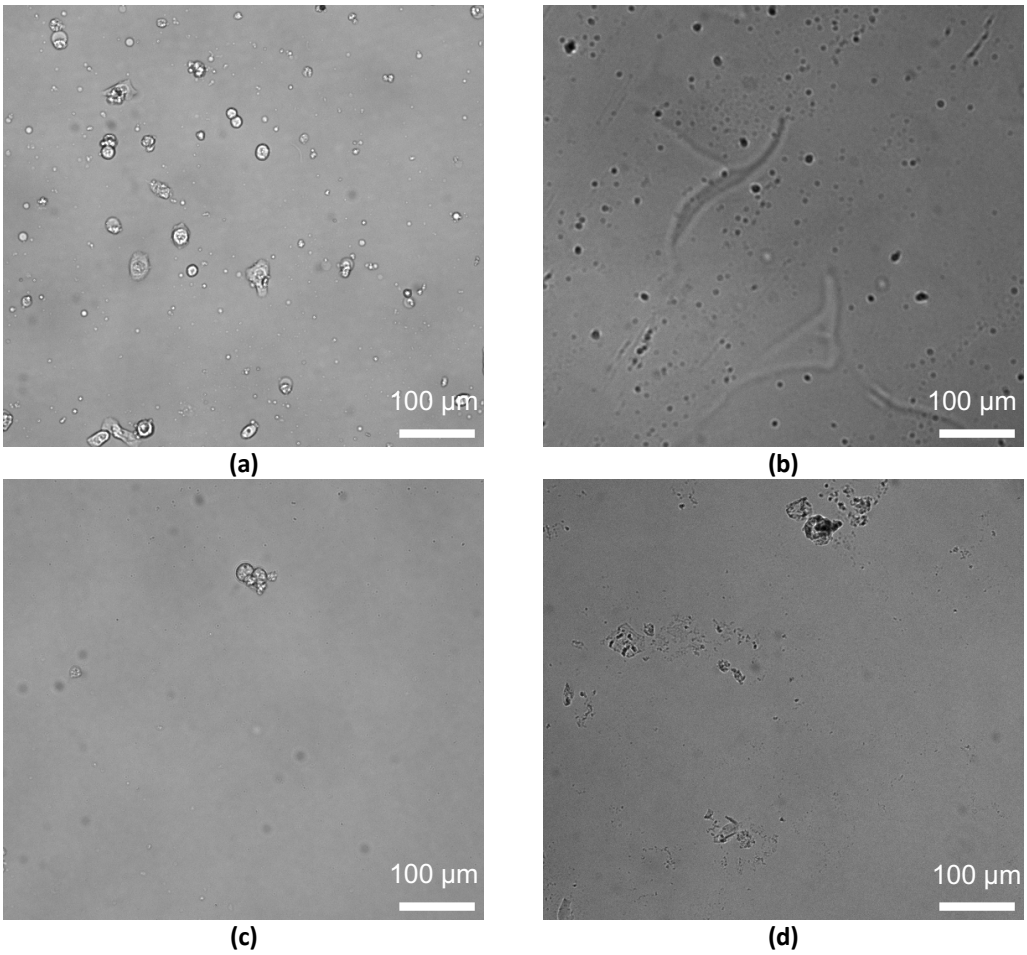

Figure 4-6. Cells attach to unpatterned N-cadherin on glass, but do not bind to unpatterned N-cadherin on PA hydrogel nor non-specifically bind to glass or PA hydrogel without protein functionalization. Brightfield images of hiPSC-CMs seeded on **(a)** unpatterned N-cadherin on glass, **(b)** unpatterned N-cadherin on PA hydrogel, **(c)** glass not functionalized with protein, and **(d)** PA hydrogel not functionalized with protein.

To determine whether cells adhere specifically to N-cadherin or to the glass itself, and to test the non-binding quality of PA hydrogels, I made glass and PA

hydrogel devices without any protein functionalized to their surfaces. The glass devices without protein had some debris adhesion, but no single CM attachment or beating (Figure 4-6c). The PA hydrogel devices without protein had no attachment at all, as expected (Figure 4-6d).

Because hiPSC-CMs attach to N-cadherin on glass, we hypothesized that hiPSC-CMs could not attach to N-cadherin on PA hydrogels because the N-cadherin was not firmly anchored to the PA hydrogel surface. To test this, we stained previously seeded N-cadherin-patterned PA hydrogels with pan-cadherin and AlexaFluor 488 (Figure 4-7), to determine if N-cadherin was still present on the PA hydrogel surface. All N-cadherin patterns had been removed from the hydrogel surface, indicating that N-cadherin is degraded or detached in the process of hiPSC-CM seeding (Figure 4-7).

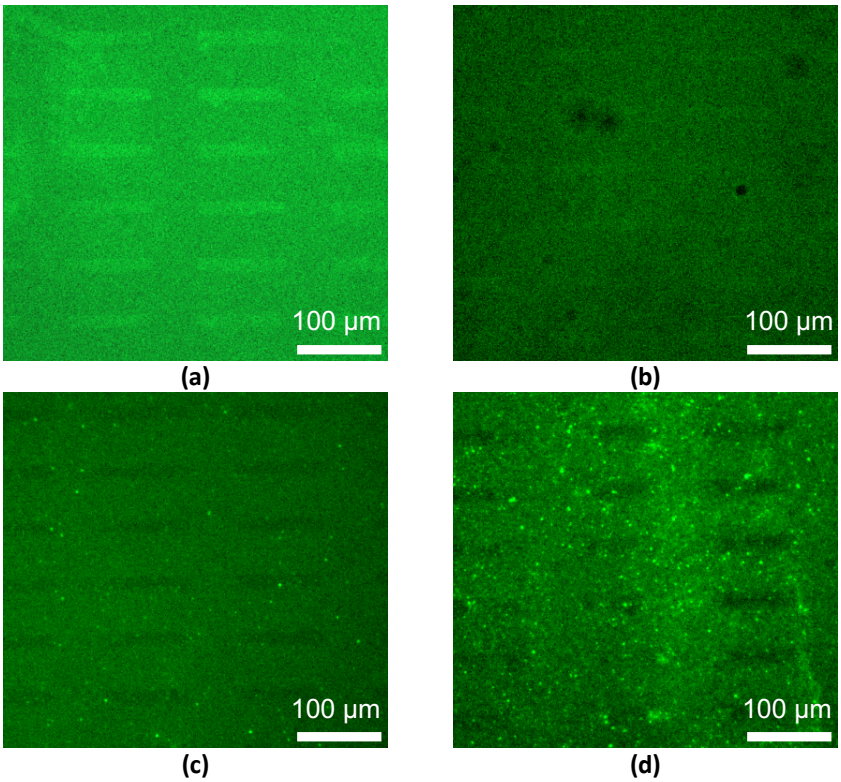

Figure 4-7. N-cadherin is removed from PA hydrogel devices after hiPSC-CMs are seeded and fail to attach. GFP images of N-cadherin-patterned **(a)** glass device 1, **(b)** glass device 2, **(c)** PA hydrogel device 1, and **(d)** PA hydrogel device 2 stained four days after they were made and three days after seeding them with hiPSC-CMs. Patterns were visualized with pan-cadherin primary antibody and AlexaFluor 488 secondary antibody.

To demonstrate that the degradation or removal of N-cadherin is not due to the time elapsed between incubation and staining, we did a time study with N-cadherin-patterned PA hydrogels. We made three N-cadherin-patterned PA hydrogels to stain for N-cadherin patterns at different time points after being cultured in media. The first PA hydrogel was stained and imaged the day of seeding (Figure 4-8a), the second two days after seeding (Figure 4-8b), and the third three days after seeding (Figure 4-8c). With the unseeded devices, there was slight degradation of the N-cadherin pattern with time, but overall the pattern was preserved, indicating that media and/or time would not result in the N-cadherin removal seen in Figure 4-7.

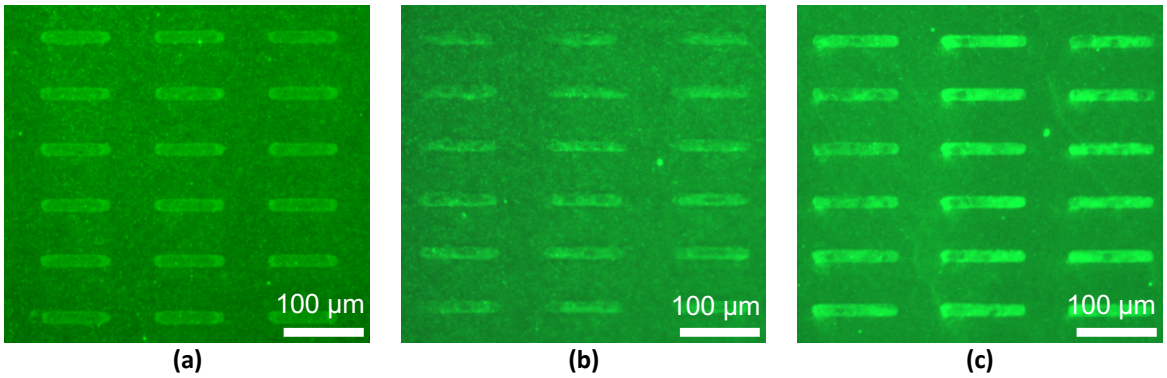

Figure 4-8. N-cadherin patterns do not degrade over time when cultured in hiPSC-CM media. GFP images of N-cadherin patterned on PA hydrogel devices immunostained **(a)** the day after the devices were made, **(b)** three days after the devices were made, and **(c)** four days after the devices were made. Patterns were visualized with pan-cadherin primary antibody and AF488 secondary antibody.

4.2.2.3. Patterning hiPSC-CMs on N-cadherin-Functionalized Oxidized HEA Devices

After demonstrating that the N-cadherin was not present on the PA hydrogel surface after seeding, we tried using a covalent linker, oxidized HEA (oHEA), to create a stronger attachment between the PA hydrogel and the protein patterns. We found that the oHEA increased the number of attached cells on both N-cadherin and Matrigel-patterned devices (Figure 4-9). While there was a much higher attachment and patterning rate, there was also greater non-specific binding, likely due to the fact that the surface of the PA hydrogel was no longer anti-fouling. To prevent non-specific binding, in future work, we incubated the oHEA PA hydrogels with a 1% bovine serum albumin (BSA; ThermoFisher, PI37525) solution in PBS after the N-cadherin incubation.

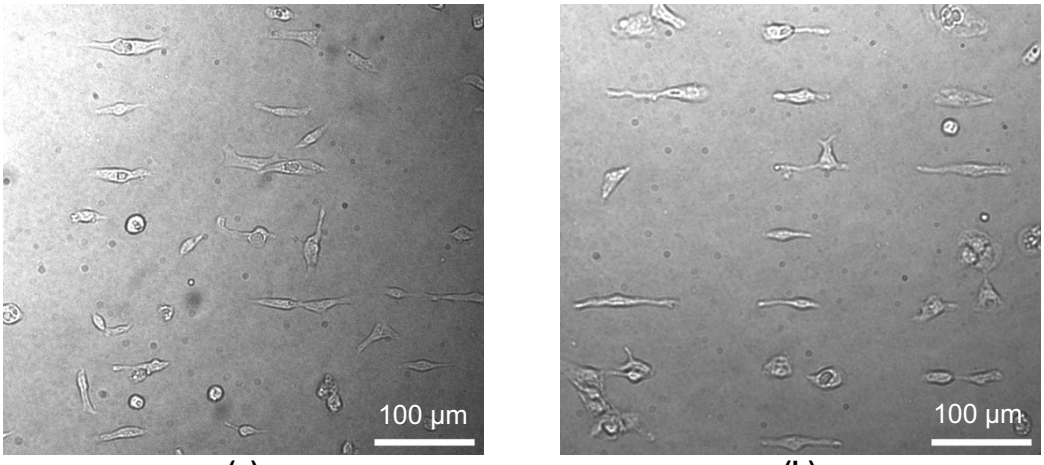

(a) **(b)**

Figure 4-9. hiPSC-CMs attach to N-cadherin patterned on PA hydrogels functionalized with oHEA. Brightfield images of hiPSC-CMs seeded on **(a)** Matrigel patterned on oHEA PA hydrogel and **(b)** N-cadherin patterned on oHEA PA hydrogel.

4.2.3. Discussion

We saw from both the PA hydrogels and the glass devices that hiPSC-CMs prefer Matrigel patterns to N-cadherin patterns. This is unsurprising as Matrigel is a complex mixture of basement membrane proteins that is known to be well suited for stem cell and hiPSC-CM culture [198]. In addition to the preferential attachment to Matrigel-patterned devices, there was more debris or non-specific cell attachment on N-cadherin-patterned glass devices compared to Matrigel-patterned glass devices. The amount of non-specific binding seen on the N-cadherin glass devices was greater than that on the no protein glass controls, indicating that the increased non-specificity was unique to N-cadherin-functionalized devices.

The greater non-specific binding on N-cadherin patterns could be caused by the hiPSC-CMs attaching to the N-cadherin patterns and subsequently producing some of their own ECM proteins [227, 228], which other cells then non-specifically bind to. It is also possible that cells attached to the N-cadherin patterns weakly and therefore did not remain restrained to the pattern area once they laid down their own ECM proteins. Alternatively, the N-cadherin patterns could be weakly attached to the glass surface and be pulled off by the hiPSC-CMs, which would support the hypothesis that the hiPSC-CMs pulled N-cadherin off the PA hydrogels as well. After hiPSC-CM seeding, the glass devices showed very little N-cadherin remaining, while the PA hydrogel devices showed no N-cadherin remaining. This supports the hypothesis that the hiPSC-CMs pull some of the N-cadherin off glass devices and all the N-cadherin off PA hydrogel devices, which matches the seeding results seen in this work. Additionally, we saw strong attachment of hiPSC-CMs on N-cadherin-

patterned oHEA PA hydrogels, indicating that a stronger bond between N-cadherin and the substrate surface is necessary for hiPSC-CM attachment. This is further supported by previous studies done by a previous member of the Pruitt lab, which showed that Madin-Darby Canine Kidney (MDCK) cells could not be anchored on E-cadherin-functionalized PA hydrogels without the presence of a chemical linker [229, 230].

In this work, we have shown that we can pattern N-cadherin on both glass coverslips and PA hydrogels, however, in order to anchor hiPSC-CMs to N-cadherin-patterned PA hydrogels, we have to use a covalent linker, such as oHEA. This allows for future studies to determine the differences in structure and/or function that occur when mimicking cell-cell vs cell-ECM interactions. Developing a method to successfully pattern hiPSC-CMs on PA hydrogels was crucial to being able to achieve dual protein patterning to replicate cell-cell and cell-ECM interactions on one pattern. The dual protein project will be discussed further in the following section.

4.3. Spatial Patterning of Laminin and N-Cadherin for Human Induced Pluripotent Stem Cell-Derived Cardiomyocytes (hiPSC-CMs)

This chapter is reformatted from a paper currently in preparation and includes entire manuscript, including figures and tables. In this chapter, I describe a study I performed as first author creating dual-protein patterned devices for studying hiPSC-CMs and the impact of cell-ECM and cell-cell interactions on hiPSC-CM structure and function. We found that dual-protein patterned hiPSC-CMs showed

some signs of improved structure and function compared to single-protein patterned hiPSC-CMs, including increased cell area and contractility in the direction of sarcomere organization. As first author, I led the conceptualization and experimental work, specifically the transfer of protein patterns to PA hydrogels, hiPSC-CM culture and seeding, and data collection and analysis. I also led the writing of the manuscript and the design of the manuscript figures.

4.3.1. Abstract

Controlling cellular shape with protein micropatterning can mimic physiological morphologies and has been shown to improve reproducibility, enhancing our ability to collect statistics on single-cell behaviors. It has also advanced efforts in developing human induced pluripotent stem cell-derived cardiomyocytes (hiPSC-CMs) as a promising human model for studies of heart structure and function. hiPSC-CMs have key physiological differences from primary human cardiomyocytes (CMs), including lower sarcomere alignment and contractility, smaller area and lower aspect ratio, and lower force production. Protein micropatterning has been demonstrated to make hiPSC-CMs behave more like primary human CMs across these metrics. However, these micropatterned models typically use only extracellular matrix (ECM) proteins and have not investigated whether providing a protein associated with CM-CM interactions, such as N-cadherin, further enhances hiPSC-CM structure and function. Here, we developed a novel dual-protein patterning process to geometrically control single-cell CM placement on deformable hydrogels suitable for traction force microscopy (TFM). The patterns were comprised of rectangular laminin islands for attachment across the majority of the

cell area, with N-cadherin “end-caps” imitating cell-cell interactions. We first photopatterned two proteins on a glass coverslip using a two-step process with photomolecular adsorption of proteins. After both photopatterning steps were complete, we transferred the pattern from the coverslip to a physiologically relevant ~10-kPa polyacrylamide hydrogel. We seeded α-actinin-tagged hiPSC-CMs on the dual-protein-patterned hydrogels and verified interaction between the hiPSC-CMs and the N-cadherin end-caps via immunofluorescent staining. We found hiPSC-CMs on dual-protein patterns have a higher cell area and contractility in the direction of sarcomere organization than those on laminin-only patterns, but no difference in sarcomere organization or force production. While N-cadherin modestly improves the single-cell patterned hiPSC-CM model, it is not sufficient to replicate the role of cell-cell contacts in CM development for *in vitro* hiPSC-CM systems.

4.3.2. Introduction

Human induced pluripotent stem cell derived cardiomyocytes (hiPSC-CMs) are a promising model to bridge the gap between human heart function and the studies of the human heart in animal models [6, 22, 196, 231]. Developments in cardiomyocyte (CM) differentiation protocols have expanded the use of hiPSC-CMs in research [13] and engineering interventions have helped overcome limitations to the use of hiPSC-CMs as models for primary human CMs. These limitations include differences in structure and function between hiPSC-CMs and adult human CMs, such as CM morphology, sarcomere organization, and contractile force [6, 197].

Cardiac organoids or engineered heart tissues (EHTs) offer one approach to improving hiPSC-CM structure and function on average [44-47]. EHTs are commonly composed of hiPSC-CMs supported via some scaffolding, often made of extracellular matrix (ECM) proteins with mechanical properties similar to the myocardium [44]. EHTs mimic the 3D, multicellular environment of human CMs, and exhibit improved structure and function in hiPSC-CM – with sarcomere length and alignment similar to adult human CMs [46, 47]. However, EHTs require large numbers of hiPSC-CMs and supporting cells, show considerable heterogeneity in cell size and shape, and their complexity impedes live-cell imaging of subcellular structures, preventing investigations of sarcomere dynamics [197].

While EHTs provide a more realistic tissue environment for hiPSC-CMs, single hiPSC-CMs are prominently used in studies that seek to investigate intracellular processes, including assessments of cardiotoxicity in pre-clinical drug studies [210, 232-234]. These studies use single-cell hiPSC-CMs to assess changes in contractile dynamics and ion channel function to investigate common and dangerous side effects of drugs before entering into clinical trials [210, 232-234]. For this reason, developing better single-cell hiPSC-CMs is an important goal that could facilitate lower cost and higher throughput drug screening assays.

Protein micropatterning on hydrogels mimicking the mechanical properties of the myocardium provides an engineering approach to improve the structure and function of hiPSC-CM for single-cell assays [15, 31]. Protein micropatterning allows for the control of hiPSC-CM morphology by culturing the cells on rectangular ECM protein patterns in aspect ratios greater than or equal to 5:1, similar to the aspect

ratio of adult human CMs [15, 22, 30, 31]. Patterned hiPSC-CMs present more highly aligned myofibrils and greater contractile forces than unpatterned hiPSC-CMs [15]. With these single-cell hiPSC-CMs, we have a high degree of control over the microenvironment and can study sarcomere dynamics and, by including fiducials in the deformable substrate, we can dynamically monitor force production.

Protein micropatterning has been used with a range of cell types to control cell shape and to create organized arrays of cells that allow for high-throughput imaging and analysis [207, 235]. Additionally, patterned cells have been shown to be more highly reproducible, creating more consistent intracellular phenotypes [207, 235, 236]. Thery and colleagues found that protein micropatterning of human retinal pigment cells created less intercellular variability and greater control over internal organization of the cells [207]. Tseng, et al. found that cell-cell junction positioning of mammary epithelial cells could be controlled by varying the spatial organization of ECM protein micropatterns [235]. Additionally, Rothenberg, et al. found that varying geometries of ECM protein micropatterns affected the number and organization of focal adhesions [236]. The reproducibility and higher control over subcellular organization are important benefits of the single-cell hiPSC-CM model, especially when screening for changing phenotypes, such as in drug studies [210, 232, 233].

Previous studies have investigated the effects of protein micropatterning on hiPSC-CMs, primarily focusing on the ECM proteins. A few studies have investigated CM-CM interactions using N-cadherin-functionalized substrates, culturing rat CMs on N-cadherin-coated polyacrylamide (PA) hydrogels [18] and N-

cadherin-patterned glass [49]. Chopra, et al. coated PA hydrogels with N-cadherin, using anti-Fc antibody as a linking protein and stabilizing the proteins on the hydrogel with the crosslinker sulfo-N-sulfosuccini-midyl-6-(4'-azido-2'-nitrophenylamino) hexanoate (Sulfo-SANPAH) [18]. They then cultured single-cell rat CMs on the N-cadherin-coated hydrogels and found that the CMs produced traction force with a similar magnitude as single-cell rat CMs on ECM proteins [18]. Additionally, they showed that N-cadherin-mediated mechanotransduction is distinct from ECM-mediated mechanotransduction [18]. In another study, Chopra and colleagues patterned single-cell rat CMs on N-cadherin patterns on glass to learn that alpha-catenin serves as an adapter protein for N-cadherin-mediated mechanotransduction [49]. While these studies have provided useful insight into the role of N-cadherin in CM mechanotransduction, their translatability is limited because they are in rat CMs, which have key physiological differences compared to human CMs [4, 5].

Some studies have investigated the role of N-cadherin in the heart using single-cell, multicellular, and whole animal models from rats, mice, cats, and chicks [222-224]. Goncharova, et al. found that blocking N-cadherin inhibits the development and organization of sarcomeres in *in vitro* single-cell rat and chick CMs cultured on glass [222]. Additionally, Simpson and colleagues showed that cell-cell contacts are necessary for *in vitro* feline CMs cultured on laminin-coated petri dishes to stabilize myofibrils and to beat on their own [223]. In a whole animal study, Wu and colleagues showed that N-cadherin and integrin-mediated stabilization of myofibrils occur independently during development [224].

These previous *in vivo* and *in vitro* studies suggest that N-cadherin is relevant to CM structure, function, and development [18, 49, 222-224]. These studies used cells from animal models, limiting the relevance to the human heart. Additionally, all but one [18] used non-physiologic stiffness substrates and could not monitor CM contractile dynamics. Here, we bridge these gaps using single-cell hiPSC-CMs on protein-patterned deformable hydrogels suitable for traction force microscopy (TFM). The single-cell hiPSC-CM model allows us to investigate the impact of N-cadherin adhesions in human CM structure, including subcellular structures like sarcomeres, but also their contractile function.

Here, we asked whether pattering both laminin (an ECM protein secreted by CMs and abundant in their native microenvironment) and N-cadherin improves the structure and function of single-cell hiPSC-CMs. To answer this, we developed a method for consistent and precise dual-protein patterning on deformable hydrogels, and tested the effects of these substrates on single-cell hiPSC-CMs. N-cadherin is a relatively short (130 kDa), asymmetric protein which requires rotational freedom for proper conformation and binding [237]. To ensure the covalent attachment of functional N-cadherin, we adapted a protocol from Sarker, et al. [33] for the covalent attachment of Protein A as a linker to bind N-cadherin with an Fc-domain [226]. We used our protein micropatterning method to imitate both CM-ECM and CM-CM interactions for single-cell hiPSC-CMs. We hypothesized that utilizing the dual-protein patterning to imitate CM-ECM and CM-CM interactions would improve hiPSC-CM structure, e.g., cell spread area, sarcomere alignment, and contractile function, i.e., sarcomere contractility and force production.

4.3.3. Results and discussion

We created two single cell patterns: i) single protein patterns consisting of laminin rectangles, and ii) dual protein patterns, consisting of laminin rectangles flanked by N-cadherin caps (Figure 4-10a). We patterned arrays of alternating single and dual protein patterns on each coverslip. We then transferred the protein patterns to a ~6.8-kPa polyacrylamide (PA) hydrogel. We verified the patterning and the pattern transfer to PA hydrogel using a laminin antibody and a pan-cadherin antibody (Figure 4-10a). Finally, we seeded hiPSC-CMs on the patterns (Figure 4-10b) and assessed their morphology, force production, and sarcomere organization and contractility on the laminin-only and dual-protein patterns.

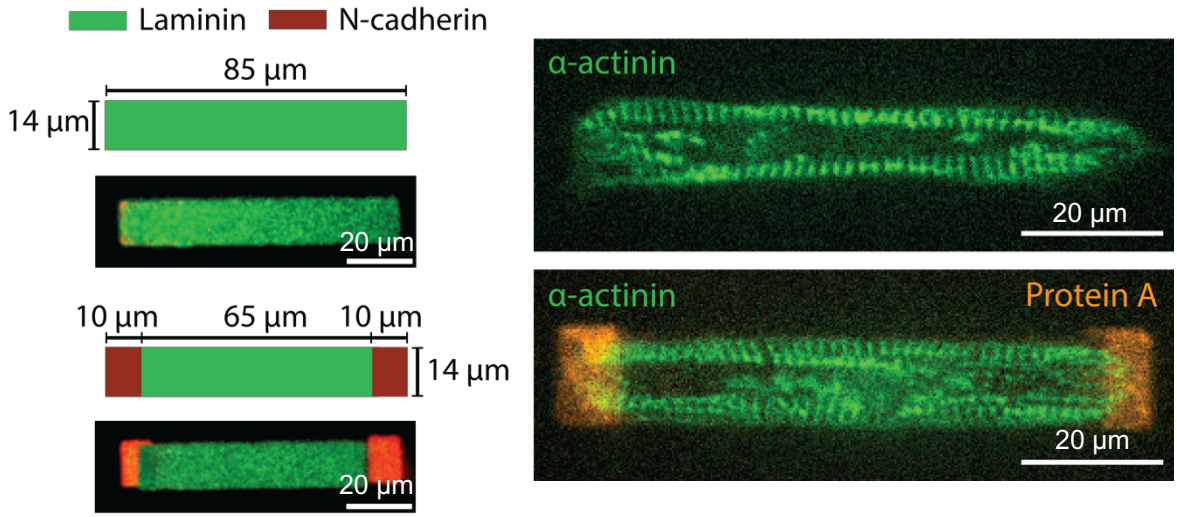

Figure 4-10. Dual-protein and laminin-only patterns. (a) Schematics and representative images of fluorescently labelled laminin-only and dual-protein patterns on PA hydrogels. Green is laminin and red is N-cadherin. **(b)** Representative image of hiPSC-CMs on laminin-only (top) and dual-protein (bottom) patterns, with sarcomeres (green) and Protein A (orange) visible.

4.3.3.1. Mechanical characterization of polyacrylamide hydrogels

We used AFM to characterize four polyacrylamide hydrogels (Figure 4-11). Using the Hertz model (Figure 4-11a), we found the mean stiffness of the polyacrylamide hydrogels to be 6.8 kPa, with a standard deviation of 1.5 kPa.

We used multiple AFM cantilevers due to PA hydrogel build-up on cantilever tips after ~10-20 measurements. The three cantilevers had the following properties: (1) r_t = 10μm, k_c = 0.184N/m, sensitivity = 0.047V/nm, (2) r_t = 10μm, k_c = 0.060N/m, sensitivity = 0.027V/nm, and (3) r_t = 3.46μm, k_c = 0.191N/m, sensitivity = 0.042V/nm.

We compared the data from each cantilever using a Kruskal–Wallis one-way analysis of variance test to ensure that the results were consistent. There was no statistically significant difference between any of the data sets, including the data set containing all of the datapoints together (p-values between 0.44 and >0.9999; Figure 4-11b).

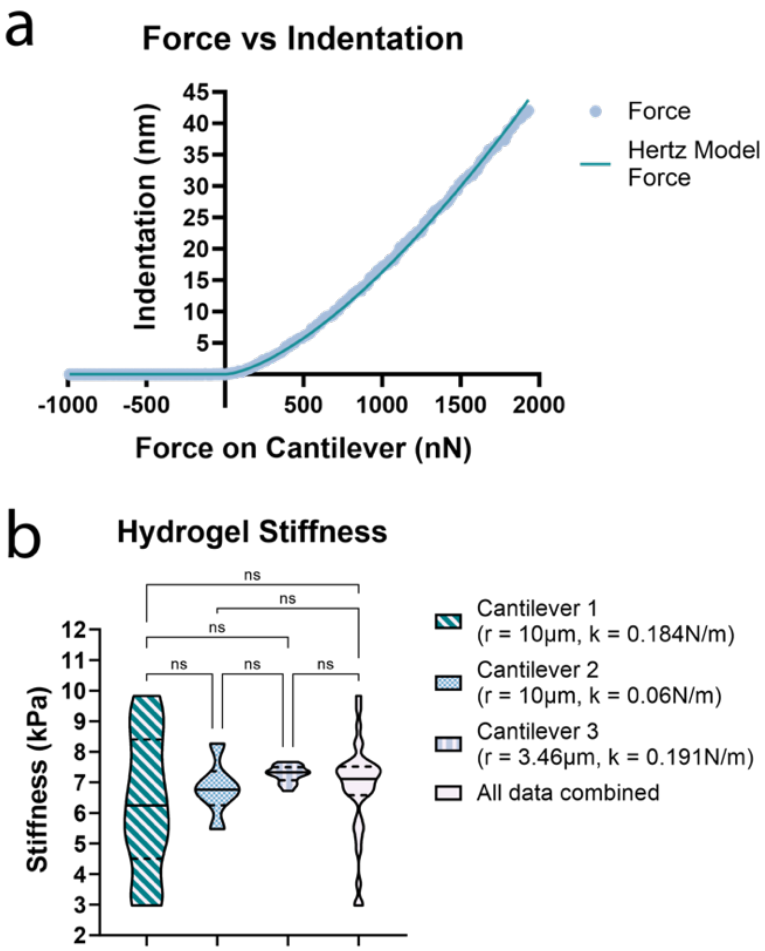

Figure 4-11. Mechanical characterization of polyacrylamide hydrogels. (a) Representative example of a force-indentation curve for a hydrogel, with measured force (light blue circular markers) plotted alongside the Hertz model calculated force (teal line). **(b)** PA hydrogel stiffness measurements with each cantilever. For stiffness data, n = 31. In (b), centerlines indicate medians, dotted lines indicate 25th and 75th percentiles.

4.3.3.2. Validation of hiPSC-CM interaction with N-cadherin on dual-protein patterns

We first sought to verify that the hiPSC-CMs were interacting with the N-cadherin end-caps on the dual-protein patterns. We stained hiPSC-CMs on dual-protein patterns with a pan-cadherin primary antibody and AlexaFluor-647 secondary antibody.

We manually outlined each cell in FIJI (ImageJ) as described in *Methods*. We outlined the N-cadherin end-cap using the 647 channel (N-cadherin). We isolated the overlap between the cell outline and the N-cadherin end-cap and quantified the average fluorescence intensities in the overlap area and the N-cadherin end-cap area (Figure 4-12a).

We compared the two conditions using a two-tailed Wilcoxon matched-pairs signed rank test, which is equivalent to a non-parametric, paired T-test. We observed a significant difference ($p < 0.0001$) between the intensity of N-cadherin signal where the hiPSC-CMs overlapped the N-cadherin patterns and the intensity of the N-cadherin patterns themselves (Figure 4-12a). This overlap confirms that the hiPSC-CMs localized endogenous N-cadherin on the N-cadherin pattern and were interacting with the N-cadherin patterns.

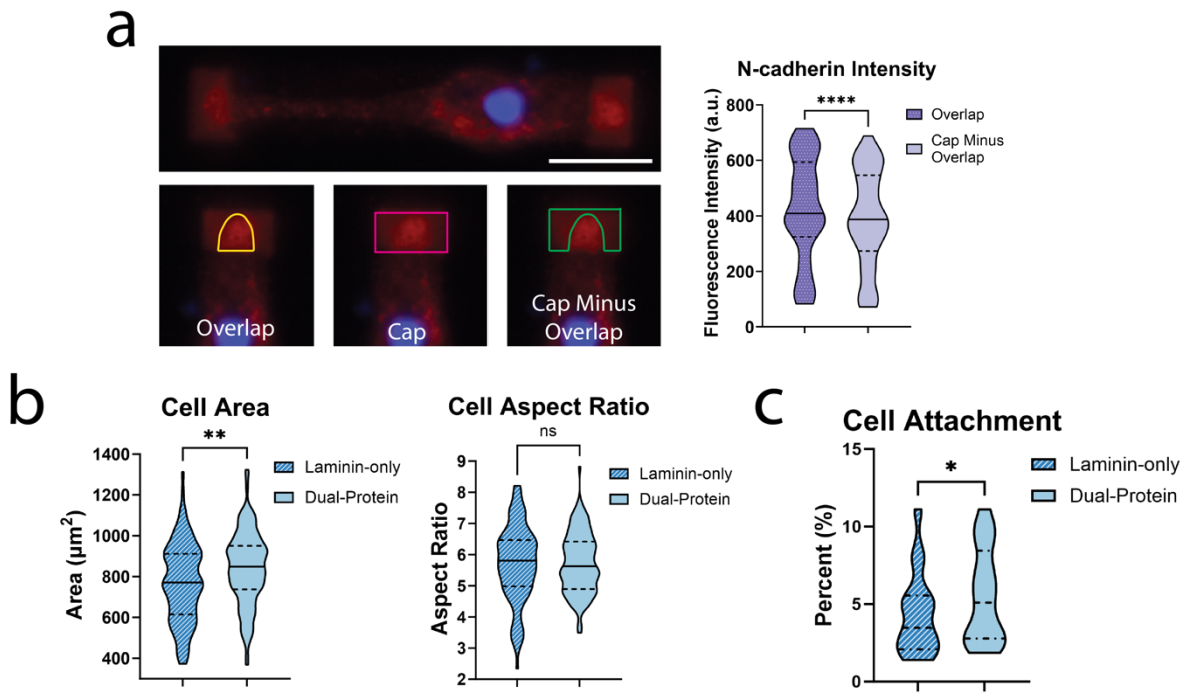

Figure 4-12. Dual-protein-patterned hiPSC-CMs have greater cell area than those on laminin-only patterns. (a) Verification of hiPSC-CM interaction with N-cadherin. hiPSC-CM stained for N-

cadherin (red) and cell nucleus (blue). Overlap of cell and N-cadherin measured using the outlines shown and the resulting fluorescent intensities of the overlapping area and the end-cap area without the overlap are visualized in the plot to the right. For N-cadherin verification data, n = 62. **(b)** hiPSC-CM cell area and aspect ratio and **(c)** attachment rates of hiPSC-CMs on laminin-only (right) and dual-protein (left) patterns. For cell area, aspect ratio, and attachment data, n = 116 for laminin-only patterned condition and n = 131 for dual-protein patterned condition. For all plots, centerlines indicate medians, dotted lines indicate 25th and 75th percentiles. P-values with significance at P<0.05 are designated with (*), P<0.005 are designated with (**), P<0.0005 are designated with (***), and P<0.0001 are designated with (****). Scale bar is 20μm.

4.3.3.3. hiPSC-CMs on dual-protein patterns have increased cell area and attachment rates

To investigate the effect of dual-protein patterns on hiPSC-CM structure, we assessed cell area and aspect ratio, as well as the rate of attachment of hiPSC-CMs to laminin-only and dual-protein patterns.

Most studies that pattern hiPSC-CMs use rectangles with an aspect ratio of 5:1 to 7:1, corresponding to the range of adult human ventricular CMs [15, 22, 30]. In early experiments, we used patterns with an aspect ratio of 7:1, but found most cells did not fill the entire pattern, meaning many did not reach the N-cadherin end-caps on the dual-protein patterns. We adjusted the length of the patterns to address this issue, bringing our pattern aspect ratio down to ~6:1.

The cell area and aspect ratio of the hiPSC-CMs were assessed by drawing an outline of the cell in FIJI, as described in Methods. The areas of hiPSC-CMs on dual-protein patterns were larger than those of laminin-only patterns, with average

areas of 824.4μm^2 and 739.9μm^2, respectively (P = 0.0023; Figure 4-12b). For reference, the total pattern area is 1190μm^2.

The mean aspect ratios of hiPSC-CMs on the laminin-only and dual-protein patterns were 5.4 and 5.5 respectively (Figure 4-12b). The laminin-only-patterned hiPSC-CMs had a larger variance than the dual-protein-patterned hiPSC-CMs, with standard deviations of 1.21 and 0.96, respectively (F-test p = 0.0085). The mean aspect ratios were compared using an unpaired, two-tailed T-test with Welch's correction and had no significant difference (P = 0.8705). These results confirm that both laminin-only and dual-protein patterns support spreading of hiPSC-CM near the patterned aspect ratio.

In addition to hiPSC-CM area and aspect ratio, we considered whether the addition of N-cadherin end-caps influenced the rate of cell attachment. To determine attachment rates, we counted the number of single-cell hiPSC-CMs attached to each pattern type. For this data, we included all cells on dual-protein patterns, regardless of whether they overlapped an N-cadherin end-cap or not. We assessed the difference in attachment rates using a parametric, two-tailed, ratio paired T-test. The rate of attachment was higher on dual-protein patterns than laminin-only patterns, with average attachment rates of 5.5% and 4.3%, respectively, on seventeen total devices (P = 0.0441; Figure 4-12c). This increased attachment suggests that dual-protein patterns may promote increased hiPSC-CM attachment rates, even if the hiPSC-CMs didn't overlap the N-cadherin end-caps at the time of fixation/imaging.

4.3.3.4. hiPSC-CMs on dual-protein patterns have increased contractility in the direction of sarcomere alignment

To investigate the effect of dual-protein patterns on hiPSC-CM function, we analyzed the contractility of the hiPSC-CM sarcomeres. Sarcomeric contractility is a commonly used metric to compare hiPSC-CMs to adult human CMs, with adult human CMs exhibiting greater contractility than hiPSC-CMs [6, 15, 22].

We analyzed sarcomere contractility and organization using a previously published, open-source program called Sarc-Graph [238]. Sarc-Graph segments videos of fluorescently-tagged sarcomeres in beating hiPSC-CMs and outputs parameters representing the orientation, spacing, and contractility of the sarcomeres, all of which are important metrics for hiPSC-CM structure and function [238].

In overall sarcomere shortening, we did not see a significant difference between hiPSC-CMs on laminin-only vs dual-protein patterns (Figure 4-13a). The percent shortening is calculated by taking the difference between the maximum and minimum length for an individual sarcomere and dividing it by the average length of the sarcomere [238]. The percent sarcomere shortening for all of the sarcomeres in one cell are averaged to calculate a single percent sarcomere shortening for each hiPSC-CM. The mean percent sarcomere shortening for laminin-only and dual-protein patterns were not significantly different, with values of 16.89% and 17.67%, respectively ($P = 0.6273$). To further investigate sarcomere contractility, we assessed $C_{||}$, a parameter calculated by Sarc-Graph that relates sarcomere

contractility to sarcomere alignment and represents the shortening of the entire cell domain in the direction of dominant sarcomere orientation [238].

To define $C_{||}$, we first need to understand how Sarc-Graph defines sarcomere alignment. Zhao, et al. use a structural tensor to quantitatively assess the sarcomere orientation, defining the structural tensor with the equation

$$\mathbb{T} = \langle 2\begin{bmatrix} r_x^i r_x^i & r_x^i r_y^i \\ r_y^i r_x^i & r_y^i r_y^i \end{bmatrix} - \begin{bmatrix} 1 & 0 \\ 0 & 1 \end{bmatrix} \rangle$$

where $\mathbf{r} = [r^i_x, r^i_y]$ is a unit vector representing the orientation of the i^{th} sarcomere [238]. The structural tensor has eigenvalues of a_{max} and a_{min}, with a_{max} providing the magnitude of sarcomere alignment (OOP). The eigenvectors of the structural tensor are $\mathbf{v}_{max}$ and $\mathbf{v}_{min}$, with $\mathbf{v}_{max}$ representing the direction of sarcomere alignment [238].

Now, to define the contractility, Zhao and colleagues define the deformation gradient $\mathbf{D}_{avg}$ with the equation

$$\mathbf{D}_{\mathrm{avg}}\mathbf{\Lambda}_0 = \mathbf{\Lambda}$$

where $\mathbf{\Lambda}_0 = [\mathbf{v}_{01}, \mathbf{v}_{02}, \ldots, \mathbf{v}_{0n}]$, representing the vectors $\mathbf{v}$ that connect neighboring sarcomeres in the initial reference frame, and $\mathbf{\Lambda} = [\mathbf{v}_1, \mathbf{v}_2, \ldots, \mathbf{v}_n]$, representing the vectors $\mathbf{v}$ connecting neighboring sarcomeres in the current deformed frame [238].

Zhao, et al. relate the deformation gradient back to the sarcomere alignment expressions with the equation $\mathbf{v}_{\mathrm{max}} = \mathbf{D}_{\mathrm{avg}}\mathbf{v}_0$ [238], where $\mathbf{v}_{max}$ is the eigenvector representing the direction of sarcomere alignment in the contracted (deformed) state and $\mathbf{v}_0$ representing the direction of sarcomere alignment in the relaxed (initial) state [238]. They then define $C_{||}$ as

$$C_{||} = \frac{|\mathbf{v}_0| - |\mathbf{v}_{\mathrm{max}}|}{|\mathbf{v}_0|},$$

representing the fractional shortening of the sarcomeres in the direction of sarcomere alignment [238].

We found that hiPSC-CMs on dual-protein patterns had larger $C_{||}$ values, with an average of 0.041 compared to 0.029 for laminin-only-patterned hiPSC-CMs (P = 0.0294; Figure 4-13a). This result suggests that the contractility of the sarcomeres along the long axis of the myofibrils is enhanced in hiPSC-CMs patterned with N-cadherin end-caps mimicking CM-CM interactions.

We determined the statistical significance with an unpaired T-test with a Welch's correction for the unequal variance (F-test P = 0.0403) in the dual-protein-patterned data (standard deviation = 0.026) compared to the laminin-only-patterned data (standard deviation = 0.019).

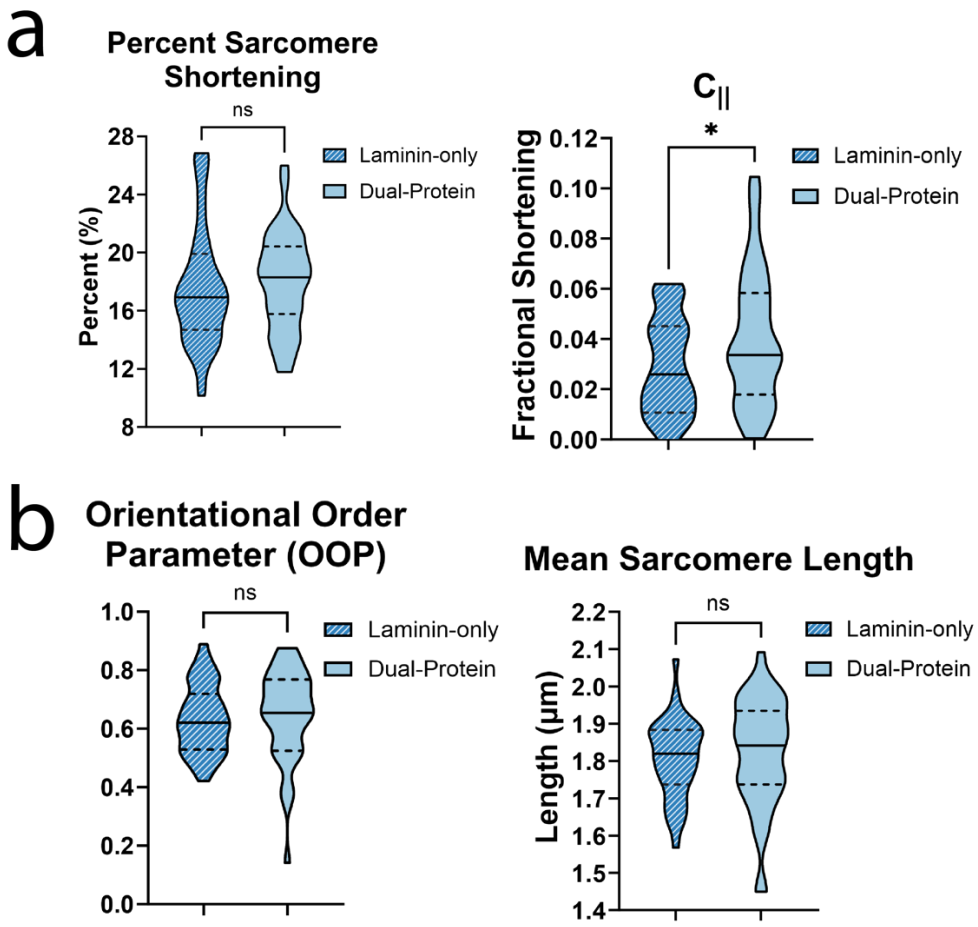

Figure 4-13. Dual-protein-patterned hiPSC-CMs have higher contractility in the direction of sarcomere organization, but no difference in sarcomere alignment compared to laminin-only-patterned hiPSC-CMs. (a) Overall percent sarcomere shortening and fractional sarcomere shortening in the direction of sarcomere organization ($C_{||}$) for hiPSC-CMs on laminin-only and dual-protein patterns. **(b)** OOP and mean sarcomere length for hiPSC-CMs on laminin-only (right) and dual-protein (left) patterns. For both laminin-only and dual-protein patterned conditions, n = 39. For all plots, centerlines indicate medians, dotted lines indicate 25th and 75th percentiles. P-values with significance at P<0.05 are designated with (*).

4.3.3.5. hiPSC-CM sarcomere organization is similar on laminin-only and dual-protein patterns

We further examined the impact of dual-protein patterning on hiPSC-CM structure by analyzing sarcomere structure and organization. Previous studies have suggested that adult CMs have average sarcomere lengths of ~2.2 μm, while immature CMs have average sarcomere lengths of ~1.6 μm [22].

To investigate sarcomere structure and organization, we assessed hiPSC-CM sarcomere lengths and the orientational order parameter (OOP), a metric commonly used to assess sarcomere organization in CMs that ranges from zero (random orientation) to 1 (perfectly aligned) [238]. We hypothesized that hiPSC-CMs on dual-protein patterns would have more highly organized sarcomeres because previous studies found that N-cadherin is important in sarcomere formation and organization [18, 41, 49, 222-224]. Surprisingly, sarcomeric organization, as assessed via the OOP, was not significantly different between hiPSC-CMs on laminin-only and dual-protein patterns, with average values of 0.6330 and 0.6254, respectively ($P = 0.6205$; Figure 4-13b). The lack of difference in sarcomere organization between laminin-only and dual-protein patterned hiPSC-CMs suggests that the patterned N-cadherin end-caps are not sufficient to increase organization.

We also found no difference between the mean sarcomere lengths of hiPSC-CMs on laminin-only and dual-protein patterns. Both groups had mean sarcomere lengths of 1.8 μm, with minimum and maximum sarcomere lengths of 1.7 μm and 2 μm, respectively ($P = 0.6193$; Figure 4-13b). We assessed the statistical significance using an unpaired T-test with a Welch's correction because the standard deviations of the laminin-only and dual-protein data, 0.10 μm and 0.14 μm, respectively, were significantly different (F-test $p = 0.0408$).

4.3.3.6. hiPSC-CM force production is similar on laminin-only and dual-protein patterns

To further investigate the impact of dual-protein patterning on hiPSC-CM function, we assessed force production of hiPSC-CMs with Traction Force Microscopy (TFM), using the streamlined TFM module of a custom, open-source code called CONTRAX [214, 239]. The streamlined TFM module of CONTRAX provides a user-friendly TFM analysis tool that reads in fluorescent microbead displacement videos and assesses a number of functional metrics, including traction force [214, 239, 240].

We looked at multiple parameters output by CONTRAX, including total force production, peak traction stress, average contraction displacement, and contraction velocity. We also assessed total contractile moment, which is a scalar value representing the sum of moments taken at the center of the cell [241], and total impulse, which is the integrated area under the curve from the force versus time plot [214].

Force production, average contraction displacement, and contraction velocity are all directly related to hiPSC-CM contractility and are commonly used to assess CM function [15, 242, 243]. The peak traction stress avoids the homogenization caused by integrating over the cell area, providing insight into the maximum stress produced by each cell.

Total force production is calculated by integrating the traction stresses over the cell area at each time point, creating a trace of force versus time, and identifying the maximum amplitude of the trace peaks [214, 239, 240]. To assess average

contraction displacement, CONTRAX averages the displacement magnitudes over the cell area for each video frame. CONTRAX then creates a one-dimensional trace of average displacement over time and extracts the displacement between the fully contracted and fully relaxed states [214, 239]. CONTRAX calculates the contraction velocity using the same displacement versus time trace, dividing the contraction displacement by the time elapsed during contraction [214, 239]. Peak traction stress is extracted by identifying the timepoint with greatest traction stress and reporting the highest absolute value of traction stress within that timepoint.

The total contractile moment provides information about the distribution of stresses by weighting the traction forces by their distance from the cell center. We hypothesized that the force production of hiPSC-CMs might be more concentrated at the N-cadherin end-caps compared to the hiPSC-CMs on laminin-only patterns. The contractile moments are calculated by multiplying the traction force by the distance from the cell center, using the equation

$$M_{ij} = \left(\frac{1}{2}\right) \int d^2r \left[x_i T_j(\vec{r}) + x_j T_i(\vec{r})\right] = -\left(\frac{i}{2}\right) \left[\frac{\partial \widetilde{T}_j(\vec{k})}{\partial k_i} + \frac{\partial \widetilde{T}_i(\vec{k})}{\partial k_j}\right] \Bigg|_{\vec{k}} = 0$$

where $\vec{T}(\vec{r})$ is the traction vector at point $\vec{r}$ on the hydrogel surface [241]. The second expression represents the equation in Fourier space, which we operate in when using Fourier Transform Traction Cytometry (FTTC; see *Methods*). The tilde indicates the two dimensional Fourier transform with wave vector $\vec{k}$ [241]. Using *x* and *y* for indices *i* and *j*, we have four possible equations representing scalar values: M_{xx}, M_{yy}, M_{xy}, and M_{yx}. M_{xy} and M_{yx} represent torque on the substrate due to the traction forces, and M_{xx} and M_{yy} represent contractile forces weighted by their

distance to the center of the cell [241]. To look at the weighted contribution of *x*- and *y*-forces to the cell contraction, we look at the total contractile moment by adding the *x*- and *y*-contractile moments together: $\mu = M_{xx} + M_{yy}$ [241].

The total impulse is calculated by calculating the area under the force versus time trace [214, 244]. It is equivalent to the tension-integral parameter used in a previous study that found that hypertrophic and dilated cardiomyopathies could be differentiated in hiPSC-CMs by the tension-integral magnitude [244]. We did not expect to see a difference in total impulse between our two conditions, but assessed the parameter to verify that there was no difference.

For all of these parameters except for average contraction displacement and contraction velocity, we used the peak measurements, meaning the values calculated when the cell is either fully contracted or fully relaxed. Our analysis tools assume these are quasi-static states; however, we note this assumption is violated during active contraction or relaxation occurring across all frames of our ~800 frame videos.

We did not find significant differences between total force, peak stress, average contraction displacement, contraction velocity, total contractile moment, or total impulse (Figure 4-14). This result is consistent with the overall contractility result, further indicating that the difference in functional outputs of hiPSC-CMs on laminin-only and dual-protein patterns are modest.

Within both laminin-only and dual-protein pattern conditions, we saw a large variance in force production, as can be seen in Figure 4-14a. For the laminin-only-

patterned hiPSC-CMs, the mean force was 104.1nN +/- 98.2nN, while the dual-protein-patterned hiPSC-CMs had an average force of 118.3nN +/- 107.1nN.

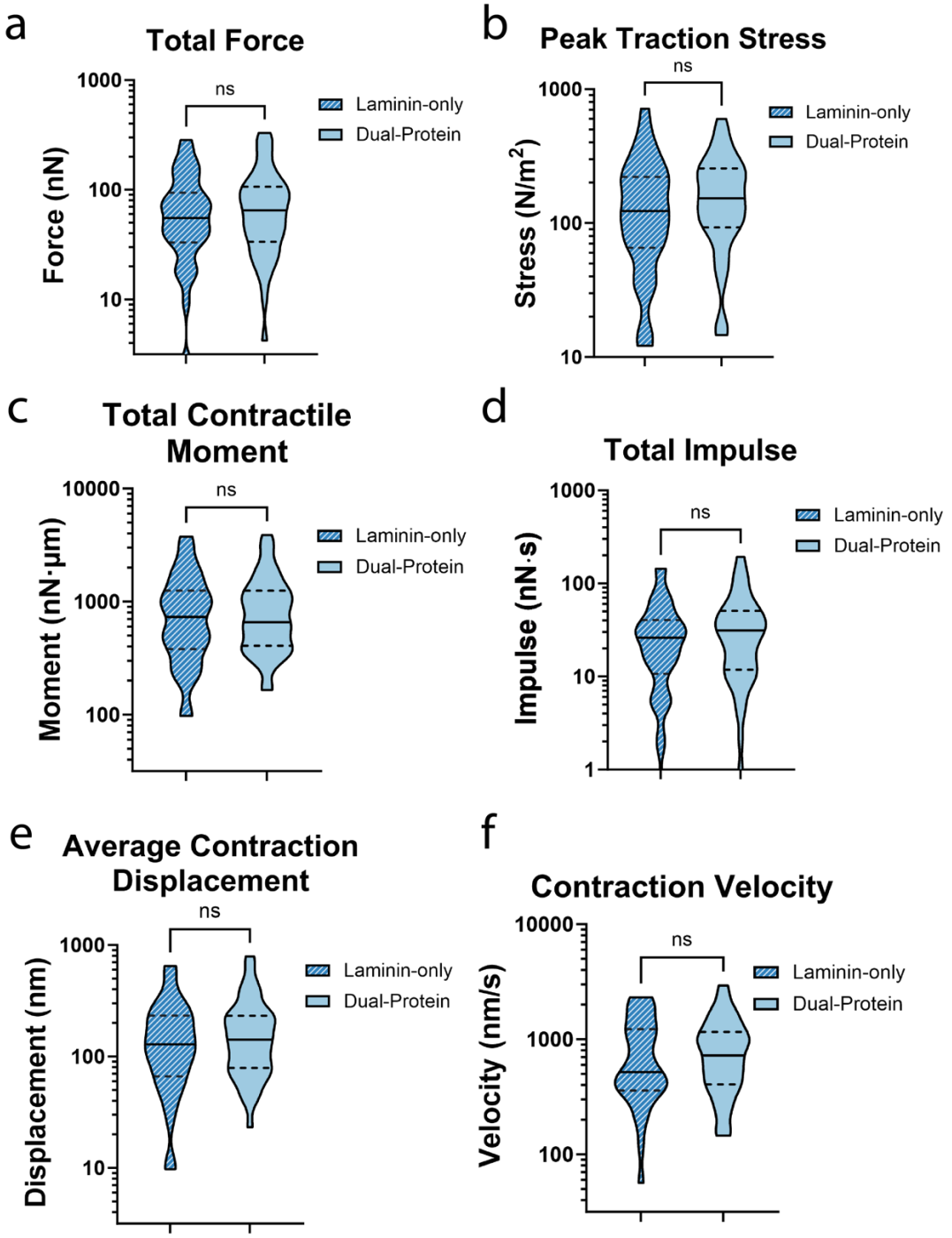

Figure 4-14. Dual-protein-patterned hiPSC-CMs demonstrate no difference in (a) total force, (b) peak traction stress, (c) total contractile moment, (d) total impulse, (e) average contraction

displacement, and (f) contraction velocity compared to laminin-only-patterned hiPSC-CMs. For all data in this figure, N = 81 with n = 35 for laminin-only and n = 46 for dual-protein condition. For all plots, centerlines indicate medians, dotted lines indicate 25^{th} and 75^{th} percentiles.

All of the parameters reported by CONTRAX, including those assessed above, are single scalar values for each cell. These parameters allow for quantification of force production but result in the loss of spatial information of hiPSC-CM contractility. This flattening of spatially distributed forces into scalar values is necessary to quantify and assess data sets that consist of ~800 frames per video and hundreds of displacement data points in each frame of each video. While the scalar outputs provide quantifiable comparisons between cells, the spatial information can contain differences in force distribution that are not discernible in scalar variables. To investigate the spatial distribution of force production for each condition, we averaged the peak contraction traction stress heatmaps of all the cells in each condition (Figure 4-15), with 34 cells in the laminin-only condition and 46 cells in the dual-protein condition. We visually see a difference between the traction stresses in the laminin-only and dual-protein-patterned conditions, with the peak stresses appearing to occur closer together in dual-protein-patterned hiPSC-CMs compared to laminin-only-patterned hiPSC-CMs. The inward shift in peak traction stress location for the hiPSC-CMs on dual-protein patterns could be reflecting the inward shift of the laminin pattern boundary compared to the laminin-only patterns. The red squares in Fig 4-15a indicate the location of the N-cadherin end-caps and the peak traction stresses occur within the laminin portion of the dual-protein patterns. This suggests that the focal adhesions still drive the traction force production in hiPSC-CMs on dual-protein patterns. Additionally, we see lower

traction stresses in the laminin-only-patterned hiPSC-CMs compared to the dual-protein-patterned hiPSC-CMs.

While the location of peak traction stress appears to have moved toward the cell center, the area of the peak traction stress is larger in dual-protein-patterned hiPSC-CMs compared to laminin-only-patterned hiPSC-CMs. The areas of peak traction stress for the laminin-only patterns on the left and right are 170 μm^2 and 155 μm^2, respectively. For the dual-protein patterns, the areas of peak traction stress on the left and right are 310 μm^2 and 292 μm^2, respectively. This could suggest that while the mechanotransduction occurs near the boundary of the laminin pattern, the hiPSC-CMs on dual-protein patterns are establishing larger mechanical connections to the patterns.

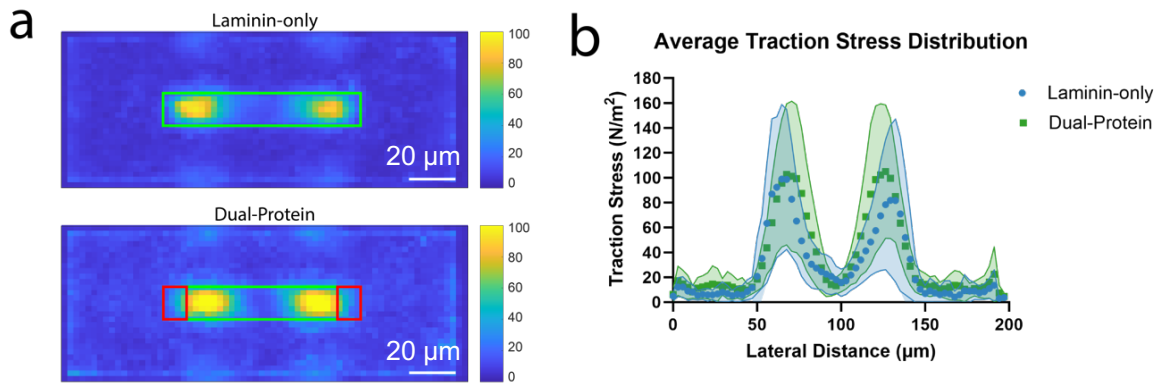

Figure 4-15. Spatial distribution of average traction stresses produced by hiPSC-CMs on laminin-only and dual-protein patterns. (a) Peak contraction traction stress heatmaps averaged over all cells in both laminin-only (n = 34) and dual-protein (n = 46) conditions. Green rectangles represent an estimation of the locations of laminin patterns, red rectangles represent an estimation of the locations of N-cadherin patterns. Color bars are in units of Pascals. **(b)** Mean traction stress distribution with respect to lateral distance, averaged over a ~10 μm width in the center of each heatmap. The shaded areas represent the standard deviations. Scale bars are 20 μm.

4.3.4. Conclusions

In this work, we have developed a method for precise patterning of multiple proteins on a single device and applied this method to create patterns mimicking cell-cell and cell-ECM interactions for hiPSC-CMs. Our method applies a novel dual patterning method to functional cellular studies. We have demonstrated the use of the method by making dual-protein patterns to mimic cell-cell interactions for single-cell hiPSC-CMs. Our results indicate that our dual-protein patterning increases hiPSC-CM attachment rates, spread area, aspect ratio, and the efficiency of sarcomere contraction along myofibrils. We found no significant difference in force production, overall sarcomere contractility, and sarcomere organization between laminin-only and dual-protein patterned hiPSC-CMs, suggesting that N-cadherin end-caps offer modest benefit alone. More complexity is likely necessary to improve hiPSC-CM structure and function beyond single ECM patterning alone.

In addition to greater complexity in the patterning approach, more detailed spatial analysis of force production and sarcomere contractility could provide more insight into the differences between laminin-only and dual-protein-patterned hiPSC-CMs. Detailed spatial analysis is made difficult by the high quantity of data – there are almost 2,000 data points per frame, 800 frames per cell, and ~40 cells per condition. In addition to the high volume of data, the data are heterogeneous, with variations in the time point of peak contraction for each cell as well as variations in cell area and cell location in relation to the pattern.

In future work, it would be advantageous to write a script to process the corresponding 546nm fluorescence images along with the brightfield and microbead

TFM images, to determine the location of the cell with respect to the protein pattern. Additionally, a script could be written to isolate the traction stress data for one frame at peak contraction for each cell and further extract the average line profile of the center of the stress map to allow for comparison between multiple cells for each condition. These developments could allow for more detailed analysis of the distribution of force production with respect to the single- and dual-protein patterns, which would potentially illustrate differences in mechanotransduction of hiPSC-CMs on the dual-protein patterns.

One potential target for improving this model would be including a desomocollin protein, a cadherin-family protein that occurs in desmosomes [245]. Lowndes and colleagues found that patterning a specific desmocollin, Dsc2a, on glass drove Madin-Darby canine kidney cells to recruit desmosome-specific intracellular proteins and create strong adhesive bonds [245]. Including a desmosome-specific protein, along with N-cadherin, could provide more cues mimicking CM-CM junctions to the hiPSC-CMs, improving structural and functional metrics more pronouncedly.

Dual protein patterning improves our single-cell hiPSC-CM model by increasing cell area and cell attachment, as well as slightly improving sarcomere contractility. These moderate improvements suggest that more complexity is necessary to replicate cell-cell contacts for patterned single-cell hiPSC-CMs. The small improvements are promising indications that successfully mimicking cell-cell contacts for single-cell hiPSC-CMs could further enhance their structure and function, improving the hiPSC-CM model for future studies of the heart.

4.3.5. Methods

4.3.5.1. Protein patterning glass coverslips

N-cadherin is an asymmetric protein and a linking protein is necessary to ensure the extracellular binding site is available when patterning N-cadherin [226, 229, 246]. In this work, we used an N-cadherin Fc chimera (R&D Systems, 1388-NC-050) and a 546-nm fluorescently tagged Protein A (ThermoFisher, P11049) as our linking protein. Protein A is a protein with a high affinity to Fc-regions of IgG molecules [247]. It has been previously used to ensure the correct orientation of E-cadherin [229, 248]. The Fc region of the N-cadherin chimera protein binds to the Protein A, ensuring the correct orientation of the N-cadherin on the device surface.

To begin protein micropatterning, we activated 18mm diameter #1 glass coverslips with oxygen plasma for 5 minutes at 18W (Harrick, PDC-32G). Immediately after plasma treatment, we sealed an 8mm inner diameter silicone ring (B&J Rubber Products) to the center of the glass coverslip. The silicone ring was cut from a Silhouette CAMEO 3 electronic desktop cutter (Silhouette America). We immediately pipetted a solution of 100 µg/mL of poly(l-lysine)-graft-poly(ethylene glycol) (PLL(20)-g[3.5]- PEG(2); SuSoS AG) diluted in phosphate buffered saline (PBS; Gibco, ThermoFisher, 10010049) within the ring and incubated for 1 hour at room temperature. We rinsed the PLL-g-PEG thoroughly (10x) with PBS prior to micropatterning. Following PLL-g-PEG incubation and rinsing, we pipetted 20µL of UV sensitive photoinitiator (PLPP; Alvéole) into the silicone ring on the glass coverslip. Then we placed the glass coverslip on the stage of a Leico Dmi8 epifluorescence microscope equipped with a Fluotar 20x/0.40 NA objective and the

Alvéole Primo photopatterning system (Alvéole) with a 375 nm, 7.10 mW laser. We made digital masks for the protein A “end-cap” patterns as well as the main laminin patterns using the open-source software Inkscape (https://inkscape.org). We used the pixel-to-micron ratio generated by Primo calibration to define the geometries of all patterns. We defined two patterns for constraining the single-cell hiPSC-CM: 1) 14 μm x 85 μm laminin-only patterns; and 2) 14 μm x 85 μm dual-protein patterns. Dual protein patterns are comprised of Protein A end-cap patterns (14 μm x 10 μm) overlapped with laminin rectangles (14 μm x 69 μm) by ~10% to mitigate any alignment artifacts.

We loaded the digital masks into the Leonardo plugin (Alvéole Laboratory) on Micro-Manager software [249], and made a 6 by 6 array with 150 μm spacing between each instance of the patterns. We illuminated the glass coverslip with the first digital mask for the Protein A end-caps at a dosage of 1,000mJ/mm^2. Following micropatterning, we rinsed off the photo initiator with PBS and incubated the glass coverslip with 100 μL of a 100 μg/mL solution of 546-nm fluorescently tagged Protein A overnight at 4°C. We then thoroughly rinsed the Protein A from the glass coverslip using PBS and added another 20 μL of PLPP photoinitiator. We illuminated the glass coverslip with the second digital mask for the laminin rectangles at a dosage of 1,000 mJ/mm^2. We designed the array of patterns to alternate between dual-protein and laminin-only patterns. Before UV illumination, we aligned the shortened laminin bodies within the digital mask to the already-patterned protein A end-cap patterns using a Texas Red fluorescent excitation filter. Following this second UV illumination step, we rinsed off the photoinitiator with PBS

and incubated the glass coverslip with a 500 µg/mL solution of laminin (Corning, 354232) for 2 hours at room temperature. For pattern verification experiments, we incubated the glass coverslip with a 500 µg/mL solution of green fluorescent laminin (Cytoskeleton, Inc., LMN02) for 2 hours at room temperature. Finally, we rinsed the patterns with PBS and removed the silicone containment ring prior to gel transfer. A schematic of the protein micropatterning process flow can be seen in Figure 4-16a.

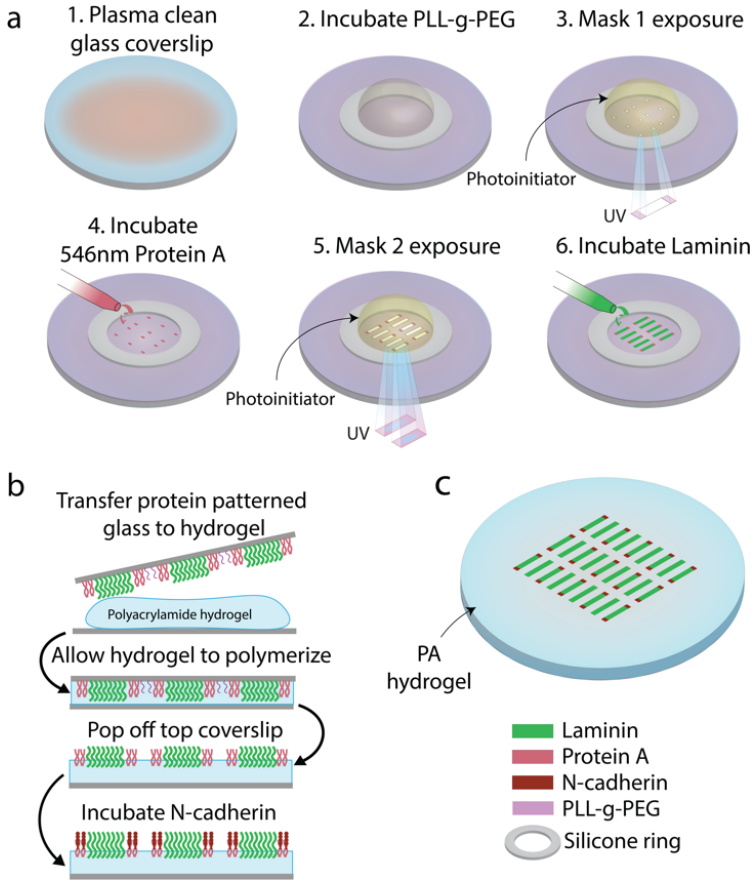

Figure 4-16. Dual-protein patterning of PA hydrogels. (a) Process flow of dual-protein patterning on a glass coverslip using photomolecular adsorption. **(b)** Process flow of transfer of dual-protein pattern from glass coverslip to PA hydrogel and incubation of N-cadherin. **(c)** Schematic of final result – alternating laminin-only and dual-protein patterns on PA hydrogel.

4.3.5.2. Preparation of polyacrylamide (PA) hydrogels

In preliminary work, the Protein A—N-cadherin complex could not anchor hiPSC-CMs on unfunctionalized polyacrylamide (PA) hydrogels (see section 4.2, Figure 4-7), so we employed oxidized N-Hydroxyethyl acrylamide (oHEA) to create a covalent bond between the hydrogel and the Protein A. We transferred the laminin and Protein A patterns to a ~10kPa oHEA-functionalized PA hydrogel before adding N-cadherin, to ensure that the final hydrogel presented the N-cadherin binding domain on the hydrogel surface.

We prepared the oHEA-functionalized PA hydrogels following a previously published protocol with some modifications [33]. Briefly, we began by oxidizing N-Hydroxyethyl acrylamide (HEA; Sigma, 697931) by adding 0.01 g of sodium metaperiodate (Sigma, 71859) to 2.338 mL of HEA, then incubating in the dark on a shaker for 4 hours. To adhere the PA hydrogels to the glass bottom dishes used in this work, we treated the glass with bind-silane. We prepared a solution with 95 µL of 100% ethanol, 50 µL of acetic acid, and 3µL of 3-(Trimethoxysilyl)propyl methacrylate (Bind-silane; Sigma, M6514). Then, we treated the glass with oxygen plasma for 30 seconds at 18W (Harrick, PDC-32G). Directly after plasma treating the glass, we added ~50 µL of the bind-silane solution to the glass surface. We incubated the solution on the glass for 1 minute, after which we removed the excess bind-silane solution. We left the remaining solution to react for 10 minutes, after which we rinsed the glass twice with 1 mL of 100% ethanol and dried with nitrogen gas.

To prepare the PA hydrogel solution, we combined 732 µL of 40% Acrylamide solution (Bio-Rad, 1610140) and 260 µL of 2% Bis-acrylamide solution (Bio-Rad,

1610142) with 4.008 mL MilliQ water. For experiments used in TFM analysis, we added 326μL of 1.0 μm-diameter blue fluorescent microbeads (ThermoFisher, F8814) and decreased the MilliQ volume to 3.682 mL to maintain the total volume of 5mL. Finally, we added 200μL of oxidized HEA, bringing the total volume to 5.2 mL. Separately, we prepared a 10% weight by volume (w/v) solution of ammonium persulfate (APS; Sigma, A9164) in MilliQ water.

To begin polymerization, we added 2.6 μL of N,N,N′,N′-tetramethylethylenediamine (TEMED; Sigma, 411019) and 260 μL of the 10% w/v APS solution to the PA solution. We gently mixed the solution with a P1000 pipette and then pipetted 35μL of the solution onto the bind-silane-treated glass surface. We then placed a protein patterned coverslip on top of the solution, sandwiching the PA solution between the bind-silane-treated glass and the protein patterned glass. After casting, the hydrogel polymerized in the dark for 30 minutes before we hydrated it with PBS and left it to fully polymerize at 4°C for 6-8 hours. After full polymerization, we removed and discarded the protein patterned top coverslip. A schematic of the protein transfer to oHEA-functionalized PA hydrogel can be seen in Figure 4-16b.

Following the removal of the top coverslip, we aspirated the PBS from the dish and incubated each PA hydrogel with ~50 μL of 100 μg/mL N-cadherin (R&D Systems, 1388-NC-050) for 3 hours at 4˚C. After 3 hours, we washed the PA hydrogel three times with 1mL PBS and then stored it overnight at 4°C in PBS with 10% Antibiotic-Antimycotic 100X (Anti-Anti; Gibco, ThermoFisher, 15-240-062) and 1% bovine serum albumin (BSA; ThermoFisher, PI37525). The following day, we

washed the hydrogel three times with 1 mL PBS and then stored it in PBS + 10% Anti-Anti until cell seeding. A schematic of the final device can be seen in Figure 4-16c.

We verified the patterning and the pattern transfer to PA hydrogel using green fluorescent laminin (as described in *Protein patterning glass coverslips*) and a pan-cadherin primary antibody (Sigma, C3678). We diluted the pan-cadherin antibody 1:200 in PBS and incubated on the devices for 1 hour at room temperature. We washed the devices three times with PBS and then incubated the devices with anti-rabbit AF-647 diluted 1:500 in PBS for 1 hour at room temperature. We rinsed the devices three times with PBS and then imaged (Figure 4-10a).

4.3.5.3. Stiffness characterization by Atomic Force Microscopy (AFM)

We characterized our PA hydrogel stiffness using AFM indentation based on a previously published protocol [35]. Briefly, we used a WITec AFM (Alpha300) and large tip cantilevers with tip radii of curvature (r_t) of 3.46 μm and 10 μm and nominal spring constants (k_c) of 0.191 N/m (3.46 μm tip – Bruker, SAA-HPI) and 0.184 N/m and 0.191 N/M (10 μm tip – Bruker, SAA-SPH-10UM and MLCT-SPH-10UM). We measured four hydrogels, assessing 3 locations per hydrogel with between 2-3 measurements per location. Each hydrogel was measured 2 days after polymerization.

The PA hydrogels were attached to a glass bottom dish and submerged in PBS. We measured Optical Lever Sensitivities [250] before each experiment by performing force-distance scans against the glass surface of a glass bottom plate using the following parameters: feedback control with 1.0 V set point, 1% p-gain,

and 0.2% i-gain, force-distance using 0.2 μm pull and 0.6 μm push at 0.2 μm/s speed.

After determining the Optical Lever Sensitivity, we loaded the PA hydrogel sample and centered the cantilever above a point on the hydrogel. We then approached the surface using the following parameters: 1.0 V set point, 1% p-gain, and 0.2% i-gain. We then performed the force-distance curve measurement using WITec's Distance Curve mode with approach and retract distances of 20 μm and 10 μm, respectively, at a speed of 3 μm/s. We analyzed the force-distance curves using the Hertz model [251], with the assumption that the PA hydrogel is linearly elastic.

4.3.5.4. Stem cell culture and cardiomyocyte differentiation

For this work, we used human induced pluripotent stem cell-derived cardiomyocytes (hiPSC-CMs). The hiPSCs were GFP-tagged alpha-actinin-2 (cell line 75) developed at the Allen Institute for Cell Science (allencell.org/cell-catalog) and available through Coriell (AICS-0075-085) [16, 20]. We cultured the hiPSCs on tissue culture plastic coated in Matrigel (Corning, 356252) using feeder-free culture conditions in standard conditions of 5% carbon dioxide at 37°C. The hiPSCs were cultured in Essential 8 Medium (Gibco, ThermoFisher, A1517001) which was changed daily. We passaged the cells with EDTA when confluency reached 75%. We differentiated the hiPSCs into cardiomyocytes (hiPSC-CMs) using a previously published protocol [218] and maintained the hiPSC-CMs until seeding in RPMI 1640 Medium (ThermoFisher, 11875119) with B-27 Supplement (B27; ThermoFisher,

17504044). We seeded the hiPSC-CMs on devices at a density of ~100,000 cells/cm^2 between day 24-30 and imaged 3-4 days after seeding (day 27-34).

4.3.5.5. Microscopy

We performed all microscopy with a Zeiss Axio Observer 7 inverted microscope with a high speed camera (Photometrics Prime 95b) and a water immersion 40X objective (Plan Apochromat, 1.2 NA). The microscope was equipped with an incubation chamber (PeCon) that maintained a temperature of 37°C and 5% CO_2 during live-cell imaging.

Before live-cell imaging, we changed the media from B27 to B-27 Supplement in RPMI 1640 Medium, no phenol red (ThermoFisher, 11835030) with 10mM HEPES and 1% Anti-Anti. For each cell, we took a still image in brightfield, 405 (fluorescent microbeads), 488 (alpha-actinin), and 546 (Protein A). We used the still images in the 546 channel to determine whether the cell was on a single- or dual-protein pattern. After the still images, we recorded ~10 second long videos of sarcomeres (488 channel) and fluorescent microbeads (405 channel). The frame rate was ~40 frames per second for the sarcomere videos and ~80 frames per second for the microbeads videos.

For the data presented in this work, unless otherwise noted, we included only cells that overlapped at least one N-cadherin cap in the dual protein datasets.

4.3.5.6. Sarcomere contractility quantification

We acquired sarcomere shortening videos using alpha-actinin-tagged hiPSC-CMs (as described in *Stem cell culture and cardiomyocyte differentiation)*. After collecting a video, we cropped it in FIJI (ImageJ) [220] and applied the “Subtract

Background" tool with a rolling ball radius of 5 pixels. We then adjusted the brightness and contrast in FIJI using the "auto" option and saved the video as an AVI with a 40 frames per second frame rate.

To quantify the average alignment, sarcomere length, sarcomere shortening, and radial contraction, we ran the videos through Sarc-Graph, a previously published, open-source code that segments the images and tracks sarcomere alignment and contraction [238].

4.3.5.7. Traction force microscopy

We utilized CONTRAX, a custom, open source workflow that acquires images and videos, then analyses fluorescent bead displacements using an Ncorr tracking module on pairwise frames from videos of beating hiPSC-CMs to generate matrices of spatiotemporal displacement field data [214, 239]. The traction force microscopy (TFM) module in CONTRAX uses the displacements to calculate traction stresses. The traction stresses are then integrated over the area of the cell to determine the total traction force produced by the cell [214].

We first uploaded bead displacement videos (~800 frames each) and their corresponding brightfield still images into CONTRAX. For each video, we drew the outline of the cell in FIJI using a composite image of the brightfield and 488 still images of the cell. We saved the cell outline as an ROI and loaded it into CONTRAX with the corresponding bead displacement video (Figure 4-17a). CONTRAX uses the cell outline to isolate the forces produced by the cell from background noise. The size of the area around the cell included in the analysis can be set using the "mask parameters" in CONTRAX.

Force production is calculated from bead displacements, so we can expect to see forces slightly outside of the cell outline due to the cell deforming the gel at the cell boundary, causing bead displacements outside the cell outline, as can be seen in Figure 4-17a.

To capture the forces at the cell boundary, while excluding background noise, we adjusted the “area factor” and “scale factor” in the “mask parameters” section of CONTRAX. After outlining the cell, CONTRAX calculates an ellipse that best fits the outline. The area included in the analysis is equal to the best fit ellipse times the “area factor”, so a larger “area factor” equals a larger analyzed area. The “scale factor” controls the aspect ratio of the analysis region ellipse, with a “scale factor” of greater than 1 increasing the aspect ratio and a “scale factor” of less than 1 decreasing the aspect ratio.

In this work, we chose an analysis region “area factor” of 3 and a “scale factor” of 0.75. The area factor of 3 allows us to capture the forces just outside the cell boundary as described above, while excluding much of the noise around the cell, as can be seen in Figure 8c. The “scale factor” of 0.75 ensures the analysis region stays within the frame, especially with long, thin cells.

After loading the cell outline, we input the material properties for the PA hydrogel the cell was on. For this study, all the cells were cultured on PA hydrogels with a Young’s modulus of ~6.8 kPa. The Poisson’s ratio for PA hydrogels is generally accepted to be between 0.45 and 0.5 [145, 252, 253], and in this work, we used a Poisson’s ratio of 0.45. These parameters are used in the force calculation with the assumption that the gel is linearly elastic and homogenous, which is a generally

accepted approximation when the strain on the hydrogel is very small (less than 1), as it is in TFM [253]. Additionally, we assume that the gel is thick enough and wide enough to prevent the cells from experiencing any boundary effects of the gel and that all cell-produced forces normal to the hydrogel surface are negligible. These assumptions are approximately true given that the hydrogel is ~10 times as thick as the cell height [254] and are generally accepted assumptions for traction force microscopy [253-255].

After the video initialization, we set the displacement parameters for the Ncorr displacement tracking module. We used a subset radius of 30 px, spacing coefficient of 10 px, cutoff norm of 1e-6, and cutoff iteration of 20. These parameters are used to optimize the bead tracking in Ncorr, minimizing the amplification of noise and the loss of information due to over-smoothing.

Using the resulting displacement maps at each timepoint (Figure 4-17b), CONTRAX calculates the regularization parameter, lambda, based on L-curve optimization [256]. The regularization parameter constrains the accepted force vectors, minimizing the error due to noise and the error due over-smoothing. Finally, using this regularization parameter, CONTRAX calculates the traction force heatmaps for each timepoint (Figure 4-17c) using Fourier Transform Traction Cytometry (FTTC) [241, 257].

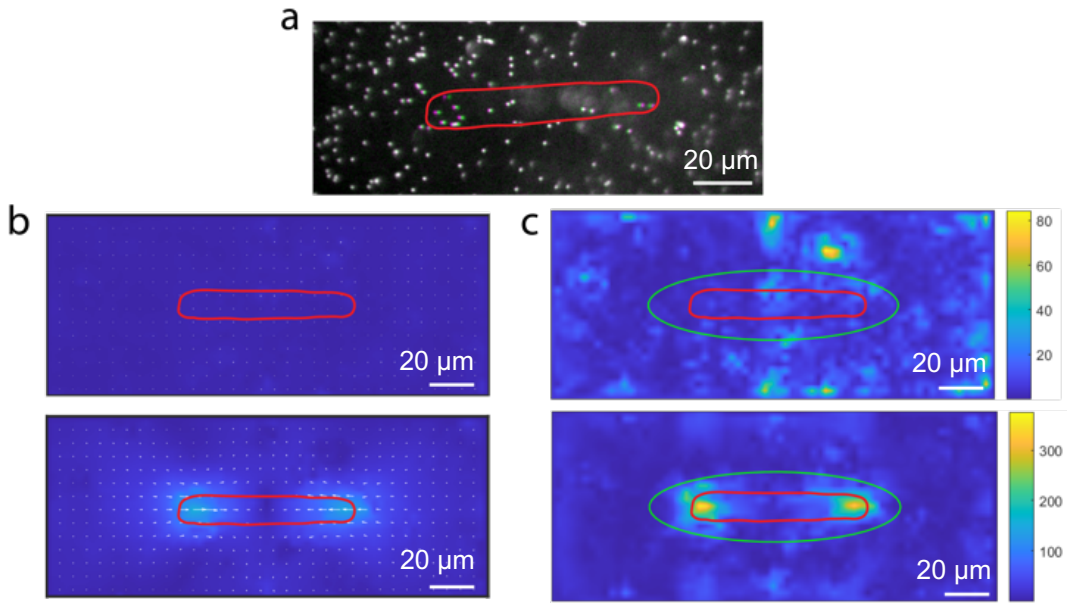

Figure 4-17. Intermediate steps of traction force microscopy. (a) Representative image of fluorescent microbeads when cell is fully relaxed (magenta) and fully contracted (green) state. Representative images of **(b)** displacement maps and **(c)** traction stress maps at relaxed (top) and contracted (bottom) states. Color bars in (c) are in units of Pascals. In all images, red elliptical shape is cell outline. In (c), green ellipse is the analysis region used by CONTRAX.

4.3.5.8. Cell fixation and immunostaining

Following live cell imaging, we fixed the hiPSC-CMs with 4% formaldehyde (ThermoFisher, 28908) for 10 minutes. Then we washed the cells with PBS three times and stored them in PBS at 4°C until immunostaining. Before antibody incubation, we incubated the cells for 5 minutes with a permeabilization solution of 0.1% Triton X-100 (ThermoFisher, A16046.AE) in PBS. We then incubated them with a blocking solution of 0.3% Tween20 (ThermoFisher, 28352) and 2% BSA in PBS for 30 minutes. We diluted a pan-cadherin primary antibody (Sigma, C3678) 1:200 in a solution of 0.1% Tween20 and 1% BSA in PBS (dilution buffer). We incubated the hiPSC-CMs with the pan-cadherin antibody solution for 1 hour at room temperature, then washed three times with dilution buffer. We diluted anti-

rabbit AF-647 secondary antibody (ThermoFisher, A-32733) 1:500 in dilution buffer and incubated on the cells for 1 hour at room temperature. We washed the cells three times with PBS and then stored in PBS at 4°C until imaging.

4.3.5.9. Statistics

Unless otherwise noted, we determined statistical significance of the data presented using parametric, unpaired, two-tailed T-tests. P-values with significance at $P<0.05$ are designated with (*), $P<0.005$ are designated with (**), $P<0.0005$ are designated with (***), and $P<0.0001$ are designated with (****). For all parametric T-tests, we verified Normality and Lognormality and transformed data as appropriate. For all T-tests, we also performed F-tests to check differences in variance between the two samples. Unless otherwise noted, all F-tests came back non-significant. For data with significant differences in variance, we reanalyzed the data with a Welch's correction to account for varying standard deviations. All statistical analyses were performed and visualized using Prism (GraphPad Software, Inc.).

5. Mimicking 3D CM Environment with Microwells

5.1. Background and Motivation

Patterning single hiPSC-CMs on two-dimensional rectangular patterns has been shown to improve hiPSC-CM structural and functional maturity [15, 31] (see Chapter 1 for more discussion). Two-dimensional patterning (2D) is useful and has improved the hiPSC-CM model, but it lacks the three-dimensional (3D) interactions with extracellular matrix (ECM) scaffolding present in native human heart tissue [17, 258]. Tissue-level studies, which inherently have these 3D interactions, are limited by the low availability of human tissues for studying (see Chapter 1 for more discussion). Some studies have addressed these limitations by creating 3D cardiac tissues, often called engineered heart tissues (EHTs) [43-47].

Eschenhagen and colleagues created some of the first EHTs by culturing embryonic chick cardiac myocytes in collagen scaffolding [44]. Boudou, et al. used microelectromechanical systems to create an array of 3D CM tissues in matrices with microcantilevers, allowing for real-time tracking of contractile force and frequency [43]. The study created a high-throughput method for creation and assessment of EHTs, but they used neonatal rat cardiomyocytes, limiting the scope of applications for studying the human heart [43]. With the development of multiple approaches for creating EHTs, along with the increased prevalence of hiPSC-CMs, more studies began making human EHTs [45-47]. Tulloch, et al. created EHTs with hiPSC-CMs and human embryonic stem cell-derived CMs to study the impact of mechanical loads on CM proliferation and hypertrophy [45]. Ronaldson-Bouchard, et al. made EHTs with hiPSC-CMs and found the tissues improved the hiPSC-CMs

maturity markers, including sarcomeric structure, force production, calcium handling, and t-tubule formation [46]. While the improvement of hiPSC-CM maturity and the ability to study hiPSC-CMs in these tissues was impressive, the complexity of the tissues means that the cells had to be fixed and sectioned to visualize subcellular structures [46]. These studies have provided great advancements to the field of human heart research, but the tissue-level complexity doesn't allow for the study of live-cell subcellular structure and function. Additionally, the control over variables provided by the single-cell model is lost in these EHT studies. In this work, we aimed to create a 3D microenvironment for single-cell hiPSC-CMs that allows for live-cell imaging of subcellular structures and reductionist studies of individual variables.

In previous work from the Pruitt lab, 3D microwells were created and used to pattern mouse myoblast cells [48]. The mouse myoblasts showed increased height, uniformity in shape, and greater actin alignment in the 3D microwells compared to those on 2D rectangular patterns [48]. In this work, we aimed to adapt this method to a human model, patterning hiPSC-CMs in 3D microwells. We hypothesized that the 3D, single-cell microenvironment would lead to improved cell morphology as well as increased sarcomeric organization and force production associated with improved hiPSC-CM maturity.

5.2. Methods

5.2.1. Creating PDMS microwell molds

Microwell molds were creating using a previously published protocol [48] with some modifications (Figure 5-1). Master molds were created via photolithography using SU-8 2010 (Microchem) photoresist on a silicon wafer. Once patterned, the wafer was silanized with trimethylsilyl chloride (TMCS; Sigma, 92361) for 1 hour to allow easy detachment of PDMS from the wafer. After silanization, we cast the thick mold by adding ~40g of Sylgard 184 PDMS (Dow, DC4019862) in a 10:1 ratio of base to curing agent and letting the PDMS cure at ~70°C for at least 8 hours. After curing, the PDMS was diced to create the thick molds and silanized again. For the thick mold silanization, we began by plasma treating the molds for ~1 minute at 18W (Harrick, PDC-32G). Then we silanized with TMCS overnight (~12 hours). After overnight silanization, the thick molds were left in the fume hood for 10 minutes and then baked for 30 minutes at ~70°C.

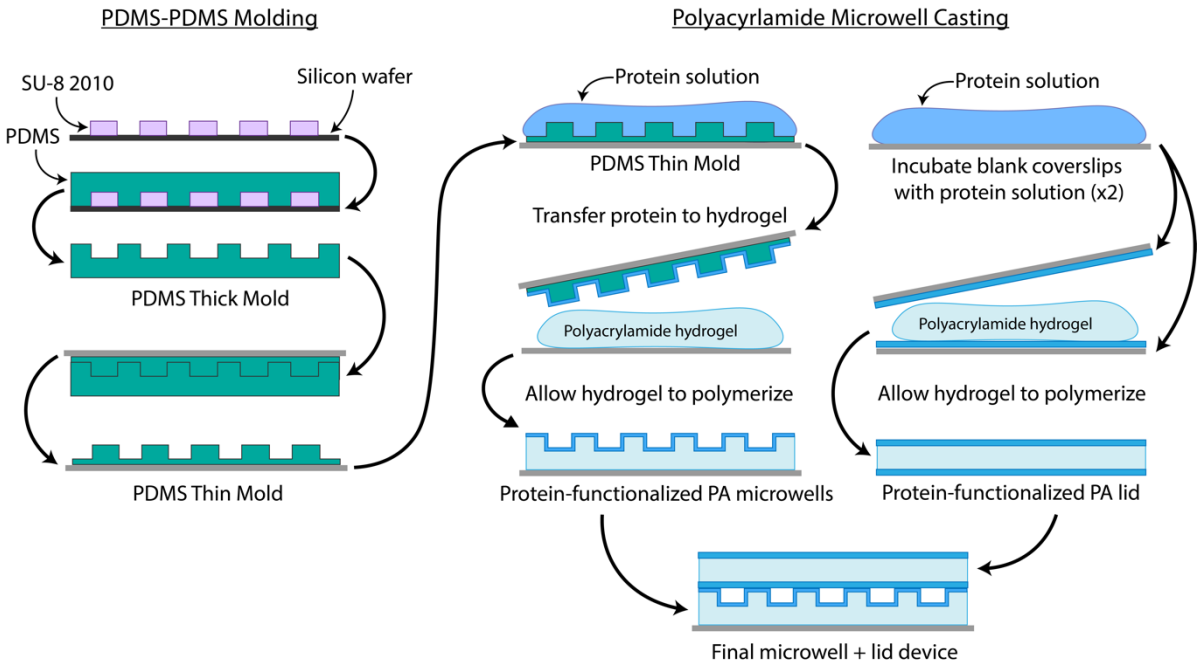

Figure 5-1. Process flow for microwell fabrication.

After the thick molds were silanized, we cast the thin molds. For a more detailed protocol for thin mold casting with images for each step, see Appendix A. First we attached the silanized thick mold, patterned side up, onto a 25x25x1mm glass slide. We wrapped another glass slide with foil and wrapped a piece of tape around the foil-covered glass with the sticky side facing outward. We placed a #2 22mm round coverslip (VWR, 48382-063) on the tape so that it was secure on the foil-covered glass slide. Finally, we added a ~3in-long piece of tape to the back of the foil-covered glass slide with the sticky side attached to the foil. After preparing the thick mold sandwiches, we mixed ~1g of PDMS in a 10:1 ratio of base to curing agent. We then applied a small droplet of the PDMS mixture, ~50-100µL, to the surface of the thick mold and placed the thick mold (still on the glass slide) on top of the coverslip attached to the foil-covered glass slide. The piece of tape was then used to secure the two glass slides together, with the thick mold and the uncured PDMS in between (Figure 5-2). Finally, this sandwich was placed into the PDMS oven, foil-covered glass facing up, and a 50g weight was added on top. These molds were baked for at least 4 hours at ~70°C then removed to cool before demolding. After cooling, the tape surrounding the sandwich was cut and the glass slide attached to the thick mold was removed by inserting a tweezer tip between the PDMS and glass. Then, we peeled the thick mold off of the thin PDMS mold slowly to prevent the glass coverslip from breaking. Next, the tape around the foil-covered glass slide was cut and the foil was unwrapped and the glass slide set aside. Finally, the coverslip with the thin mold was carefully peeled off of the tape and foil.

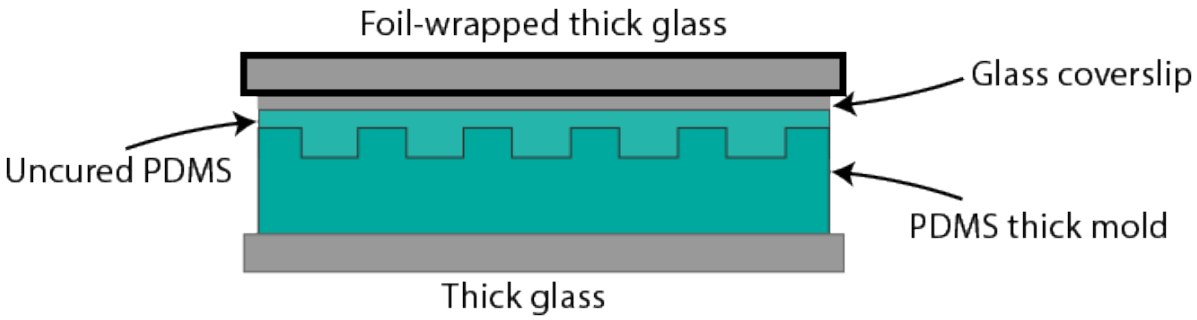

Figure 5-2. Schematic of sandwich used to make microwells thin mold.

Before casting polyacrylamide hydrogels on the thin PDMS molds, they were incubated with Matrigel diluted 1:10 in DMEM for 1 hour at room temperature. After an hour, the Matrigel solution was aspirated from the molds and the molds were dried with compressed nitrogen.

5.2.2. Microcontact printing

The 2D controls were made using microcontact printing, following a previously published protocol [29, 259]. Briefly, PDMS stamps were made by pouring PDMS (10:1) over a master mold. After baking, the PDMS was removed from the mold and cut into individual stamps. Stamps were incubated with Matrigel diluted 1:10 in DMEM for 1 hour at room temperature. After an hour, the Matrigel solution was aspirated from the stamps and the stamps were dried with compressed nitrogen. After drying, the stamps were placed patterned side down on top of a coverslip and a 50g weight was added on top of the stamp. The stamp and weight were left for 5 minutes, after which the coverslip was carefully removed from the stamp and set aside for the next step.

5.2.3. Polyacrylamide hydrogel fabrication

We followed a previously published protocol to prepare the PA hydrogels [35, 48]. To adhere the PA hydrogels to the glass bottom dishes used in this work, we treated the glass with bind-silane. For more details, see the methods section of Chapter 4. We used a PA formulation with higher crosslinker concentration to reduce swelling [48]. We combined 161μL of a 0.025g/mL N,N′-Methylenebis(acrylamide) (bis-acrylamide; Sigma, 146072) solution, 152μL of a 0.5g/mL acrylamide (Sigma, 01696) solution, 519.4μL of water, 140.5μL of 250mM N-2-hydroxyethylpiperazine-N-2-ethane sulfonic acid (HEPES; Thermo, 15630080), and 21.6μL of red fluorescent microbeads (diameter 0.5μm, Thermo, F8812). Separately, we prepared a 10% weight by volume (w/v) solution of ammonium persulfate (APS; Sigma, A9164) in MilliQ water. We degassed the PA precursor solution and the APS solution for 1 hour in a vacuum desiccator to remove bubbles.

The polymerization process was the same as that used in Chapter 4 but with the Matrigel-functionalized PDMS thin mold placed on top of the PA solution, sandwiching the solution between the mold and the bind-silane-treated glass. After casting, the hydrogels polymerized in the dark for 30 minutes before being hydrated with PBS and left to fully polymerize at 4°C for 6-8 hours. After full polymerization, the PDMS thin mold was removed and discarded and the hydrogels were stored in PBS with 10% Pen-Strep at 4°C until cell seeding.

5.2.4. Cell seeding

For this work, we used GFP-tagged alpha-actinin hiPSC-CMs. For more details on the hiPSCs and hiPSC-CM differentiation, see Chapter 4. Cells were seeded on devices at a density of ~70,000 cells/cm^2 between day 25-30 and imaged 3-4 days

after seeding (day 30-35). To begin seeding, we prepared replating media, previously described in Chapter 4. We lifted up the hiPSC-CMs using TrypLE 10X for 5-10 minutes at 37°C. After 5-10 minutes, we diluted the TrypLE 10X by adding 1mL of replating media. The solution was triturated to further lift up the cells and then collected in a 15mL conical tube containing 3mL of replating media to further dilute the TrypLE 10X. The 15mL conical tube was spun in a centrifuge at 200g for 3 to 5 minutes, until a pellet formed at the bottom of the tube. The supernatant was aspirated and the pellet was resuspended with 1mL of replating media. We stained a sample of the resuspended cells with Trypan Blue and counted cells on a hemocytometer to achieve the desired density of 250,000 cells per device. Then, we flooded the devices with the resuspended cell solution and centrifuged the entire plate, containing both 3D microwells and 2D stamped devices, at ~300g for 5 minutes. Following the second centrifugation, we left them in the incubator at 37°C for 1 hour. After 1 hour, the PA hydrogel lids were added and secured to the PA hydrogel device using a laser-cut holder described in previous work [48]. After adding the lids, the devices were put back in the incubator at 37°C for 48 hours. After 48 hours, we changed the media in the devices to B27 with 1% Pen-Strep every two days.

5.2.5. Confocal microscopy

All images were taken on a Leica SP8 Resonant Scanning confocal microscope with a 40X water immersion objective (1.1 NA, 650μm WD). Z-stacks were taken of each cell in the 488 channel to capture the sarcomere structure throughout the cell.

Sarcomere shortening videos were taken at the top, bottom, and middle of the cell with a frame rate of ~30 frames per second.

We acknowledge the use of the NRI-MCDB Microscopy Facility and the Resonant Scanning Confocal supported by the NSF MRI grant DBI-1625770.

5.3. Results

5.3.1. hiPSC-CMs Were Seeded in Single-cell 3D Microwells

To investigate the effect of the 3D microenvironment on hiPSC-CMs maturity, we isolated single hiPSC-CMs in 3D microwells. Two different microwell designs were used for this work. The first consisted of groups of three different area rectangles - 750μm^2, 1125μm^2, and 1500μm^2, all with an aspect ratio of 5:1 and height of ~10μm (Figure 5-3a). The second was uniform, with 1500μm^2 patterns with an aspect ratio of 7:1 and height of ~10μm (Figure 5-3b). The first design was used in previous work by the Pruitt lab that used microwells to encapsulate mouse myoblast cells [48]. The first experiments were done with this design for consistency. The second design was created to match the 2D patterns most commonly used in the Pruitt lab. The data presented in this chapter is from experiments using the second design only. Figure 5-3c shows a confocal image of a 15000μm^3, 7:1 microwell, where the red dots are fluorescent microbeads embedded in the gel and the green signal is 488-tagged gelatin (ThermoFisher, G13186) that the microwells were functionalized with for imaging purposes.

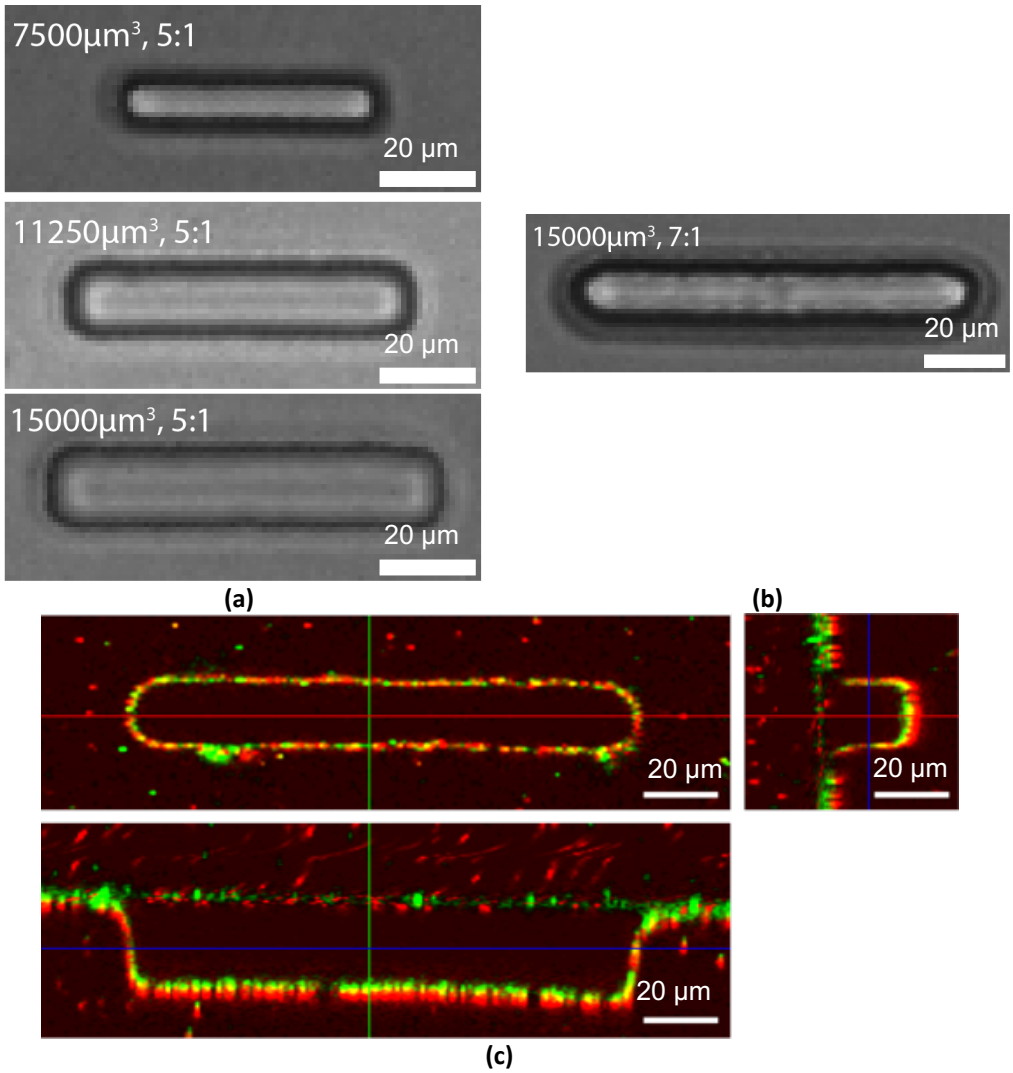

Figure 5-3. Visualization of microwell thin molds and PA hydrogel microwells. Brightfield images of PDMS thin molds of **(a)** the first microwell design with 5:1 wells with volumes of 750, 11250, and 15000µm^3 and **(b)** the second microwell design with 7:1 wells with 15,000µm^3 volume. **(c)** Fluorescent confocal image of second microwell design with 7:1 wells with 15,000µm^3 volume. Red shows fluorescent microbeads embedded in the PA hydrogel, green shows 488-tagged gelatin protein.

After creating the Matrigel-functionalized PA hydrogel microwells, we seeded hiPSC-CMs on the devices. In our first attempts, we seeded hiPSC-CMs using B27 + 1% Pen-Strep, with which we saw very poor attachment to the microwells To

improve hiPSC-CM attachment, we used replating media described in the methods of Chapter 4. In addition to using replating media, we also spun down the devices after seeding to encourage the hiPSC-CMs to go into the microwells, rather than staying on top of the device. With these adjustments, we were able to successfully seed hiPSC-CMs inside the microwells (Figure 5-4).

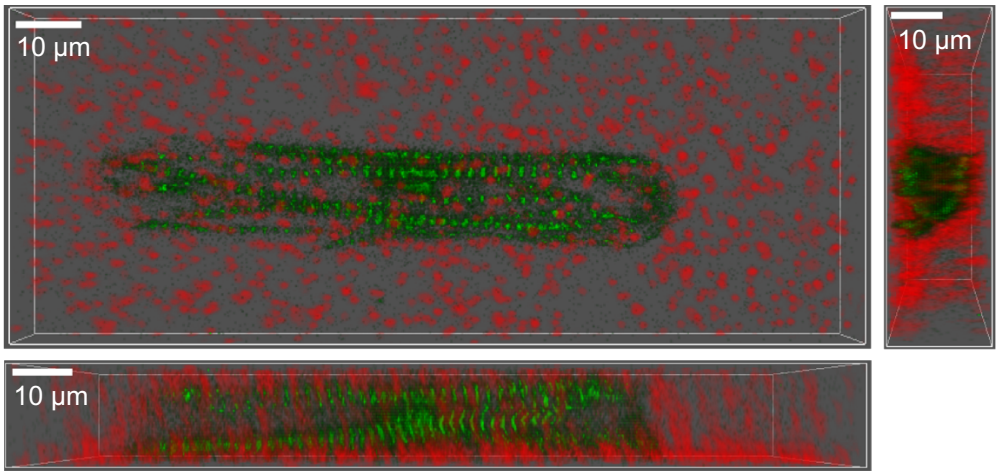

Figure 5-4. Confocal image of an α-actinin-tagged hiPSC-CM patterned in a 3D microwell. Sarcomeres are green and fluorescent microbeads are red.

While we were able to seed hiPSC-CMs in microwells, the process was low-throughput. For each device with thousands of microwells, we typically saw about 15 single hiPSC-CMs encapsulated in microwells. Very few microwells were filled with hiPSC-CMs and those that were often had multiple cells per well or attachment between the cell in the well and the cells on the top surface of the device, despite the lid in place. Additionally, after seeding, there was a small window of time in which the hiPSC-CMs were beating and happy before most of them died. This small window made it difficult to collect data from these devices, as the hiPSC-CMs often died before imaging was done.

5.3.2. Patterning hiPSC-CMs in 3D Microwells Improves Cell Morphology

5.3.2.1. Patterning hiPSC-CMs in 3D Microwells Does Not Affect Cell Volume

After seeding hiPSC-CMs on our microwell devices, we expected to see greater cell height and volume in the 3D-patterned hiPSC-CMs compared to the 2D-patterned controls, as was seen in previous work with C2C12 cells [48].

To estimate hiPSC-CM volume, we used an open-source machine learning image processing tool called ilastik [260] to determine the cell area for each frame of a z-stack. We did so by labeling what we considered part of the cell area (blue) and what was outside the cell (yellow) on training data and then processing the rest of the images (Figure 5-5a). After ilastik output the cell area estimates for each z-position (Figure 5-5b), the cell volume could be calculated by summing the area measured for each z-position.

For this process, we used the images of the sarcomeres to estimate cell volume. We chose the sarcomere images because the brightfield images had considerable out-of-plane signal, making it difficult to determine the cell boundary specific to each z-location. This is likely due to the pinhole being too wide, which could be adjusted in the future to solve this issue. The sarcomere images, while having little out-of-plane signal, are not ideal for area/volume measurements as the sarcomeres are not on the perimeter of the cell. Background fluorescence makes it easier to identify some areas of a cell that don't have sarcomeres, however we cannot be sure that the measurements are accurate without a cell membrane label or brightfield image.

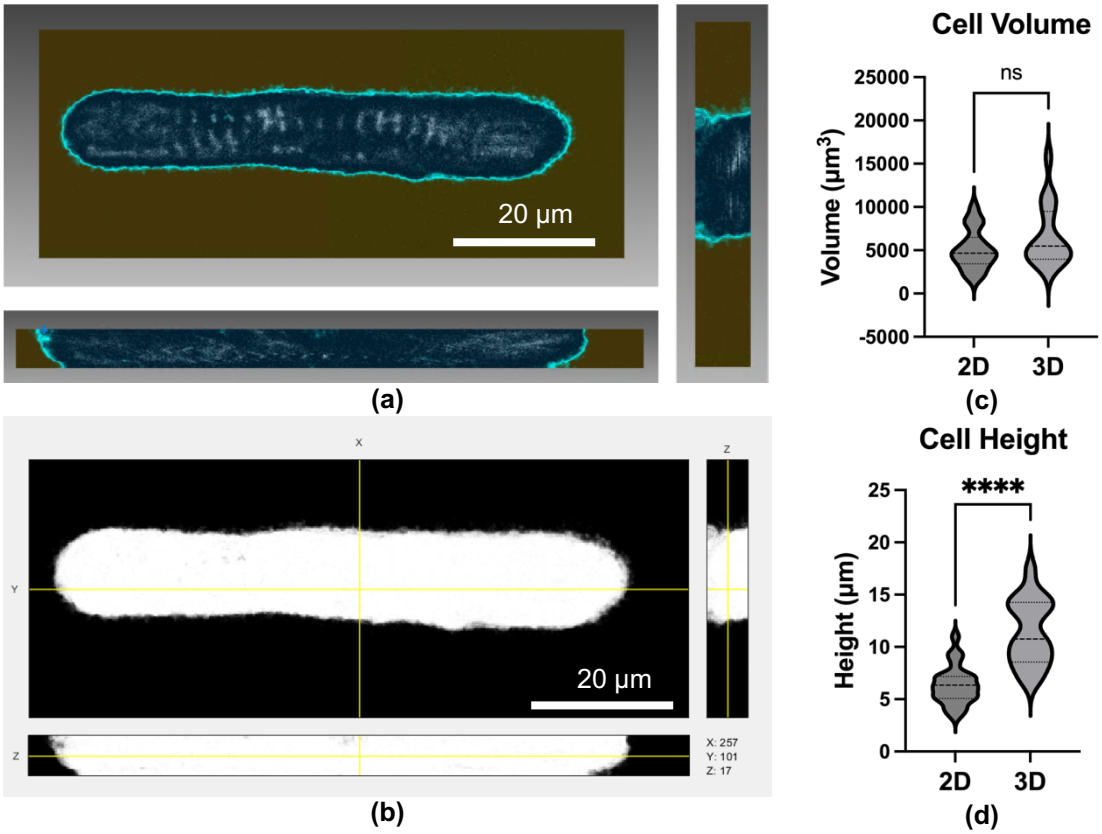

Figure 5-5. hiPSC-CMs patterned in 3D microwells have greater cell height but not greater cell volume compared to hiPSC-CMs patterned in 2D. **(a)** Ilastik segmentation of cell volume on an image of sarcomeres. The bright blue indicates the areas of uncertainty, the blue area represents what ilastik identifies as the cell, and the yellow represents the area outside of the cell. **(b)** The output of ilastik volume segmentation which can be used to estimate the total cell volume. **(c)** Cell volume for 2D- and 3D-patterned hiPSC-CMs. **(d)** Cell height for 2D- and 3D-patterned hiPSC-CMs. In (c) and (d), centerlines indicate medians, dotted lines indicate 25th and 75th percentiles.

Our results do not match our hypothesis, as there is not a significant difference between the volume of 2D- and 3D-patterned hiPSC-CMs (Figure 5-5c). This could be due to a number of factors, such as the error in the volume measurement method. It could also be due to the limited number of hiPSC-CMs in 3D microwells compared to those attached to 2D patterns.

As a more reliable proxy for volume, we estimated the height of the hiPSC-CMs using the sarcomere images. Again, using the sarcomere images to determine cell height introduces some error, but it is less than that of the volume measurement. For the height estimation, we measured the distance between the first and last z-planes with sarcomeric signal. Though the cell could extend beyond where the sarcomeres are, we expect that there is a relationship between the height of the overall cell and the height of the collective myofibrils.

We did see a difference in cell height for the 2D- and 3D-patterned hiPSC-CMs, confirming our hypothesis that the 3D microwells produce taller hiPSC-CMs. The average height of the 3D-patterned hiPSC-CMs was ~11.4μm, compared to ~6.3μm for 2D-patterned hiPSC-CMs (Figure 5-5d).

5.3.2.2. Patterning hiPSC-CMs in 3D Microwells Increases Cell Myofibrillar Content

To measure the total myofibrillar content in 3D- and 2D-patterned hiPSC-CMs, we again utilized ilastik. The sarcomere volume calculation from images of sarcomeres have less error than the volume estimations described above. Ilastik was more easily able to determine sarcomeres, as can be seen in Figure 5-6a,b. From ilastik's estimation of the sarcomeric area, we were able to calculate the total sarcomeric volume by summing the areas from each z-plane. As hypothesized, the 3D-patterned hiPSC-CMs had greater myofibrillar content, with a mean of 990μm^3, compared to a mean of 454μm^3 for the 2D-patterned hiPSC-CMs (Figure 5-6c).

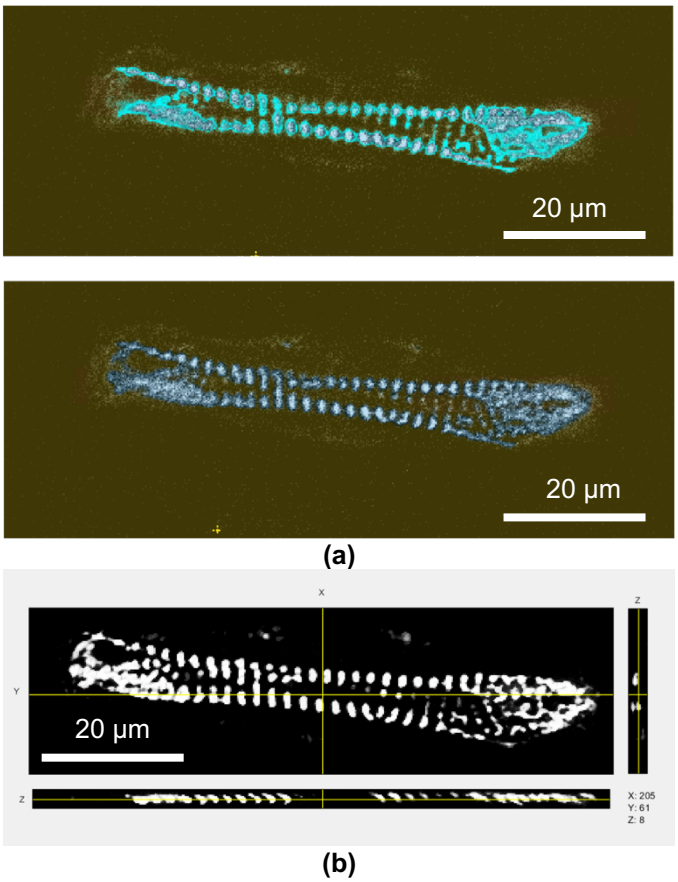

Figure 5-6. hiPSC-CMs patterned in 3D microwells have greater myofibrillar content than those patterned in 2D. **(a)** Ilastik segmentation of an image of sarcomeres. In the top image, the bright blue indicates the areas of uncertainty. In the bottom image, the whitish blue area represents what ilastik identifies as sarcomeres, while the yellow represents non-sarcomeric areas. **(b)** The output of ilastik segmentation which can be used to estimate the myofibrillar content. **(c)** The myofibrillar content in terms of volume - centerlines indicate medians, dotted lines indicate 25th and 75th percentiles.

The large range of myofibrillar content in 3D-patterned hiPSC-CMs compared to the smaller range in 2D-patterned hiPSC-CMs indicates greater variance in the cells in microwells than on 2D patterns. This could be due to the inconsistency in hiPSC-CMs patterned in 3D microwells and the relative consistency of 2D-patterned hiPSC-CMs.

5.3.2.3. Qualitative Observations of 3D- vs 2D-patterned hiPSC-CMs

Along with greater myofibrillar content, we also observed differences in sarcomere organization throughout the z-direction in 3D-patterned hiPSC-CMs. In 3D-patterned hiPSC-CMs, we saw varying sarcomere organization in different z-planes of a single cell (Figure 5-7). In 2D-patterned hiPSC-CMs, we saw only planar sarcomere organization, which is also reflected in the cell height measurements described above (Figure 5-5d). This greater complexity in sarcomere organization suggests a higher number of sarcomeres, which could indicate greater potential for force production.

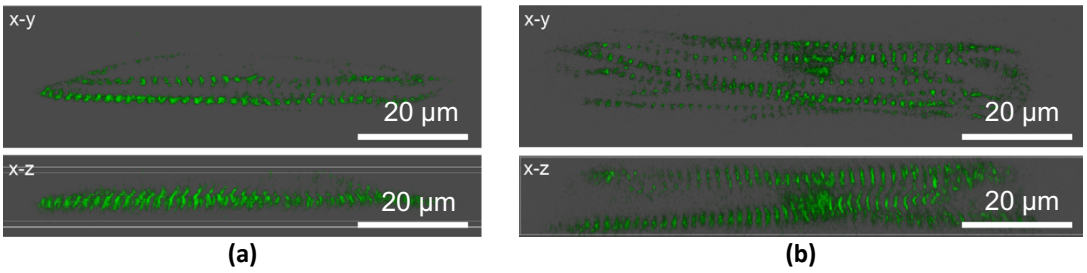

Figure 5-7. Sarcomeres organize along the z-axis in 3D-patterned hiPSC-CMs but are planar in 2D-patterned hiPSC-CMs. Fluorescent confocal image of α-actinin-tagged hiPSC-CMs patterned in **(a)** 2D and **(b)** 3D. Sarcomeres are in green.

Though we observed these differences, we were unable to quantitatively describe the differences, as the confocal z-stacks were not compatible with any of the sarcomere organization analysis tools we have used.

5.4. Conclusions

In this study, we have shown that we can pattern hiPSC-CMs in single-cell, 3D microwells. We found that the 3D microwells led to hiPSC-CMs with greater height but not greater volume, matching some of the results seen in the previous study of 3D microwells with mouse myoblast cells. The lack of difference in volume is likely

due to the low number of cells patterned in microwells and the variability of the cells that were successfully patterned. With no difference between hiPSC-CM volume, the increase in myofibrillar content in 3D-patterned hiPSC-CMs compared to 2D-patterned is even more pronounced. This increase in sarcomeres in 3D-patterned hiPSC-CMs suggests greater maturity of the hiPSC-CMs, as we expected. We also qualitatively saw that hiPSC-CMs patterned in 3D microwells had sarcomere organization that varied along the z-axis, as opposed to 2D patterned hiPSC-CMs that had planar sarcomere organization. These results indicate that 3D-patterned hiPSC-CMs could be an improved human CM model compared to 2D-patterned hiPSC-CMs.

In addition to cell morphology, parameters such as force production and sarcomere organization and contraction would be useful for assessing the maturity of 3D-patterned hiPSC-CMs. However, these parameters are difficult to assess with the data we collected here. For force production, most of our current tools are designed for 2D systems, and do not work without assuming forces are produced in only two dimensions. Traction force microscopy has been done in 3D, but this is more complex, both experimentally and computationally [261-264]. Future studies on applying TFM to 3D-patterned hiPSC-CMs could be greatly beneficial to this work. As with force production, many of the tools used to assess sarcomere organization and contractility are designed primarily for 2D systems. Images from a confocal microscope, with signal limited to a specific z-plane, do not work with these tools. Additionally, not many tools are able to analyze sarcomere organization outside of an x-y plane. Future work in adjusting the available tools to work with

confocal data and organization along the z-axis would be advantageous for this platform.

While 3D microwells replicate the 3D microenvironment of the heart and possibly improve the hiPSC-CM model, there are challenges that make 3D microwells difficult to implement. The low throughput nature of the devices and the difficulties analyzing hiPSC-CMs on the devices make them less practical as tools for high volume studies. Future work should seek to improve the efficiency of hiPSC-CM seeding on 3D microwells and work towards adapting tools for analysis of 3D-patterned hiPSC-CMs.

6. Conclusions and Future Directions

6.1. Wafer-Scale Protein Patterning to Scale Up Lift-off

We developed a method for increased yield of glass templates for lift-off protein patterning. Our method produces up to 16 times the amount of pattern templates for a similar amount of work, increasing the availability and ease of use of lift-off protein patterning, a highly accurate and reproducible method for protein patterning. We showed that our pattern templates were compatible with PA hydrogel protein transfer and hiPSC-CM culture.

This work improves the yield of the lift-off protein patterning method, which could expand the use of the technique. With greater yield, labs with photolithography abilities can make and share pattern templates with labs that do not have experience with or facilities for microfabrication, as many groups already do with microcontact printing master wafers. These advancements could make the lift-off method more of a standard in the hiPSC-CM field. The higher accuracy of the patterns allows for more reproducible patterning of hiPSC-CMs – with wide-spread use in the hiPSC-CM field, this method could greatly improve the single-cell, patterned hiPSC-CM model.

6.2. Dual-Protein Patterned PA Hydrogels to Replicate Cell-Cell Interactions for hiPSC-CMs

We developed a method for spatially accurate dual-protein patterning compatible with transfer to polyacrylamide hydrogels and cultured hiPSC-CMs on the resulting devices. Our method is consistent, highly reproducible, and applies a novel dual

patterning method to functional cellular studies. We have demonstrated the use of the method by making dual protein patterns to mimic cell-cell interactions for single-cell hiPSC-CMs. Our results indicate that our reductionist model to mimic CM-CM junctions slightly improves hiPSC-CM structural and functional maturity, but fails to make significant changes in many crucial CM maturity markers. We conclude that the lack of significant difference in force production, overall sarcomere contractility, and sarcomere organization in single- and dual-protein patterned hiPSC-CMs indicates that N-cadherin caps are not sufficient to mimic cell-cell interactions between neighboring CMs.

Our ultimate goal was to determine if interaction with N-cadherin is sufficient to replicate cell-cell contacts for hiPSC-CMs, with the hypothesis that replicating cell-cell interactions would improve the maturity of the hiPSC-CMs. Our findings, which indicate that N-cadherin is not sufficient to replicate cell-cell contacts, are useful for future studies of reductionist hiPSC-CM models. It would be useful to do further studies to determine the intracellular response to the dual-protein patterns with N-cadherin caps. Vinculin, a protein associated with the intracellular signaling pathway of N-cadherin, would be a good target to study – determining if vinculin is present in hiPSC-CMs patterned on dual-protein patterns could indicate whether the signaling cascade associated with N-cadherin attachment is actually activated by hiPSC-CM attachment to dual-protein patterns.

In addition to determining the intracellular response of hiPSC-CMs to the N-cadherin caps on the dual-protein patterns, it would be useful to do further studies patterning alternative proteins associated with CM-CM junctions. One target to

replicate desmosomes is desmocollin, a cadherin-family protein key in desmosome function [245]. Creating protein patterns with N-cadherin and desmocollin could create a more accurate model of a CM-CM junction.

We have shown that the dual protein patterns improve our single-cell hiPSC-CM model by increasing cell area and cell attachment, as well as slightly improving sarcomere contractility. These moderate improvements suggest that more complexity is necessary to replicate cell-cell contacts for patterned single-cell hiPSC-CMs. The small improvements are promising indications that successfully mimicking cell-cell contacts for single-cell hiPSC-CMs could further enhance their maturity, improving the hiPSC-CM model for future studies of the heart.

6.3. 3D Microwells to Replicate a 3D Microenvironment for hiPSC-CMs

We adapted a method for single-cell 3D encapsulation to work with hiPSC-CMs. We have shown that we can pattern hiPSC-CMs in these 3D microwells and that hiPSC-CMs have greater cell height in the microwells compared to on 2D protein patterns. While we found that hiPSC-CMs in microwells have increased height comparted to hiPSC-CMs on 2D patterns, we did not see a significant difference between cell volume. While there was no difference in volume between hiPSC-CMs on 2D patterns and in 3D microwells, there was a difference in myofibrillar content, indicating that those hiPSC-CMs that survived in the microwells showed improved maturity, as we expected.

The lack of difference in cell volume of hiPSC-CMs patterned on 2D patterns vs in 3D microwells reflects the difficulties in getting viable, single hiPSC-CMs in

microwells. The yield from each experiment was very low, with only about 10 single cells in microwells on each device, compared to over 1000 microwells per device. This is one of the major aspects for future improvement – improving viability for single hiPSC-CMs in 3D microwells. One potential reason for the low viability of hiPSC-CMs in 3D microwells could be nutrient transfer through PA hydrogel. Unlike the 2D patterned hiPSC-CMs, cells in 3D microwells are completely surrounded by PA hydrogel, making the diffusion rate of nutrients through the PA hydrogel incredibly important for hiPSC-CM viability. With some hiPSC-CMs surviving, it is likely that there is some nutrient diffusion through the PA hydrogels, but the low number of hiPSC-CMs indicates it might not be enough for most hiPSC-CMs to survive. Potential approaches for improving this could include attempting to adjust the PA hydrogel formulation to increase pore size, potentially allowing for greater diffusion of nutrients from media. Another potential approach to improving the nutrient concentration in the microwells could be to increase the concentration of nutrients in the media.

In addition to difficulties in culturing viable, single hiPSC-CMs in microwells, there are also difficulties associated with analyzing the sarcomere organization and contractility and force production of hiPSC-CMs in 3D microwells. Many of the currently available and widely used tools for analyzing sarcomere organization and contraction are designed for 2D-patterned hiPSC-CMs. Analyzing sarcomeres that are organized in 3D, with variation along the z-axis, is not compatible with the sarcomere analysis software used in this work. The Allen Institute Cell Segmenter [265] software is a good candidate for this analysis, as it is designed to work with

confocal z-stacks. While there are available tools for 3D TFM, it is much more experimentally and computationally complex than 2D TFM [261-264]. Future work should determine if the available tools are compatible with single-cell 3D analysis, otherwise, new tools would have to be developed.

In addition to limitations in analyzing sarcomere organization and force production, sarcomere contractility analysis software requires high frame-rate videos with high signal-to-noise ratio. These requirements make it difficult to use data taken on a confocal microscope, which is necessary to capture variance in sarcomere organization along the z-axis. In this work, I was able to take sarcomere contractility videos either at a high frame rate, but with low signal-to-noise ratio, or at a low frame rate, with moderate signal-to-noise ratio. Future work is necessary to find the right balance of frame rate and signal-to-noise ratio, and/or a higher resolution or higher speed confocal microscope, in order to capture varying sarcomere contractility along the z-axis in videos that can be analyzed by the tools available today.

While 3D microwells replicate the 3D microenvironment of the heart and possibly improve the hiPSC-CM model, there are challenges that make 3D microwells difficult to implement. The low throughput nature of the devices and the difficulties analyzing hiPSC-CMs on the devices make them less practical as tools for high volume studies. Future work should seek to improve the efficiency of hiPSC-CM seeding on 3D microwells and work towards adapting tools for analysis of 3D-patterned hiPSC-CMs.

6.4. Summary of Potential Future Directions

The platforms we developed in this work move the hiPSC-CM field forward in improving the single-cell hiPSC-CM model by imitating cell-cell and cell-ECM interactions and by creating a 3D microenvironment. Here, we summarize potential future directions for development and improvement of these platforms and studies of single-cell hiPSC-CMs.

Platform development:

Dual protein patterning:

- Testing alternative proteins for end cap patterns – e.g. desmocollin
- Increasing complexity of protein patterning – e.g. multi-protein end caps

Microwells:

- Testing alternative PA hydrogel formulations to increase pore size
- Improvement of microwell lid attachment to minimize hiPSC-CMs on top of microwells
- Creating microwells with multiple proteins (dual protein patterns in 3D)

hiPSC-CM studies:

Dual protein patterning:

- Watching and recording hiPSC-CMs as they attach to single- and dual-protein patterns
- Characterization of intracellular response to N-cadherin patterns
- Testing dual protein patterns with HCM mutant hiPSC-CM lines

Microwells:

- Optimizing data collection for sarcomere contractility analysis

- Finding/developing program for 3D TFM of single-cell hiPSC-CMs
- Testing microwells with HCM mutant hiPSC-CM lines

Appendix

Appendix A – Oxidized HEA (oHEA) Polyacrylamide Hydrogel Protocol[1]

<u>Step 1:</u> Oxidation of HEA (needs to be freshly prepared!)

- Sodium Metaperiodate
  - Form: solid/powder
  - MW: 213.89 g/mol
- N-Hydroxyethyl acrylamide (HEA)
  - Form: liquid

*collect waste from Sodium Metaperiodate and HEA in HEA waste bucket

1. Oxidize HEA by adding 0.02 M sodium metaperiodate
   a. Ex.: 0.01 g of Sodium Metaperiodate in 2.338 mL of HEA
2. Incubate HEA and Sodium Metaperiodate mixture at room temperature under dark conditions and continuously shaking for 4 hours to facilitate free aldehydes generation in HEA

<u>Step 2:</u> Treat bottom coverslips with Bind-Silane

1. Mix 950 µL Ethanol, 50 µL Acetic Acid, & 3 µL Bind-Silane (3-(Trimethoxysilyl)propyl methacrylate) in a plastic tube
   a. Carefully mix by triturating with a 1000 µL pipette
2. Plasma treat cleaned coverslips for 15 seconds on high power
3. Pipette the bind-silane solution onto each coverslip
   a. ~30 µL for 18mm coverslip
   b. ~100 µL for glass-bottom 6-well plate
   c. Increase/decrease volume as necessary for your glass area
4. Allow the solution to react for 1 minute
5. Remove excess Bind-Silane by dabbing on clean KimWipe
6. Allow the solution to react for 10 minutes
7. Rinse twice with 1 mL of Ethanol
8. Carefully dry with N2 gas
9. Place in the bind-silane degasser and degas until ready for use

<u>Step 3:</u> Prepare the precursors

1. Label 1.5 mL and 15 mL plastic tubes
   a. 1.5 mL for APS, 15 mL for precursors
2. Add MilliQ, Bisacrylamide, Acrylamide, and fluorescent beads (straight from the tube), into 15 mL tube (see table below for volumes)
   a. Carefully triturate with a 1000 µL pipette
3. Make a 10% w/v APS solution
   a. Ex: weigh 0.060 g of powder and add 600 µL of MilliQ water

[1] This protocol was developed in collaboration with Erica Castillo

b. Triturate with a 1000 µL pipette to mix
4. Add 200 µL of the freshly prepared oxidized HEA to PA precursor solution

Formulation	Bis-acrylamide (2%)	Acrylamide (40%)	Fluorescent Beads	MilliQ Water
Sarker paper (reported ~7kPa, measured ~25kPa)	362.5µL	1500µL	108.5µL	3029µL
10%T, 1%C (calc ~6kPa, measured ~6kPa)	260µL	732µL	108.5µL	3899µL

<u>Step 4:</u> Polymerize the PA

1. Wipe down benchtop with 70% Ethanol
2. Remove Bind-Silane coverslips/plates from degasser and place on benchtop (Bind-Silane treated side facing up)
3. Rinse top coverslips if incubating with protein
4. Dry the top coverslips

Be quick about the process from the addition of TEMED onward!

5. Add 2.6 µL of TEMED and 260 µL of APS (0.5% final APS concentration and 0.05% final TEMED concentration)
6. Slowly (to avoid bubble introduction) mix 3-4 times with a 1 mL pipet
7. **Pipette 40 µL precursor solution** onto each Bind-Silane-treated coverslip
    a. **Note:** Volume of solution depends on the height you desire for the gel and the size of your top coverslip. Ex: for 18mm coverslip, 50 µL gel solution creates gel ~200 µm in height
8. Quickly and carefully place the top coverslips on the gels before they polymerize
9. Let the gels sit for 45 minutes in the dark while they polymerize
10. Place the polymerized gels in PBS with 5% pen strep and store at 4°C
11. Flush all gel components with N2 and wrap with parafilm

<u>Step 5:</u> Block with BSA

1. Pop off the top coverslip of the gel
2. Wash 3 times with PBS
3. Passivate unpatterned regions with BSA (1% by volume) overnight at 4°C
    a. Flood the well with PBS + 1% BSA
4. Aspirate BSA and wash hydrogels 3 times with PBS
5. Place gels in PBS with 5% pen strep and proceed to seed devices with cells

Appendix B – AFM Characterization of Polyacrylamide Hydrogels

B-1. Pruitt Lab Reagents

Polyacrylamide hydrogels made with the following reagents:

	Acrylamide	Bis-acrylamide	HEPES
Concentration (diluted in MilliQ)	0.5 g/mL	0.025 g/mL	250 mM
Supplier, product number	Sigma, 01696	Sigma, 146072	Thermo, 15630080

Recipes for the formulations tested:

	Acrylamide (0.5 g/mL)	Bis-acrylamide (0.025 g/mL)	HEPES (250 mM)	MilliQ Water
10% T, 1%C (expected ~6kPa)	198µL	40µL	140.5µL	616µL
8% T, 5% C (expected ~10kPa)	152µL	161µL	140.5µL	541µL
20% C, 0.2% C (expected ~10kPa)	400µL	16µL	140.5µL	438µL
10% T, 2% C (expected ~14kPa)	196µL	80µL	140.5µL	578µL
15% T, 1% C (expected ~32kPa)	297µL	61µL	140.5µL	496µL
20% T, 3% C (expected ~100kPa)	392µL	161µL	140.5µL	301µm

*note for measurements with beads, the only change to the recipe is adding 21.6µL of beads solution

AFM measurement results:

	10% T, 1%C (expected ~6kPa)				
Date of Measurement	**8/17/20**	**8/19/20**	**9/17/20**	**9/23/20**	**4/26/21**
Gel age	6 days old	1 day old	1 day old	1 day old	3 days old
Made by	Orlando Chirikian	Orlando Chirikian	Cheavar Blair	Kerry Lane	Kerry Lane
Average Stiffness (kPa)	8.0	6.0	5.6	7.8	9.5
St. Dev (kPa)	1.7	0.8	0.7	1.5	0.6

From all measurements of 10% T, 1% C gels, the average stiffness is 7.1kPa with a standard deviation of 3.1kPa. Excluding the data from 8/17/20 (because the gels were 6 days old) the average stiffness is 7.1kPa with a standard deviation of 2.9kPa.

	8%T, 5%C (expected ~10kPa)	**20%T, 0.2%C** (expected ~10kPa)		**10%T, 2%C** (expected ~14kPa)
Date	**4/26/21**	**8/19/20** (w/ fluorescent microbeads)	**8/19/20** (w/o fluorescent microbeads)	**8/17/20**

Gel age	3 days old	1 day old	1 day old	6 days old
Made by	Kerry Lane	Orlando Chirikian	Orlando Chirikian	Orlando Chirikian
Average (kPa)	12.9	10.8	6.6	13.0
St. Dev (kPa)	5.2	1.0	0.9	0.4

	15%T 1%C (expected ~32kPa)		**20%T, 3%C** (expected ~100kPa)	
Date	**8/17/20**	**8/19/20** (w/ fluorescent microbeads)	**8/17/20**	**8/19/20** (w/ fluorescent microbeads)
Gel age	6 days old	1 day old	6 days old	1 day old
Made by	Orlando Chirikian	Orlando Chirikian	Orlando Chirikian	Orlando Chirikian
Average (kPa)	22.0	20.0	73.0	91.6
St. Dev (kPa)	3.9	1.2	10.9	22.9

B-2. oHEA PA hydrogels with Bio-Rad Reagents

Polyacrylamide hydrogels made with the following reagents:

	Acrylamide – 40% solution	**Bis-acrylamide – 2% solution**	**oHEA**
Supplier, product number	Bio-Rad, 1610140	Bio-Rad, 1610142	(see Ch 4 methods)

Recipes for the formulations tested:

	Acrylamide – 40% solution	**Bis-acrylamide – 2% solution**	**MilliQ Water**	**oHEA**
Sarker paper (reported ~7kPa)	1500µL	362.5µL	3137.5µL	200µL
BioRad 10%T, 1%C (expected ~6kPa)	732µL	260µL	4008.5µL	200µL
BioRad 15%T, 1%C (expected ~32kPa)	1375µL	390µL	3235µL	200µL
BioRad 15%T, 4%C (expected ~69kPa)	1316.5µL	1560µL	2123.5µL	200µL

AFM measurement results:

	Sarker paper (reported ~7kPa)			
Date of Measurement	**Gel age**	**Made by**	**Average Stiffness (kPa)**	**St. Dev (kPa)**
10/23/20	2 days old	Erica Castillo	29.6	2.0
4/26/21	3 days old	Kerry Lane	27.4	1.3
11/13/21	2 days old	Kerry Lane	17.6	1.4
10/28/20	6 days old	Erica Castillo	20.4	1.8
10/29/20	7 days old	Erica Castillo	19.1	1.7

From all measurements of Sarker paper gels, the average stiffness is 22.5kPa with a standard deviation of 5.4kPa. Excluding the data from 10/28/20 and 10/29/20 (because the gels were 6 and 7 days old), the average stiffness is 24.1kPa with a standard deviation of 6.0kPa.

	BioRad 10%T, 1%C (expected ~6kPa)			
Date of Measurement	**Gel age**	**Made by**	**Average Stiffness (kPa)**	**St. Dev (kPa)**
9/23/20	1 day old	Erica Castillo	6.6	1.7
11/13/21	2 days old	Kerry Lane	6.8	0.9
2/18/22	2 days old	Daniella Walter	7.3	0.3
10/28/20	6 days old	Erica Castillo	8.0	1.6
10/29/20	7 days old	Erica Castillo	9.1	2.6
2/24/22 (normal HEA oxidation)	1 day old	Kerry Lane	7.1	0.3
2/24/22 (overnight HEA oxidation)	1 day old	Kerry Lane	7.8	0.3

From all measurements of BioRad 10%T, 1%C gels, the average stiffness is 7.3kPa with a standard deviation of 1.7kPa. Excluding the data from 10/28/20 and 10/29/20 (because the gels were 6 and 7 days old), along with the overnight HEA oxidation data from 2/24/22, the average stiffness is 6.8kPa with a standard deviation of 1.5kPa.

	BioRad 15%T 1%C (expected ~32kPa)	**BioRad 15%T 4%C** (expected ~69kPa)
Date	**2/18/22**	**2/18/22**
Gel age	2 days old	2 days old
Made by	Daniella Walter	Daniella Walter
Average (kPa)	18.5	81.1
St. Dev (kPa)	0.7	4.2

Appendix C – PDMS-PDMS Molding Protocol[2]

There are two items we need to mold PDMS from PDMS - thick and thin molds. This molding process involves three main steps: pouring the bulk PDMS mold, silanizing the bulk PDMS mold, and molding the thin PDMS mold.

Materials:

- SU-8 wafer with 3D microwell patterns
- PDMS (Sylgard 184)
- 25x25x1mm glass slides (can cut from glass slides using glass cutter)
- Scotch tape
- No.2 18mm coverslips
- 50g weights

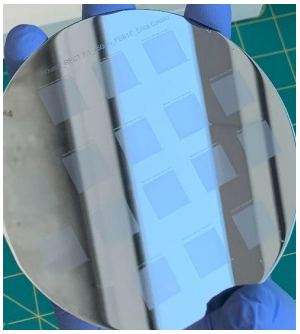

SU-8 wafer with 3D microwell patterns

Thick PDMS molds:

1. Mix 20 g Sylgard 184 (PDMS) base + 4 g curing agent and degas.
2. Pour PDMS on the microwell wafer in a foil boat, degas, and bake at 60°C for at least 4 hrs.
3. Remove PDMS from the oven, allow to cool, then carefully peel PDMS from the wafer.
4. Dice PDMS into individual microwell thick molds with a razor blade.

PDMS removed from wafer

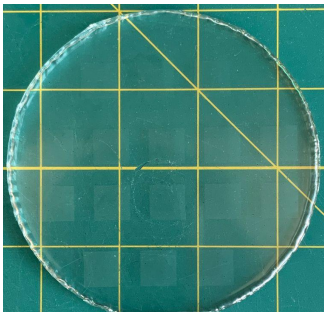

PDMS diced into individual thick molds

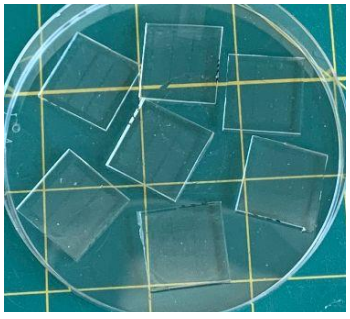

Silane Treatment: see Appendix D

Thin PDMS molds:

1. Mix 1 g PDMS base + 0.1 g curing agent and degas for 5-10 minutes.

---

[2] This protocol was adapted from a PDMS-PDMS molding protocol developed by Dr. Robin Wilson

2. Place each silanized PDMS mold on a 25x25x1mm glass slide (pattern side up). This glass slide will be referred to as glass slide 1.

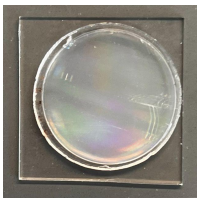

3. Wrap 25 x 25 x 1mm glass slides in foil to be placed on top of each mold, being careful to keep the foil flat and unwrinkled.

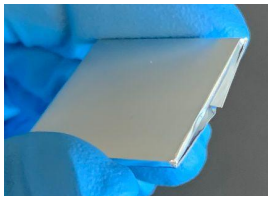

4. Wrap tape around the foil-covered 25x25x1mm glass slides so that the sticky side of the tape is facing up.

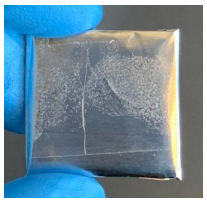

5. Place a No.2 22mm coverslip on top of the tape so that it is secure on the foil-covered glass slide.

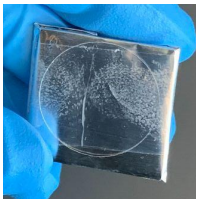

6. Put a piece of scotch tape (~3 in long) on the back of the foil-covered glass slide (sticky side facing the foil-wrapped glass).

7. Apply a small droplet of PDMS (50-100 µL) in the middle of the silanized bulk PDMS mold using a wood rod or pipet tip.

8. Flip the PDMS stack onto the foil-covered glass slide such that the coverslip is touching the uncured PDMS.

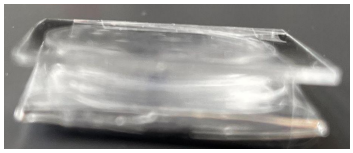

    a. Wrap the tape to secure the assembly.

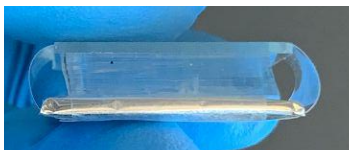

b. Place the assemblies with foil-covered glass on top in a 60°C oven and put a 50 g weight on top of each assembly to ensure a thin microwell mold.

c. Bake for at least 3 hrs.

9. Once baked, remove from oven, cool, then remove thin PDMS molds.
    a. First, cut the tape surrounding the glass slide sandwich.
    b. Then, remove uncovered glass slide by carefully inserting a tweezer between the thick PDMS and glass and slowly moving until the glass comes off.
    c. Next, peel off the silanized bulk PDMS mold.
    d. Cut the tape surrounding the foil-covered glass slide.
    e. Unwrap foil-covered glass slide, setting the glass aside.
    f. Carefully, peel the tape back from the coverslip to reveal the final thin PDMS microwell mold.

Appendix D – Protocol for Silanization of PDMS Molds[3]

Step 1: Plasma activate the microwell bulk molds for (30 W for 45 – 60 seconds)

Step 2: Immediately silanize the microwell bulk molds with TCMS

Setup:

1. Load molds into vacuum chamber
2. Turn the selector valve to the **OFF** position (pointed up)
3. Make sure the isolation and silane valves are **OFF** (horizontal)
4. Turn the vacuum pump on
5. Open (CCW) the fume hood Nitrogen valve 1-2 turns

Test Vacuum:

6. Turn the selector valve to **VACUUM** until pressure is about -25 inches Hg then turn the selector valve to **OFF**
7. Wait 1-2 minutes; vacuum should not change. If the vacuum does drop there is a leak in the system

Purge Chamber:

8. Turn the isolation valve **ON** (vertical)
9. Turn selector valve to **NITROGEN** until gauge pressure reads about 2 inches Hg
10. Turn selector valve to **VACUUM** until the pressure gauge reads about 25 inches Hg
11. Repeat filling the chamber with Nitrogen and evacuating 5 times
12. Turn the selector valve to **OFF** when the pressure is 15 inches Hg

Deposit Silane:

13. Turn the silane valve **ON** (vertical), exposing the silane to the chamber
14. Leave the mircowell molds in the silane chamber overnight (6+ hours)
15. Turn the sign to the red side indicating that there is a run in progress, leave a note with your name and number

Purge Chamber:

16. Turn the silane valve **OFF** (horizontal)
17. Fill the chamber with Nitrogen and evacuate with vacuum 5 times to remove the silane from the chamber

Shutdown:

18. Move all valves to **OFF** position (selector valve pointing up, isolation and silane valves horizontal)
19. Remove molds from chamber
20. Turn off vacuum pump and close the fume hood Nitrogen valve
21. Turn sign to the green side (indicating no run in progress)

Step 3: After silanizing, allow the molds to sit in the hood for 10 minutes, then bake for 30 minutes at 70°C.

---

[3] This protocol was adapted from a silane rig protocol written by Dr. Dave Bothman and a mold silanization protocol written by Dr. Robin Wilson

Appendix E – Photolithography Parameters for Microwells Wafers

We sought to make our microwells wafer with ~10μm feature height. To do so, we consulted the datasheet for SU-8 2010 (from Kayaku AM), the photoresist used to make the microwells molds. We tested the following spin coating speeds (Table E-1), with all other parameters held the same.

Table E-1: Adjusted lithography parameters for wafers with varying feature heights.

	Test #1 – 1100 RPM	**Test #2 – 1500 RPM**	**Test #3 – 2000 RPM**
Spin coat	500 rpm for 10s, a = 100 rpm/s 1100 rpm for 30s, a = 300 rpm/s	500 rpm for 10s, a = 100 rpm/s 1500 rpm for 30s, a = 300 rpm/s	500 rpm for 10s, a = 100 rpm/s 2000 rpm for 30s, a = 300 rpm/s
Soft bake	2 min at 95°C		
Exposure	130 mJ/cm^2		
Post-exposure bake	4 min at 95°C		
Development	2-3 mins in SU-8 Developer with agitation		
Hard bake	Start spin coater hot plate at 120°C and set to 180°C When hot plate reaches 180°C, turn off and let wafer stay on hot plate and cool overnight		

Table E-2: Mean feature height of microwells molds made with the parameters listed in Table D-1.

Test #1 – 1100 RPM	**Test #2 – 1500 RPM**	**Test #3 – 2000 RPM**
12.44 +/- 0.1232 μm	10.61 +/- 0.1702 μm	8.679 +/- 0.2382 μm

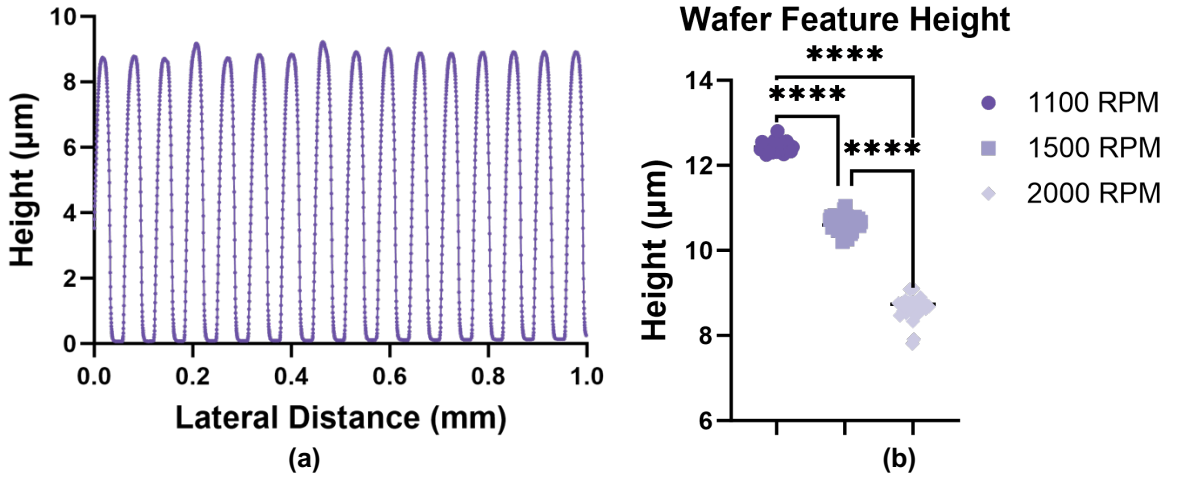

Figure E-1. Photolithography mold characterization. (a) Example trace of Dektak scan over microwells wafer mold. (b) Feature height for wafers with varying spin coating speed.

7. Bibliography

1. Benjamin, E.J., et al., *Heart Disease and Stroke Statistics-2019 Update: A Report From the American Heart Association.* Circulation, 2019. **139**(10): p. e56-e528.
2. Bergmann, O., et al., *Evidence for cardiomyocyte renewal in humans.* Science, 2009. **324**(5923): p. 98-102.
3. Brandenburger, M., et al., *Organotypic slice culture from human adult ventricular myocardium.* Cardiovasc Res, 2012. **93**(1): p. 50-9.
4. Milani-Nejad, N. and P.M.L. Janssen, *Small and large animal models in cardiac contraction research: Advantages and disadvantages.* Pharmacology & Therapeutics, 2014. **141**(3): p. 235-249.
5. Hasenfuss, G., *Animal models of human cardiovascular disease, heart failure and hypertrophy.* Cardiovascular Research, 1998. **39**(1): p. 60-76.
6. Schroer, A., et al., *Engineering hiPSC cardiomyocyte in vitro model systems for functional and structural assessment.* Progress in Biophysics and Molecular Biology, 2019. **144**: p. 3-15.
7. Weiss, A. and L.A. Leinwand, *The mammalian myosin heavy chain gene family.* Annual Review of Cell and Developmental Biology, 1996. **12**(1): p. 417-439.
8. Shephard, R. and C. Semsarian, *Role of Animal Models in HCM Research.* Journal of Cardiovascular Translational Research, 2009. **2**(4): p. 471-482.
9. Jung, G. and D. Bernstein, *hiPSC modeling of inherited cardiomyopathies.* Current Treatment Options in Cardiovascular Medicine, 2014. **16**(7).
10. Uosaki, H. and Y.H. Taguchi, *Comparative Gene Expression Analysis of Mouse and Human Cardiac Maturation.* Genomics Proteomics Bioinformatics, 2016. **14**(4): p. 207-15.
11. Burridge, P.W., et al., *Chemically defined generation of human cardiomyocytes.* Nat Methods, 2014. **11**(8): p. 855-60.
12. Eschenhagen, T., C. Mummery, and B.C. Knollmann, *Modelling sarcomeric cardiomyopathies in the dish: From human heart samples to iPSC cardiomyocytes.* Cardiovascular Research, 2015. **105**(4): p. 424-438.
13. Zhang, J., et al., *Functional cardiomyocytes derived from human induced pluripotent stem cells.* Circulation Research, 2009. **104**(4).
14. Karakikes, I., et al., *Human Induced Pluripotent Stem Cell-Derived Cardiomyocytes: Insights into Molecular, Cellular, and Functional Phenotypes*. 2015, Lippincott Williams and Wilkins. p. 80-88.
15. Ribeiro, A.J., et al., *Contractility of single cardiomyocytes differentiated from pluripotent stem cells depends on physiological shape and substrate stiffness.* Proc Natl Acad Sci U S A, 2015. **112**(41): p. 12705-10.
16. Roberts, B., et al., *Systematic gene tagging using CRISPR/Cas9 in human stem cells to illuminate cell organization.* Molecular Biology of the Cell, 2017. **28**(21): p. 2854-2874.
17. Simmons, C.S., B.C. Petzold, and B.L. Pruitt, *Microsystems for biomimetic stimulation of cardiac cells.* Lab on a Chip, 2012. **12**(18): p. 3235-3248.

18. Chopra, A., et al., *Cardiac myocyte remodeling mediated by N-cadherin-dependent mechanosensing.* American Journal of Physiology - Heart and Circulatory Physiology, 2011. **300**(4): p. 1252-1266.
19. Luo, Y. and G.L. Radice, *Cadherin-mediated adhesion is essential for myofibril continuity across the plasma membrane but not for assembly of the contractile apparatus.* Journal of Cell Science, 2003. **116**(8): p. 1471-1479.
20. Roberts, B., et al., *Fluorescent Gene Tagging of Transcriptionally Silent Genes in hiPSCs.* Stem Cell Reports, 2019. **12**(5): p. 1145-1158.
21. Gopalan, C. and E. Kirk, *The heart*, in *Biology of Cardiovascular and Metabolic Diseases*, C.G.a.E. Kirk, Editor. 2022, Academic Press. p. 1-33.
22. Yang, X., L. Pabon, and C.E. Murry, *Engineering adolescence: maturation of human pluripotent stem cell-derived cardiomyocytes.* Circ Res, 2014. **114**(3): p. 511-23.
23. Sheehy, S.P., et al., *Quality metrics for stem cell-derived cardiac myocytes.* Stem Cell Reports, 2014. **2**(3): p. 282-294.
24. Robertson, C., D.D. Tran, and S.C. George, *Concise review: Maturation phases of human pluripotent stem cell-derived cardiomyocytes.* Stem Cells, 2013. **31**(5): p. 829-837.
25. Melero, C., et al., *Light-Induced Molecular Adsorption of Proteins Using the PRIMO System for Micro-Patterning to Study Cell Responses to Extracellular Matrix Proteins.* Journal of Visualized Experiments, 2019(152).
26. Wilbur, J.L., et al., *Microfabrication by microcontact printing of self-assembled monolayers.* Advanced Materials, 1994. **6**(7-8): p. 600-604.
27. Nelson, C.M., et al., *Degradation of micropatterned surfaces by cell-dependent and -independent processes.* Langmuir, 2003. **19**(5): p. 1493-1499.
28. Tang, X., M. Yakut Ali, and M.T.A. Saif, *A novel technique for micro-patterning proteins and cells on polyacrylamide gels.* Soft Matter, 2012. **8**(27): p. 7197-7206.
29. Moeller, J., et al., *Controlling cell shape on hydrogels using liftoff protein patterning.* PLoS ONE, 2018. **13**(1): p. 1-17.
30. Bray, M.-A., S.P. Sheehy, and K.K. Parker, *Sarcomere alignment is regulated by myocyte shape.* Cell Motility and the Cytoskeleton, 2008. **65**(8): p. 641-651.
31. Wang, G., et al., *Modeling the mitochondrial cardiomyopathy of Barth syndrome with induced pluripotent stem cell and heart-on-chip technologies.* Nature Medicine, 2014. **20**(6): p. 616-623.
32. Kane, R.S., et al., *Patterning proteins and cells using soft lithography.* Biomaterials, 1999. **20**: p. 2363-2376.
33. Sarker, B., C. Walter, and A. Pathak, *Direct Micropatterning of Extracellular Matrix Proteins on Functionalized Polyacrylamide Hydrogels Shows Geometric Regulation of Cell-Cell Junctions.* ACS Biomaterials Science and Engineering, 2018. **4**(7): p. 2340-2349.
34. Damljanović, V., B.C. Lagerholm, and K. Jacobson, *Bulk and micropatterned conjugation of extracellular matrix proteins to characterized polyacrylamide*

substrates for cell mechanotransduction assays. BioTechniques, 2005. **39**(6): p. 847-851.
35. Denisin, A.K. and B.L. Pruitt, *Tuning the Range of Polyacrylamide Gel Stiffness for Mechanobiology Applications.* ACS Applied Materials and Interfaces, 2016. **8**(34): p. 21893-21902.
36. Tse, J.R. and A.J. Engler, *Preparation of hydrogel substrates with tunable mechanical properties*. 2010, John Wiley & Sons, Ltd. p. 10.16.1-10.16.16.
37. Berry, M.F., et al., *Mesenchymal stem cell injection after myocardial infarction improves myocardial compliance.* Am J Physiol Heart Circ Physiol, 2006. **290**(6): p. H2196-203.
38. Majkut, S., et al., *Heart-specific stiffening in early embryos parallels matrix and myosin expression to optimize beating.* Curr Biol, 2013. **23**(23): p. 2434-9.
39. Parker, K.K., et al., *Myofibrillar architecture in engineered cardiac myocytes.* Circulation Research, 2008. **103**(4): p. 340-342.
40. Chirikian, O., et al., *The effects of xeno-free cryopreservation on the contractile properties of human iPSC derived cardiomyocytes.* J Mol Cell Cardiol, 2022. **168**: p. 107-114.
41. McCain, M.L., et al., *Cooperative coupling of cell-matrix and cell-cell adhesions in cardiac muscle.* Proceedings of the National Academy of Sciences of the United States of America, 2012. **109**(25): p. 9881-9886.
42. Schinner, C., et al., *Regulation of cardiac myocyte cohesion and gap junctions via desmosomal adhesion.* Acta Physiologica, 2019. **226**(2): p. e13242.
43. Boudou, T., et al., *A microfabricated platform to measure and manipulate the mechanics of engineered cardiac microtissues.* Tissue Engineering - Part A, 2012. **18**(9-10): p. 910-919.
44. Eschenhagen, T., et al., *Three-dimensional reconstitution of embryonic cardiomyocytes in a collagen matrix: a new heart muscle model system.* The FASEB Journal, 1997. **11**(8): p. 683-694.
45. Tulloch, N.L., et al., *Growth of Engineered Human Myocardium With Mechanical Loading and Vascular Coculture.* Circulation Research, 2011. **109**(1): p. 47-59.
46. Ronaldson-Bouchard, K., et al., *Advanced maturation of human cardiac tissue grown from pluripotent stem cells.* Nature, 2018. **556**(7700): p. 239-243.
47. Mannhardt, I., et al., *Human Engineered Heart Tissue: Analysis of Contractile Force.* Stem Cell Reports, 2016. **7**(1): p. 29-42.
48. Wilson, R.E., et al., *3D Microwell Platforms for Control of Single Cell 3D Geometry and Intracellular Organization.* Cellular and Molecular Bioengineering, 2021. **14**(1): p. 1-14.
49. Chopra, A., et al., *α-Catenin Localization and Sarcomere Self-Organization on N-Cadherin Adhesive Patterns Are Myocyte Contractility Driven.* PLoS ONE, 2012. **7**(10).

50. Castillo, E.A., K.V. Lane, and B.L. Pruitt, *Micromechanobiology: Focusing on the Cardiac Cell-Substrate Interface.* Annual Review of Biomedical Engineering, 2020. **22**: p. 257-284.
51. Kim, A.A., et al., *Wafer-Scale Patterning of Protein Templates for Hydrogel Fabrication.* Micromachines, 2021. **12**(11): p. 1386.
52. Bowers, S.L., et al., *Desmoplakin is important for proper cardiac cell-cell interactions.* Microsc Microanal, 2012. **18**(1): p. 107-14.
53. Rienks, M., et al., *Myocardial extracellular matrix: an ever-changing and diverse entity.* Circ Res, 2014. **114**(5): p. 872-88.
54. Zak, R., *Cell proliferation during cardiac growth.* Am J Cardiol, 1973. **31**(2): p. 211-9.
55. Spater, D., et al., *How to make a cardiomyocyte.* Development, 2014. **141**(23): p. 4418-31.
56. De Franceschi, N., et al., *Integrin traffic - the update.* J Cell Sci, 2015. **128**(5): p. 839-52.
57. Frantz, C., K.M. Stewart, and V.M. Weaver, *The extracellular matrix at a glance.* J Cell Sci, 2010. **123**(Pt 24): p. 4195-200.
58. Hynes, R.O., *The extracellular matrix: not just pretty fibrils.* Science, 2009. **326**(5957): p. 1216-9.
59. Israeli-Rosenberg, S., et al., *Integrins and integrin-associated proteins in the cardiac myocyte.* Circ Res, 2014. **114**(3): p. 572-586.
60. Michele, D.E., et al., *Dystroglycan matrix receptor function in cardiac myocytes is important for limiting activity-induced myocardial damage.* Circ Res, 2009. **105**(10): p. 984-93.
61. Adams, J.C. and A. Brancaccio, *The evolution of the dystroglycan complex, a major mediator of muscle integrity.* Biol Open, 2015. **4**(9): p. 1163-79.
62. Xie, J., et al., *Syndecan-4 Signaling Is Required for Exercise-Induced Cardiac Hypertrophy.* Mol Med, 2016. **22**: p. 192-201.
63. Peter, A.K., et al., *The costamere bridges sarcomeres to the sarcolemma in striated muscle.* Prog Pediatr Cardiol, 2011. **31**(2): p. 83-88.
64. Samarel, A.M., *Costameres, focal adhesions, and cardiomyocyte mechanotransduction.* Am J Physiol Heart Circ Physiol, 2005. **289**(6): p. H2291-301.
65. Baldwin, H.S. and C.A. Buck, *Integrins and other cell adhesion molecules in cardiac development.* Trends Cardiovasc Med, 1994. **4**(4): p. 178-87.
66. Forbes, M.S. and N. Sperelakis, *Intercalated discs of mammalian heart: a review of structure and function.* Tissue Cell, 1985. **17**(5): p. 605-48.
67. Ross, R.S. and T.K. Borg, *Integrins and the myocardium*. 2001, Lippincott Williams and Wilkins. p. 1112-1119.
68. Huveneers, S. and E.H. Danen, *Adhesion signaling - crosstalk between integrins, Src and Rho.* J Cell Sci, 2009. **122**(Pt 8): p. 1059-69.
69. Humphries, J.D., et al., *Signal transduction via integrin adhesion complexes.* Curr Opin Cell Biol, 2019. **56**: p. 14-21.
70. Lundgren, E., et al., *In vitro studies on adult cardiac myocytes: attachment and biosynthesis of collagen type IV and laminin.* J Cell Physiol, 1988. **136**(1): p. 43-53.

71. Mott, J.D. and Z. Werb, *Regulation of matrix biology by matrix metalloproteinases.* Curr Opin Cell Biol, 2004. **16**(5): p. 558-64.
72. Miner, E.C. and W.L. Miller, *A look between the cardiomyocytes: the extracellular matrix in heart failure.* Mayo Clin Proc, 2006. **81**(1): p. 71-6.
73. Mishra, P.K., et al., *Cardiac matrix: a clue for future therapy.* Biochim Biophys Acta, 2013. **1832**(12): p. 2271-6.
74. Marsico, G., et al., *Glycosylation and Integrin Regulation in Cancer.* Trends in Cancer, 2018. **4**(8): p. 537-552.
75. Seetharaman, S. and S. Etienne-Manneville, *Integrin diversity brings specificity in mechanotransduction.* Biology of the Cell, 2018. **110**(3): p. 49-64.
76. Barczyk, M., S. Carracedo, and D. Gullberg, *Integrins.* Cell and Tissue Research, 2010. **339**(1): p. 269-280.
77. Barczyk, M., S. Carracedo, and D. Gullberg, *Integrins.* Cell Tissue Res, 2010. **339**(1): p. 269-80.
78. Takahashi, K., et al., *Induction of pluripotent stem cells from adult human fibroblasts by defined factors.* Cell, 2007. **131**(5): p. 861-72.
79. Gherghiceanu, M., et al., *Cardiomyocytes derived from human embryonic and induced pluripotent stem cells: comparative ultrastructure.* J Cell Mol Med, 2011. **15**(11): p. 2539-51.
80. Scuderi, G.J. and J. Butcher, *Naturally engineered maturation of cardiomyocytes*. 2017, Frontiers Media S.A. p. 50-50.
81. Spudich, J.A., *Hypertrophic and dilated cardiomyopathy: Four decades of basic research on muscle lead to potential therapeutic approaches to these devastating genetic diseases*. 2014, Biophysical Society. p. 1236-1249.
82. Kolanowski, T.J., C.L. Antos, and K. Guan, *Making human cardiomyocytes up to date: Derivation, maturation state and perspectives.* Int J Cardiol, 2017. **241**: p. 379-386.
83. Lundy, S.D., et al., *Structural and functional maturation of cardiomyocytes derived from human pluripotent stem cells.* Stem Cells Dev, 2013. **22**(14): p. 1991-2002.
84. Liu, A.P., O. Chaudhuri, and S.H. Parekh, *New advances in probing cell-extracellular matrix interactions.* Integr Biol (Camb), 2017. **9**(5): p. 383-405.
85. Darnell, M. and D.J. Mooney, *Leveraging advances in biology to design biomaterials.* Nat Mater, 2017. **16**(12): p. 1178-1185.
86. Campbell, I.D. and M.J. Humphries, *Integrin structure, activation, and interactions.* Cold Spring Harb Perspect Biol, 2011. **3**(3).
87. Humphries, J.D., A. Byron, and M.J. Humphries, *Integrin ligands at a glance.* J Cell Sci, 2006. **119**(Pt 19): p. 3901-3.
88. Roca-Cusachs, P., et al., *Clustering of alpha(5)beta(1) integrins determines adhesion strength whereas alpha(v)beta(3) and talin enable mechanotransduction.* Proc Natl Acad Sci U S A, 2009. **106**(38): p. 16245-50.
89. Balcioglu, H.E., et al., *The integrin expression profile modulates orientation and dynamics of force transmission at cell-matrix adhesions.* J Cell Sci, 2015. **128**(7): p. 1316-26.

90. Kechagia, J.Z., J. Ivaska, and P. Roca-Cusachs, *Integrins as biomechanical sensors of the microenvironment.* Nat Rev Mol Cell Biol, 2019. **20**(8): p. 457-473.
91. Vogel, C. and E.M. Marcotte, *Insights into the regulation of protein abundance from proteomic and transcriptomic analyses.* Nat Rev Genet, 2012. **13**(4): p. 227-32.
92. Meliopoulos, V.A. and S. Schultz-Cherry, *Although it's painful: The importance of stringent antibody validation.* PLoS Pathog, 2018. **14**(1): p. e1006701.
93. Chen, C., et al., *Integrins and integrin-related proteins in cardiac fibrosis.* Journal of Molecular and Cellular Cardiology, 2016. **93**: p. 162-174.
94. Brancaccio, M., et al., *Differential Onset of Expression of α7 and β1D Integrins During Mouse Heart and Skeletal Muscle Development.* Cell Adhesion and Communication, 1998. **5**(3): p. 193-205.
95. Wiencierz, A.M., et al., *Differential Expression Levels of Integrin alpha6 Enable the Selective Identification and Isolation of Atrial and Ventricular Cardiomyocytes.* PLoS One, 2015. **10**(11): p. e0143538.
96. Terracio, L., et al., *Expression of Collagen Binding Integrins During Cardiac Development and Hypertrophy.* Circulation Research, 1991. **68**: p. 734-744.
97. Nawata, J., et al., *Differential expression of a1, a3 and a5 integrin subunits in acute and chronic stages of myocardial infarction in rats.* Cardiovascular Research, 1999. **43**: p. 371-381.
98. Babbitt, C.J., et al., *Modulation of integrins and integrin signaling molecules in the pressure-loaded murine ventricle.* Histochem Cell Biol, 2002. **118**(6): p. 431-9.
99. van der Flier, A., et al., *Spatial and temporal expression of the beta1D integrin during mouse development.* Dev Dyn, 1997. **210**(4): p. 472-86.
100. Ichikawa, Y., et al., *Modulation of caveolins, integrins and plasma membrane repair proteins in anthracycline-induced heart failure in rabbits.* PLoS One, 2017. **12**(5): p. e0177660.
101. Krishnamurthy, P., et al., *Deficiency of beta1 integrins results in increased myocardial dysfunction after myocardial infarction.* Heart, 2006. **92**(9): p. 1309-15.
102. Manso, A.M., et al., *Loss of mouse cardiomyocyte talin-1 and talin-2 leads to beta-1 integrin reduction, costameric instability, and dilated cardiomyopathy.* Proc Natl Acad Sci U S A, 2017. **114**(30): p. E6250-E6259.
103. Schips, T.G., et al., *Thrombospondin-3 augments injury-induced cardiomyopathy by intracellular integrin inhibition and sarcolemmal instability.* Nat Commun, 2019. **10**(1): p. 76.
104. Domogatskaya, A., S. Rodin, and K. Tryggvason, *Functional diversity of laminins.* Annu Rev Cell Dev Biol, 2012. **28**: p. 523-53.
105. Belkin, A.M., et al., *Beta 1D integrin displaces the beta 1A isoform in striated muscles: localization at junctional structures and signaling potential in nonmuscle cells.* J Cell Biol, 1996. **132**(1-2): p. 211-26.

106. Sun, M., et al., *Temporal response and localization of integrins beta1 and beta3 in the heart after myocardial infarction: regulation by cytokines.* Circulation, 2003. **107**(7): p. 1046-52.
107. Rowland, T.J., et al., *Roles of integrins in human induced pluripotent stem cell growth on Matrigel and vitronectin.* Stem Cells Dev, 2010. **19**(8): p. 1231-40.
108. Ja, K.P., et al., *iPSC-derived human cardiac progenitor cells improve ventricular remodelling via angiogenesis and interstitial networking of infarcted myocardium.* J Cell Mol Med, 2016. **20**(2): p. 323-32.
109. Yu, T., et al., *In vivo differentiation of induced pluripotent stem cell-derived cardiomyocytes.* Circ J, 2013. **77**(5): p. 1297-306.
110. Karpievitch, Y.V., et al., *Liquid Chromatography Mass Spectrometry-Based Proteomics: Biological and Technological Aspects.* Ann Appl Stat, 2010. **4**(4): p. 1797-1823.
111. *Cardiac Extracellular Matrix Fundamental Science to Clinical Applications*. Advances in Experimental Medicine and Biology 1098, ed. E.G. Schmuck, P. Hematti, and A.N. Raval. 2018: Springer, Cham.
112. Chang, C.W., et al., *Cardiac extracellular matrix proteomics: Challenges, techniques, and clinical implications.* Proteomics Clin Appl, 2016. **10**(1): p. 39-50.
113. Schwach, V. and R. Passier, *Native cardiac environment and its impact on engineering cardiac tissue.* Biomaterials Science, 2019.
114. Hanson, K.P., et al., *Spatial and temporal analysis of extracellular matrix proteins in the developing murine heart: A blueprint for regeneration.* Tissue Engineering - Part A, 2013. **19**(9-10): p. 1132-1143.
115. Borg, T.K., R.E. Gay, and L.D. Johnson, *Changes in the distribution of fibronectin and collagen during development of the neonatal rat heart.* Coll Relat Res, 1982. **2**(3): p. 211-8.
116. Gershlak, J.R., et al., *Mesenchymal stem cells ability to generate traction stress in response to substrate stiffness is modulated by the changing extracellular matrix composition of the heart during development.* Biochem Biophys Res Commun, 2013. **439**(2): p. 161-6.
117. Williams, C., et al., *Young developmental age cardiac extracellular matrix promotes the expansion of neonatal cardiomyocytes in vitro.* Acta Biomater, 2014. **10**(1): p. 194-204.
118. Wei, S., et al., *Left and right ventricular collagen type I/III ratios and remodeling post-myocardial infarction.* J Card Fail, 1999. **5**(2): p. 117-26.
119. Quinn, K.P., et al., *Optical metrics of the extracellular matrix predict compositional and mechanical changes after myocardial infarction.* Sci Rep, 2016. **6**: p. 35823.
120. Sullivan, K.E., et al., *Extracellular matrix remodeling following myocardial infarction influences the therapeutic potential of mesenchymal stem cells.* Stem Cell Res Ther, 2014. **5**(1): p. 14.
121. Bashey, R.I., A. Martinez-Hernandez, and S.A. Jimenez, *Isolation, characterization, and localization of cardiac collagen type VI: Associations*

with other extracellular matrix components. Circulation Research, 1992. **70**(5): p. 1006-1017.
122. Roediger, M., N. Miosge, and N. Gersdorff, *Tissue distribution of the laminin beta1 and beta2 chain during embryonic and fetal human development.* J Mol Histol, 2010. **41**(2-3): p. 177-84.
123. Yap, L., et al., *In Vivo Generation of Post-infarct Human Cardiac Muscle by Laminin-Promoted Cardiovascular Progenitors.* Cell Rep, 2019. **26**(12): p. 3231-3245 e9.
124. Ulrich, M.M.W., et al., *Increased Expression of Fibronectin Isoforms After Myocardial Infarction in Rats.* Journal of Molecular and Cellular Cardiology, 1997. **29**(9): p. 2533-2543.
125. van Dijk, A., et al., *Accumulation of fibronectin in the heart after myocardial infarction: a putative stimulator of adhesion and proliferation of adipose-derived stem cells.* Cell Tissue Res, 2008. **332**(2): p. 289-98.
126. Balasubramanian, S., et al., *beta3 integrin in cardiac fibroblast is critical for extracellular matrix accumulation during pressure overload hypertrophy in mouse.* PLoS One, 2012. **7**(9): p. e45076.
127. de Souza, R.R., *Aging of myocardial collagen.* Biogerontology, 2002. **3**(6): p. 325-35.
128. Berk, B.C., K. Fujiwara, and S. Lehoux, *ECM remodeling in hypertensive heart disease.* Journal of Clinical Investigation, 2007. **117**(3): p. 568-575.
129. Fomovsky, G.M., S. Thomopoulos, and J.W. Holmes, *Contribution of extracellular matrix to the mechanical properties of the heart.* J Mol Cell Cardiol, 2010. **48**(3): p. 490-6.
130. Speiser, B., C.F. Riess, and J. Schaper, *The extracellular matrix in human myocardium: Part I: Collagens I, III, IV, and VI.* Cardioscience, 1991. **2**(4): p. 225-32.
131. Marijianowski, M.M., et al., *The neonatal heart has a relatively high content of total collagen and type I collagen, a condition that may explain the less compliant state.* J Am Coll Cardiol, 1994. **23**(5): p. 1204-8.
132. Yang, H., et al., *Interactive relationship between basement-membrane development and sarcomerogenesis in single cardiomyocytes.* Exp Cell Res, 2015. **330**(1): p. 222-32.
133. Luther, D.J., et al., *Absence of type VI collagen paradoxically improves cardiac function, structure, and remodeling after myocardial infarction.* Circ Res, 2012. **110**(6): p. 851-6.
134. Rasi, K., et al., *Collagen XV is necessary for modeling of the extracellular matrix and its deficiency predisposes to cardiomyopathy.* Circ Res, 2010. **107**(10): p. 1241-52.
135. Jourdan-Lesaux, C., J. Zhang, and M.L. Lindsey, *Extracellular matrix roles during cardiac repair.* Life Sci, 2010. **87**(13-14): p. 391-400.
136. Boateng, S.Y., et al., *RGD and YIGSR synthetic peptides facilitate cellular adhesion identical to that of laminin and fibronectin but alter the physiology of neonatal cardiac myocytes.* Am J Physiol Cell Physiol, 2005. **288**(1): p. C30-8.

137. Linask, K.K. and J.W. Lash, *A role for fibronectin in the migration of avian precardiac cells. II. Rotation of the heart-forming region during different stages and its effects.* Dev Biol, 1988. **129**(2): p. 324-9.
138. Ramos, I.T., et al., *Simultaneous Assessment of Cardiac Inflammation and Extracellular Matrix Remodeling after Myocardial Infarction.* Circ Cardiovasc Imaging, 2018. **11**(11).
139. Lee, J.P., et al., *N-terminal specific conjugation of extracellular matrix proteins to 2-pyridinecarboxaldehyde functionalized polyacrylamide hydrogels.* Biomaterials, 2016. **102**: p. 268-276.
140. Halldorsson, S., et al., *Advantages and challenges of microfluidic cell culture in polydimethylsiloxane devices.* Biosensors and Bioelectronics, 2015. **63**: p. 218-231.
141. Ribeiro, A.J.S., et al., *For whom the cells pull: Hydrogel and micropost devices for measuring traction forces.* Methods, 2016. **94**: p. 51-64.
142. Pelham, R.J. and Y.L. Wang, *Cell locomotion and focal adhesions are regulated by substrate flexibility.* Proceedings of the National Academy of Sciences of the United States of America, 1997. **94**(25): p. 13661-13665.
143. Lekka, M., J. Pabijan, and B. Orzechowska, *Morphological and mechanical stability of bladder cancer cells in response to substrate rigidity.* Biochimica et Biophysica Acta - General Subjects, 2019. **1863**(6): p. 1006-1014.
144. Wen, J.H., et al., *Interplay of Matrix Stiffness and Protein Tethering in Stem Cell Differentiation.* Nature Materials, 2014. **13**(10): p. 979-987.
145. Dembo, M. and Y.L. Wang, *Stresses at the cell-to-substrate interface during locomotion of fibroblasts.* Biophysical Journal, 1999. **76**(4): p. 2307-2316.
146. Charrier, E.E., et al., *Control of cell morphology and differentiation by substrates with independently tunable elasticity and viscous dissipation.* Nature Communications, 2018. **9**(1): p. 1-13.
147. Reinhart-King, C.A., M. Dembo, and D.A. Hammer, *The dynamics and mechanics of endothelial cell spreading.* Biophysical Journal, 2005. **89**(1): p. 676-689.
148. Gokaltun, A., et al., *Recent advances in nonbiofouling PDMS surface modification strategies applicable to microfluidic technology.* Technology, 2017. **5**(1): p. 1-12.
149. Khnouf, R., D. Karasneh, and B.A. Albiss, *Protein immobilization on the surface of polydimethylsiloxane and polymethyl methacrylate microfluidic devices.* Electrophoresis, 2016. **37**(3): p. 529-535.
150. De Silva, M.N., R. Desai, and D.J. Odde, *Micro-Patterning of Animal Cells on PDMS Substrates in the Presence of Serum without Use of Adhesion Inhibitors.* Biomedical Microdevices, 2004. **6**(3): p. 219-222.
151. Eteshola, E. and D. Leckband, *Development and characterization of an ELISA assay in PDMS microfluidic channels.* Sensors and Actuators, B: Chemical, 2001. **72**(2): p. 129-133.
152. Mobasseri, S.A., et al., *Patterning of human epidermal stem cells on undulating elastomer substrates reflects differences in cell stiffness.* Acta Biomaterialia, 2019. **87**: p. 256-264.

153. Kim, Y., C. Kwon, and H. Jeon, *Genetically engineered phage induced selective H9c2 cardiomyocytes patterning in PDMS microgrooves.* Materials, 2017. **10**(8): p. 1-8.
154. Ferguson, G.S., et al., *Monolayers on Disordered Substrates: Self-Assembly of Alkyltrichlorosilanes on Surface-Modified Polyethylene and Poly(dimethylsiloxane).* Macromolecules, 1993. **26**(22): p. 5870-5875.
155. Chaudhury, M.K. and G.M. Whitesides, *Direct Measurement of Interfacial Interactions between Semispherical Lenses and Flat Sheets of Poly(dimethylsiloxane) and Their Chemical Derivatives.* Langmuir, 1991. **7**(5): p. 1013-1025.
156. Zhang, W., et al., *Studying cancer stem cell dynamics on PDMS surfaces for microfluidics device design.* Scientific Reports, 2013. **3**: p. 1-8.
157. Yang, Y., et al., *Effects of topographical and mechanical property alterations induced by oxygen plasma modification on stem cell behavior.* ACS Nano, 2012. **6**(10): p. 8591-8598.
158. Nam, K.H., et al., *Probing mechanoregulation of neuronal differentiation by plasma lithography patterned elastomeric substrates.* Scientific Reports, 2014. **4**: p. 1-9.
159. Farrell, M. and S. Beaudoin, *Surface forces and protein adsorption on dextran- and polyethylene glycol-modified polydimethylsiloxane.* Colloids and Surfaces B: Biointerfaces, 2010. **81**(2): p. 468-475.
160. Hu, S., et al., *Protein-Substrate Adhesion in Microcontact Printing Regulates Cell Behavior.* Langmuir, 2018. **34**(4): p. 1750-1759.
161. Kuddannaya, S., et al., *Surface chemical modification of poly(dimethylsiloxane) for the enhanced adhesion and proliferation of mesenchymal stem cells.* ACS Applied Materials and Interfaces, 2013. **5**(19): p. 9777-9784.
162. Leivo, J., et al., *A durable and biocompatible ascorbic acid-based covalent coating method of polydimethylsiloxane for dynamic cell culture.* Journal of The Royal Society Interface, 2017. **14**(132): p. 20170318-20170318.
163. Huang, B., et al., *Phospholipid biotinylation of polydimethylsiloxane (PDMS) for protein immobilization.* Lab on a Chip, 2006. **6**(3): p. 369-373.
164. Wang, R.M. and K.L. Christman, *Decellularized myocardial matrix hydrogels: In basic research and preclinical studies.* Adv Drug Deliv Rev, 2016. **96**: p. 77-82.
165. Santoro, R., et al., *Unchain My Heart: Integrins at the Basis of iPSC Cardiomyocyte Differentiation.* Stem Cells Int, 2019. **2019**: p. 8203950.
166. Bejleri, D. and M.E. Davis, *Decellularized Extracellular Matrix Materials for Cardiac Repair and Regeneration.* Adv Healthc Mater, 2019. **8**(5): p. e1801217.
167. Taylor, D.A., R.B. Parikh, and L.C. Sampaio, *Bioengineering Hearts: Simple yet Complex.* Curr Stem Cell Rep, 2017. **3**(1): p. 35-44.
168. Paoletti, C., C. Divieto, and V. Chiono, *Impact of Biomaterials on Differentiation and Reprogramming Approaches for the Generation of Functional Cardiomyocytes.* Cells, 2018. **7**(9).

169. Chen, Q.Z., et al., *Biomaterials in cardiac tissue engineering: Ten years of research survey.* Materials Science & Engineering R-Reports, 2008. **59**(1-6): p. 1-37.
170. Segers, V.F. and R.T. Lee, *Biomaterials to enhance stem cell function in the heart.* Circ Res, 2011. **109**(8): p. 910-22.
171. Borg, T.K., et al., *Recognition of extracellular matrix components by neonatal and adult cardiac myocytes.* Dev Biol, 1984. **104**(1): p. 86-96.
172. Hirata, N., et al., *A chemical probe that labels human pluripotent stem cells.* Cell Rep, 2014. **6**(6): p. 1165-1174.
173. Patel, A.K., et al., *A defined synthetic substrate for serum-free culture of human stem cell derived cardiomyocytes with improved functional maturity identified using combinatorial materials microarrays.* Biomaterials, 2015. **61**: p. 257-65.
174. Battista, S., et al., *The effect of matrix composition of 3D constructs on embryonic stem cell differentiation.* Biomaterials, 2005. **26**(31): p. 6194-207.
175. Jung, J.P., et al., *An integrated statistical model for enhanced murine cardiomyocyte differentiation via optimized engagement of 3D extracellular matrices.* Sci Rep, 2015. **5**: p. 18705.
176. Discher, D.E., P. Janmey, and Y.L. Wang, *Tissue cells feel and respond to the stiffness of their substrate.* Science, 2005. **310**(5751): p. 1139-43.
177. Corbin, E.A., et al., *Tunable and Reversible Substrate Stiffness Reveals a Dynamic Mechanosensitivity of Cardiomyocytes.* ACS Appl Mater Interfaces, 2019. **11**(23): p. 20603-20614.
178. Tambe, D.T., et al., *Collective cell guidance by cooperative intercellular forces.* Nature Materials, 2011. **10**(6): p. 469-475.
179. Engler, A.J., et al., *Embryonic cardiomyocytes beat best on a matrix with heart-like elasticity: scar-like rigidity inhibits beating.* Journal of Cell Science, 2008. **121**(22): p. 3794-3802.
180. Chung, C., et al., *Hydrogel crosslinking density regulates temporal contractility of human embryonic stem cell-derived cardiomyocytes in 3D cultures.* Soft Matter, 2012. **8**(39): p. 10141-10148.
181. Hirata, M. and T. Yamaoka, *Effect of stem cell niche elasticity/ECM protein on the self-beating cardiomyocyte differentiation of induced pluripotent stem (iPS) cells at different stages.* Acta Biomater, 2018. **65**: p. 44-52.
182. Kong, Y.P., et al., *A systems mechanobiology model to predict cardiac reprogramming outcomes on different biomaterials.* Biomaterials, 2018. **181**: p. 280-292.
183. Branco, M.A., et al., *Transcriptomic analysis of 3D Cardiac Differentiation of Human Induced Pluripotent Stem Cells Reveals Faster Cardiomyocyte Maturation Compared to 2D Culture.* Scientific Reports, 2019. **9**(1): p. 1-13.
184. Kerscher, P., et al., *Direct hydrogel encapsulation of pluripotent stem cells enables ontomimetic differentiation and growth of engineered human heart tissues.* Biomaterials, 2016. **83**: p. 383-95.
185. Zhang, D., et al., *Tissue-engineered cardiac patch for advanced functional maturation of human ESC-derived cardiomyocytes.* Biomaterials, 2013. **34**(23): p. 5813-20.

186. Lemoine, M.D., et al., *Human iPSC-derived cardiomyocytes cultured in 3D engineered heart tissue show physiological upstroke velocity and sodium current density.* Sci Rep, 2017. **7**(1): p. 5464.
187. Carson, D., et al., *Nanotopography-Induced Structural Anisotropy and Sarcomere Development in Human Cardiomyocytes Derived from Induced Pluripotent Stem Cells.* ACS Appl Mater Interfaces, 2016. **8**(34): p. 21923-32.
188. Seo, H.R., et al., *Nanopillar Surface Topology Promotes Cardiomyocyte Differentiation through Cofilin-Mediated Cytoskeleton Rearrangement.* ACS Applied Materials and Interfaces, 2017. **9**(20): p. 16803-16812.
189. Abadi, P.P.S.S., et al., *Engineering of Mature Human Induced Pluripotent Stem Cell-Derived Cardiomyocytes Using Substrates with Multiscale Topography.* Advanced Functional Materials, 2018. **28**(19): p. 1-11.
190. Chen, H., et al., *The effect of surface microtopography of poly(dimethylsiloxane) on protein adsorption, platelet and cell adhesion.* Colloids and Surfaces B: Biointerfaces, 2009. **71**(2): p. 275-281.
191. Delcommenne, M. and C.H. Streuli, *Control of integrin expression by extracellular matrix.* J Biol Chem, 1995. **270**(45): p. 26794-801.
192. Vite, A. and G.L. Radice, *N-cadherin/catenin complex as a master regulator of intercalated disc function.* Cell Commun Adhes, 2014. **21**(3): p. 169-79.
193. Nitsan, I., et al., *Mechanical communication in cardiac cell synchronized beating.* Nature Physics, 2016. **12**(5): p. 472-+.
194. Matsa, E., P.W. Burridge, and J.C. Wu, *Human stem cells for modeling heart disease and for drug discovery.* Sci Transl Med, 2014. **6**(239): p. 239ps6.
195. Chiong, M., et al., *Cardiomyocyte death: mechanisms and translational implications.* Cell Death Dis, 2011. **2**(12): p. e244.
196. Sayed, N., C. Liu, and J.C. Wu, *Translation of Human-Induced Pluripotent Stem Cells: From Clinical Trial in a Dish to Precision Medicine.* J Am Coll Cardiol, 2016. **67**(18): p. 2161-2176.
197. Ahmed, R.E., et al., *A Brief Review of Current Maturation Methods for Human Induced Pluripotent Stem Cells-Derived Cardiomyocytes.* Front Cell Dev Biol, 2020. **8**: p. 178.
198. Hughes, C.S., L.M. Postovit, and G.A. Lajoie, *Matrigel: A complex protein mixture required for optimal growth of cell culture.* PROTEOMICS, 2010. **10**(9): p. 1886-1890.
199. Lam, M.T. and M.T. Longaker, *Comparison of several attachment methods for human iPS, embryonic and adipose-derived stem cells for tissue engineering.* J Tissue Eng Regen Med, 2012. **6 Suppl 3**(0 3): p. s80-6.
200. Kohen, N.T., L.E. Little, and K.E. Healy, *Characterization of Matrigel interfaces during defined human embryonic stem cell culture.* Biointerphases, 2009. **4**(4): p. 69-79.
201. Martinez-Rivas, A., et al., *Methods of Micropatterning and Manipulation of Cells for Biomedical Applications.* Micromachines (Basel), 2017. **8**(12): p. 347.
202. Jansen, K.A., et al., *A guide to mechanobiology: Where biology and physics meet.* Biochim Biophys Acta, 2015. **1853**(11 Pt B): p. 3043-52.

203. Vignaud, T., H. Ennomani, and M. Thery, *Polyacrylamide Hydrogel Micropatterning*, in *Methods in Cell Biology*, M. Piel and M. Théry, Editors. 2014, Academic Press. p. 93-116.
204. Caliari, S.R. and J.A. Burdick, *A practical guide to hydrogels for cell culture.* Nat Methods, 2016. **13**(5): p. 405-14.
205. Acevedo-Acevedo, S. and W.C. Crone, *Substrate stiffness effect and chromosome missegregation in hIPS cells.* J Negat Results Biomed, 2015. **14**(1): p. 22.
206. Hilenski, L.L., et al., *The role of beta 1 integrin in spreading and myofibrillogenesis in neonatal rat cardiomyocytes in vitro.* Cell Motil Cytoskeleton, 1992. **21**(2): p. 87-100.
207. Thery, M., et al., *Anisotropy of cell adhesive microenvironment governs cell internal organization and orientation of polarity.* Proc Natl Acad Sci U S A, 2006. **103**(52): p. 19771-6.
208. Rape, A.D., W.-H. Guo, and Y.-L. Wang, *The regulation of traction force in relation to cell shape and focal adhesions.* Biomaterials, 2011. **32**(8): p. 2043-2051.
209. Lekka, M., et al., *Traction force microscopy - Measuring the forces exerted by cells.* Micron, 2021. **150**: p. 103138.
210. Blair, C.A. and B.L. Pruitt, *Mechanobiology Assays with Applications in Cardiomyocyte Biology and Cardiotoxicity.* Adv Healthc Mater, 2020. **9**(8): p. e1901656.
211. Azioune, A., et al., *Simple and rapid process for single cell micro-patterning.* Lab Chip, 2009. **9**(11): p. 1640-2.
212. Degot, S., et al., *Improved visualization and quantitative analysis of drug effects using micropatterned cells.* J Vis Exp, 2010(46).
213. Pushkarsky, I., et al., *Elastomeric sensor surfaces for high-throughput single-cell force cytometry.* Nature biomedical engineering, 2018. **2**(2): p. 124.
214. Pardon, G., et al., *Insights into single hiPSC-derived cardiomyocyte phenotypes and maturation using ConTraX, an efficient pipeline for tracking contractile dynamics*. 2021, Cold Spring Harbor Laboratory.
215. Fink, J., et al., *Comparative study and improvement of current cell micro-patterning techniques.* Lab Chip, 2007. **7**(6): p. 672-80.
216. Azioune, A., et al., *Robust method for high-throughput surface patterning of deformable substrates.* Langmuir, 2011. **27**(12): p. 7349-52.
217. Strale, P.-O., et al., *Multiprotein Printing by Light-Induced Molecular Adsorption.* Advanced Materials, 2016. **28**(10): p. 2024-2029.
218. Sharma, A., et al., *Derivation of highly purified cardiomyocytes from human induced pluripotent stem cells using small molecule-modulated differentiation and subsequent glucose starvation.* Journal of Visualized Experiments, 2015. **2015**(97): p. 52628-52628.
219. Buikema, J.W., et al., *Wnt Activation and Reduced Cell-Cell Contact Synergistically Induce Massive Expansion of Functional Human iPSC-Derived Cardiomyocytes.* Cell Stem Cell, 2020. **27**(1): p. 50-63.e5.
220. Schindelin, J., et al., *Fiji: an open-source platform for biological-image analysis.* Nat Methods, 2012. **9**(7): p. 676-82.

221. Brocher, J. *The BioVoxxel Image Processing and Analysis Toolbox*. in *European BioImage Analysis Symposium*. 2015.
222. Goncharova, E.J., Z. Kam, and B. Geiger, *The involvement of adherens junction components in myofibrillogenesis in cultured cardiac myocytes.* Development, 1992. **114**(1): p. 173-183.
223. Simpson, D.G., et al., *Contractile activity and cell-cell contact regulate myofibrillar organization in cultured cardiac myocytes.* Journal of Cell Biology, 1993. **123**(2): p. 323-336.
224. Wu, J.C., et al., *Role of N-cadherin- and integrin-based costameres in the development of rat cardiomyocytes.* J Cell Biochem, 2002. **84**(4): p. 717-24.
225. Kostetskii, I., et al., *Induced deletion of the N-cadherin gene in the heart leads to dissolution of the intercalated disc structure.* Circ Res, 2005. **96**(3): p. 346-54.
226. Nag, K., et al., *Cadherin-Fc Chimeric Protein-Based Biomaterials: Advancing Stem Cell Technology and Regenerative Medicine Towards Application*, C. Atwood and S.V. Meethal, Editors. 2014. p. 137-164.
227. Wendel, J.S., et al., *Functional Effects of a Tissue-Engineered Cardiac Patch From Human Induced Pluripotent Stem Cell-Derived Cardiomyocytes in a Rat Infarct Model.* Stem Cells Transl Med, 2015. **4**(11): p. 1324-32.
228. Masuda, S. and T. Shimizu, *Three-dimensional cardiac tissue fabrication based on cell sheet technology.* Adv Drug Deliv Rev, 2016. **96**: p. 103-9.
229. Collins, C., et al., *Changes in E-cadherin rigidity sensing regulate cell adhesion.* Proceedings of the National Academy of Sciences of the United States of America, 2017. **114**(29): p. E5835-E5844.
230. Denisin, A.K., *Controlling the Microenvironment to Investigate Single Cell Mechanobiology, Adhesion, and Function*. 2018, Stanford University.
231. Chen, V.C., et al., *Development of a scalable suspension culture for cardiac differentiation from human pluripotent stem cells.* Stem Cell Res, 2015. **15**(2): p. 365-75.
232. Sager, P.T., et al., *Rechanneling the cardiac proarrhythmia safety paradigm: a meeting report from the Cardiac Safety Research Consortium.* Am Heart J, 2014. **167**(3): p. 292-300.
233. Crumb, W.J., Jr., et al., *An evaluation of 30 clinical drugs against the comprehensive in vitro proarrhythmia assay (CiPA) proposed ion channel panel.* J Pharmacol Toxicol Methods, 2016. **81**: p. 251-62.
234. Fermini, B., et al., *A New Perspective in the Field of Cardiac Safety Testing through the Comprehensive In Vitro Proarrhythmia Assay Paradigm.* J Biomol Screen, 2016. **21**(1): p. 1-11.
235. Tseng, Q., et al., *Spatial organization of the extracellular matrix regulates cell-cell junction positioning.* Proceedings of the National Academy of Sciences, 2012. **109**(5): p. 1506-1511.
236. Rothenberg, K.E., et al., *Controlling Cell Geometry Affects the Spatial Distribution of Load Across Vinculin.* Cellular and Molecular Bioengineering, 2015. **8**(3): p. 364-382.

237. Loh, C.Y., et al., *The E-Cadherin and N-Cadherin Switch in Epithelial-to-Mesenchymal Transition: Signaling, Therapeutic Implications, and Challenges.* Cells, 2019. **8**(10): p. 1118-1118.
238. Zhao, B., et al., *Sarc-Graph: Automated segmentation, tracking, and analysis of sarcomeres in hiPSC-derived cardiomyocytes.* PLoS Comput Biol, 2021. **17**(10): p. e1009443.
239. Pardon, G., *ContraX*. 2021: GitHub repository.
240. Ribeiro, A.J.S., et al., *Multi-imaging method to assay the contractile mechanical output of micropatterned human iPSC-derived cardiac myocytes.* Circulation Research, 2017. **120**(10): p. 1572-1583.
241. Butler, J.P., et al., *Traction fields, moments, and strain energy that cells exert on their surroundings.* Am J Physiol Cell Physiol, 2002. **282**(3): p. C595-605.
242. Pasqualini, F.S., et al., *Traction force microscopy of engineered cardiac tissues.* PLoS One, 2018. **13**(3): p. e0194706.
243. Wheelwright, M., et al., *Investigation of human iPSC-derived cardiac myocyte functional maturation by single cell traction force microscopy.* PLoS One, 2018. **13**(4): p. e0194909.
244. Davis, J., et al., *A Tension-Based Model Distinguishes Hypertrophic versus Dilated Cardiomyopathy.* Cell, 2016. **165**(5): p. 1147-1159.
245. Lowndes, M., et al., *Different roles of cadherins in the assembly and structural integrity of the desmosome complex.* Journal of Cell Science, 2014. **127**(10): p. 2339-2350.
246. Gavard, J., et al., *Lamellipodium extension and cadherin adhesion: two cell responses to cadherin activation relying on distinct signalling pathways.* J Cell Sci, 2004. **117**(Pt 2): p. 257-70.
247. Goding, J.W., *Use of Staphylococcal Protein-a as an Immunological Reagent.* Journal of Immunological Methods, 1978. **20**(Apr): p. 241-253.
248. Drees, F., A. Reilein, and W.J. Nelson, *Cell-Adhesion Assays*, in *Cell Migration. Methods in Molecular Biology*, J.L. Guan, Editor. 2005, Humana Press.
249. Edelstein, A.D., et al., *Advanced methods of microscope control using muManager software.* J Biol Methods, 2014. **1**(2).
250. Van Vliet, K.J., *Instrumentation and Experimentation*, in *Handbook of Nanoindentation with Biological Applications*, M.L. Oyen, Editor. 2019, Jenny Stanford Publishing. p. 39−76.
251. Lin, D.C. and F. Horkay, *Nanomechanics of polymer gels and biological tissues: A critical review of analytical approaches in the Hertzian regime and beyond.* Soft Matter, 2008. **4**(4): p. 669-682.
252. Kandow, C.E., et al., *Polyacrylamide Hydrogels for Cell Mechanics: Steps Toward Optimization and Alternative Uses.* Methods in Cell Biology, 2007. **83**(07): p. 29-46.
253. Schwarz, U.S. and J.R. Soine, *Traction force microscopy on soft elastic substrates: A guide to recent computational advances.* Biochim Biophys Acta, 2015. **1853**(11 Pt B): p. 3095-104.
254. Kraning-Rush, C.M., et al., *Quantifying Traction Stresses in Adherent Cells*. 2012, Academic Press Inc. p. 139-178.

255. Ribeiro, A.J., et al., *For whom the cells pull: Hydrogel and micropost devices for measuring traction forces.* Methods, 2016. **94**: p. 51-64.
256. Hansen, P.C. and D.P. O'Leary, *The Use of the L-Curve in the Regularization of Discrete Ill-Posed Problems.* SIAM Journal on Scientific Computing, 1993. **14**(6): p. 1487-1503.
257. Kulkarni, A.H., et al., *Traction cytometry: regularization in the Fourier approach and comparisons with finite element method.* Soft Matter, 2018. **14**(23): p. 4687-4695.
258. Jane-Lise, S., et al., *The extracellular matrix and the cytoskeleton in heart hypertrophy and failure.* Heart Fail Rev, 2000. **5**(3): p. 239-50.
259. Kumar, A. and G.M. Whitesides, *Features of Gold Having Micrometer to Centimeter Dimensions Can Be Formed through a Combination of Stamping with an Elastomeric Stamp and an Alkanethiol Ink Followed by Chemical Etching.* Applied Physics Letters, 1993. **63**(14): p. 2002-2004.
260. Berg, S., et al., *ilastik: interactive machine learning for (bio)image analysis.* Nature Methods, 2019. **16**(12): p. 1226-1232.
261. Roca-Cusachs, P., V. Conte, and X. Trepat, *Quantifying forces in cell biology.* Nature Cell Biology, 2017. **19**(7): p. 742-751.
262. Jorge Barrasa-Fano, A.S., Álvaro Jorge-Peñas, Mojtaba Barzegari, José Antonio Sanz-Herrera, Hans Van Oosterwyck, *TFMLAB: A MATLAB toolbox for 4D traction force microscopy.* SoftwareX, 2021.
263. Legant, W.R., et al., *Multidimensional traction force microscopy reveals out-of-plane rotational moments about focal adhesions.* Proceedings of the National Academy of Sciences, 2013. **110**(3): p. 881-886.
264. Toyjanova, J., et al., *High resolution, large deformation 3D traction force microscopy.* PLoS One, 2014. **9**(4): p. e90976.
265. Chen, J., et al., *The Allen Cell and Structure Segmenter: a new open source toolkit for segmenting 3D intracellular structures in fluorescence microscopy images*. 2018, Cold Spring Harbor Laboratory.